博士論文

Role of Si addition in determining fine-scale defect formation condition and mechanism in reactor structural material

（炉内構造材の照射損傷機構に対するケイ素添加の影響）

陳　東鉞
（CHEN Dongyue）

Role of Si addition in determining fine-scale defect formation condition and mechanism in reactor structural material

（炉内構造材の照射損傷機構に対するケイ素添加の影響）

陳　東鉞
（**CHEN Dongyue**）

指導教員：関村直人　教授
（**Supervisor: Prof. SEKIMURA Naoto**）

Department of Nuclear Engineering & Management,
School of Engineering,
The University of Tokyo

Abstract

Stainless steel is used in the core of light water reactors as structural material. Due to the high neutron fluence, high temperature, stress load and corrosive water chemistry in reactors, the stainless steel components may crack during their service time in reactors. Therefore, the ageing management of stainless steel components in light water reactors is an important issue to ensure reactor safety. Currently, to evaluate the condition of stainless steel components in service, the Japan and U.S. ageing management standards mainly rely on mechanical databases of irradiation assisted stress corrosion cracking. Threshold curves of temperature and cumulative dose are drawn based on the cracking databases, and the stainless steel components that are working in conditions exceeding these thresholds are supposed to be susceptible to cracking.

However, different stainless steel components have different working conditions, which the cracking databases cannot fully cover. Also, since the setting up of cracking databases are limited to the current understanding of cracking mechanisms, the uncertainties brought up by possible unknown factors or mechanisms could be large. Therefore, besides the cracking databases, continuous efforts should also be made to trace back to the microstructure evolution process in irradiated stainless steel, which is the origin of the mechanical degradation.

The main objective of this research is to investigate the formation mechanisms of black dots, dislocation loops and γ’ precipitates under irradiation. The interactions between these defects are completed during microstructure evolution process. Therefore, irradiation condition is controlled so that the formation of black dots and Frank loops could be isolated, and their formation mechanisms could be discussed respectively by tuning the Si content of stainless steel. By raising irradiation temperature and dose, γ’ precipitates are introduced. The formation mechanisms of γ’ precipitates are analyzed by combining near-atomic scale three dimensional atom maps with first principle calculation. The possible relationship between the formation of precipitates and dislocation loops are discussed. Additionally, attempts are made to quantitatively correlate these microscopic defects with macroscopic hardening in heavy ion irradiation by utilizing the heterogeneous defect depth distribution observed.

High purity solution-annealed 316L stainless steel model alloys are prepared, and are irradiated by heavy ions at 290~450°C in this study. The major post irradiation analysis include nano-indentation, transmission microscopy and atom probe tomography. The principal results obtained are:

1) The formation of black dot is not much influenced by Si in irradiation at 290ºC. However, Frank loops are distinctively suppressed by Si addition at 400ºC in both density and size, especially in the near-surface region. This could be explained by Si's role in enhancing the effective diffusivity of vacancies and thus promoting recombination. It could also be explained if the Si addition can promote the trapping of interstitials by surface sink. For low Si samples, the unfaulting of Frank loops is not evident until the irradiation temperature is raised to 450ºC.

2) When irradiated at 290ºC to ~0.8dpa, the addition of Si enhances Ni segregation. And Ni tends to enrich near positions of Si enrichment in high Si sample, which may be the precursor of Ni-Si precipitates.

3) Ni-Si precipitates are formed in both base Si (0.42wt.%) and high Si (0.95wt.%) samples irradiated at 450ºC to 5dpa. In well-developed Ni-Si precipitates, Ni/Si atom ratio is found to be smaller than 3 while maintaining Ni+Si≈96at.% by atom probe tomography. It could be explained by VASP calculation that when one Ni atom is replaced by Si, the configuration is still preferable as its defect formation energy is very close to zero. Mo and Mn are fully depleted at an early stage of precipitate formation.

4) Some Ni-Si precipitates are found to be of ring shape. And base on the shape, size and orientation, they should have formed on dislocation loops. Si addition retards loop unfaulting, possibly via suppressing Frank loop size or stabilizing Frank loops by precipitation.

5) The irradiation hardening tested by nano-indentation matches the microstructure observed in this work. The Orowan model can also be applied in heavy ion irradiation by averaging the inhomogeneous loop density and size in a

semi-spherical plastic zone. A hardening coefficient of around 0.30 is obtained for all the three samples irradiated at 400°C to 3dpa by assuming the maximum depth of the plastic zone to be five times of the indentation depth. This hardening coefficient value meets the lower limit of previous literature data.

The present study is a fundamental research on stainless steel degradation under irradiation. It contributes to ageing management and nuclear safety by improving the knowledge base of degradation behavior. This work found the complexity in the stoichiometry of Ni-Si precipitates, and confirmed the interactions between dislocation loops and precipitates, which both emphasize the importance of further studies on Ni-Si precipitates. It provides references for future design of stainless steels by further clarifying the effects of Si in irradiation. It improves the reliability of using heavy ion irradiation tool to emulate neutron damage.

Further work on Ni-Si precipitates is suggested based on the results obtained in this work. The nature of Ni-Si precipitates and their role during stainless steel deformation needs to be reconsidered. Their interactions with dislocation loops need to be further analyzed by modeling.

Index

1. Introduction

1.1 Ageing management of reactors

Currently, the nuclear energy is playing an important role in electricity generation in the world. Fig. 1-1 shows the nuclear share of electricity generation in 2014 summarized by IAEA, and the majority of these reactors are light water reactors (LWRs) [1]. In countries like France and Slovakia, nuclear energy contributes over 50% of nation’s total electricity generation, while in some other developing countries such as China, India and Turkey, great efforts are being made to increase the share of nuclear energy in the nation.

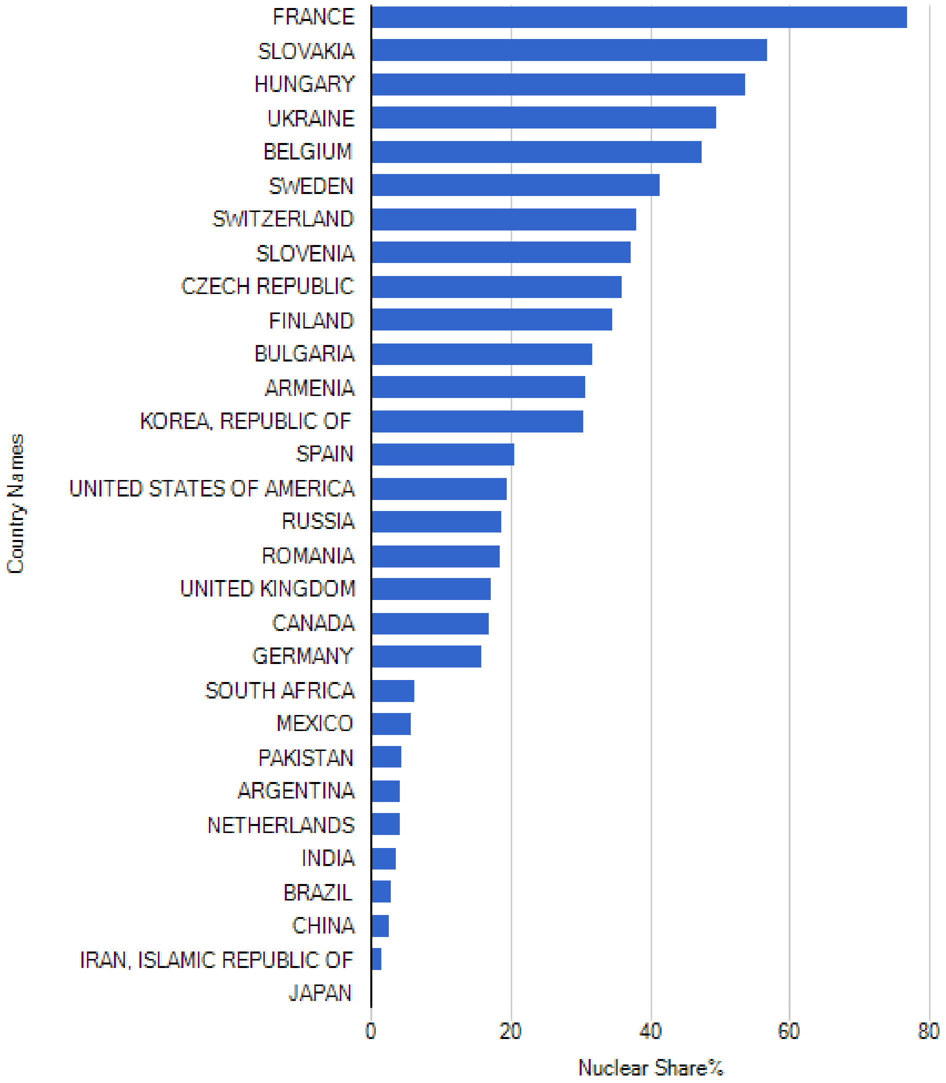

Fig. 1-1 Nuclear share of electricity generation in 2014 (IAEA) [1]

Presently in China, the central government has issued the “Twelfth Five Year Plan” and Mid-long Term Development Planning for Nuclear Power to encourage nuclear industry [2]. In the year of 2014, 27 reactors are under operation in China, and 23 more reactors are being constructed [1].

However, the Fukushima Dai-ichi accident on March 16th, 2011 in Japan has warned again the importance of ensuring reactor safety. For China, the challenge of reactor ageing management lies in two aspects.

- Firstly, the old Qinshan-1 and Daya Bay LWR has been operated for over 20 years and is going to reach their design lifetime in the near future. The ageing condition of these old reactors needs to be assessed for the possibility of life extension. This will be the very first time for China to conduct a reactor license renewal.
- Secondly, many newly-constructed reactors of Generation II and III, have just started operation or will start operation in a few years. They cover a wide range of reactor types, such as such as PWR, EPR, CPR1000, AP1000, WWER, CANDU and HTGR. Considering of the so many types of reactors being constructed, operation experience and database are still lacking for China; therefore special care should be taken for the ageing management of these reactors.

IAEA safety standards have pointed out that the ageing process of reactors consists of two parts: the physical ageing of structures, systems and components (SSCs), and the obsolescence of SSCs, which means their becoming out of date compared with current knowledge or standards [3]. Among them, a comprehensive understanding of SSC physical ageing process is an essential starting point, and is the key to effective ageing management of reactors.

The different types of SSCs that are important to reactor safety can include core structural components, reactor pressure vessel, piping, concrete structure, cables, and etc. Some cases of component failure or material crack have already been observed in current running LWRs [4]. This could be very dangerous for LWRs. In this work, the ageing of core structural components, which is usually made of 304 or 316 series stainless steel, is focused on.

1.2 Ageing management of stainless steel components

1.2.1 Working conditions of stainless steel components in reactors

Stainless steel is the major structural material used in LWRs. It's used as plates, barrels, baffles, formers, bolts and so on in the LWR core internals. The major functions of these stainless steel components are two:

- Support the core structure.
- Guide the coolant flow.

Table 1-1 Working environment for typical stainless steel components in PWR [5]. The dose received is estimated by 32 effective full power years of operation.

	Temperature (°C)	Dose (dpa)	Estimated order of average dose rate (dpa/s)	Component function
Upper core plate	~325	0.3~0.45	$\sim 10^{-10}$	Ensure fuel assembly, control rod position.
Lower core plate	~290	0.17~5.6	$\sim 10^{-10} \sim 10^{-9}$	Support the core; Control coolant flow.
Core barrel	260~330	1~10	$\sim 10^{-9}$	Support the core.
Core baffle & former	290~370	10~110	$\sim 10^{-8}$	Separate coolant flows.
Bolt	290~370	58~110	$\sim 10^{-8}$	Connect and fix.

The degradation of stainless steel components mainly comes from the synergetic effects of high temperature, high neutron fluence, stress load and corrosive water chemistry in LWR. Depending on the positions they are installed at, the temperature and dpa they received during service time could vary a lot. Table 1-1 summarizes the working environment of some typical stainless steel components in pressurized water reactor (PWR) [5], and together with their major functions. PWR is selected here because the accumulative neutron dose in PWR could be much higher than that in boiled water reactor (BWR). In the table, the total dose received during service time is estimated by 32 effective full power years of operation, which corresponds to ~40 years of reactor life time.

Table 1-1 shows that in PWR, the temperature of stainless steel components is mostly in the range of 290~370°C, but the total dose during service time could vary from less than 1 dpa to as high as 100 dpa. Such large displacement damage could cause evident property change in stainless steel components, which could be dangerous to the component reliability. The dose rate is at the order of 10^{-10}~10^{-8} dpa/s.

Therefore, it is easy to imagine the consequences if one or several stainless steel components lost their functions, there will be structural integrity failure. Fuel assembly may be disordered, and the insertion of control rods may become impossible. The coolant flow may no longer be efficiently covering the whole core area, leading to insufficient cooling in some local areas. These possible consequences are obviously not acceptable when considering rector safety. That’s why the integrity and function of stainless steel components have to be ensured during their service time in LWR as the basis of safety management.

1.2.2 Current standards to evaluate stainless steel component ageing

The integrity and function of stainless steel components is important, and their failure is unacceptable speaking of reactor safety, so that’s why ageing management standards of stainless steel components have been published in many countries to ensure their function during service time. Here the Japan and United States standards are mentioned as examples.

- Japan

In Japan, IASCC is regarded as the major threat to the stainless steel components in PWRs. As described in the standard JANSI-VIP-05 created by Japan Nuclear Safety Institute (JANSI), the cracking of stainless steel components in PWRs is predicted based on the neutron dose and stress loads it receives during service.

Japan Nuclear Energy Safety Organization (JNES) has previously built up a database to define the threshold conditions of IASCC in stainless steel components, as shown in Fig. 1-2 [6]. To build up the database, neutron irradiated stainless steels are tested by stress corrosion crack tests under selected external stresses. Then the threshold condition curves are drawn based on these experimental test data for baffle former bolts and thimble tubes. In conditions above the threshold curve, IASCC is supposed to occur for the stainless steel component. Note that for baffle former bolts, the threshold curve (red curve) above 20dpa is here drawn by extrapolation without experimental data.

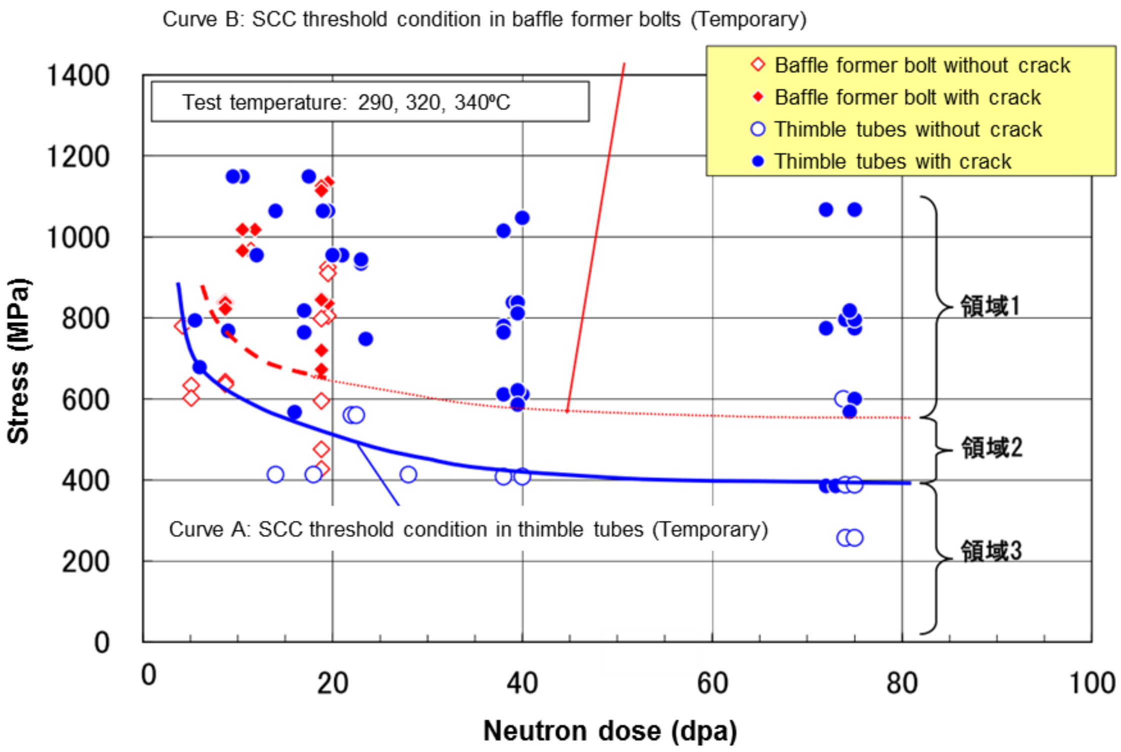

Fig. 1-2 The threshold conditions of IASCC in stainless steel components [6]

- United States

In the standards of United States, similar databases of mechanical properties are built up by Electric Power Research Institute (EPRI) [7]. When flaws exceeding the allowable crack initiation criteria are detected in PWRs, integrity assessment needs to be performed. For components with neutron fluence less than 3x10^{20}n/cm^2 (E>1MeV), or ~0.5 dpa, based on databases a threshold load value should not be exceeded for the component to continue its service in PWRs. For neutron fluence above ~0.5dpa, the crack growth must to be evaluated through existing databases to ensure the structural integrity of the component.

1.2.3 Improving the knowledge base of stainless steel component ageing

As discussed above, the current standards to evaluate stainless steel component ageing in LWRs largely rely on the experimental databases of mechanical property degradation. Using databases of mechanical properties is straightforward and practical in engineering application, but it also has its limitations:

- Various working conditions can hardly be fully covered in databases.

The ageing process of stainless steel is complicated. Several degradation modes could occur during service time, and these degradation modes are actually related more or less with each other.

For simplicity, here only take IASCC as an example. IASCC could be directly influenced by temperature, neutron dose, dose rate, applied stress, material composition and water chemistry. As previously shown in Table 1-1, the temperature and dose can vary from place to place in LWRs. So is external stress and dose rate. Therefore with the combinations of these parameters, it will be very difficult to build up huge databases of mechanical properties covering all components at all positions in all types of reactors.

Besides, currently a large fraction of the high neutron dose data has been obtained by irradiation in fast reactors [8]. The dose rate in fast reactors is orders of magnitude higher than that in commercial LWRs. And the thermal- and fast- neutron energy spectrum is also different between them. In the United States, most of the void swelling data have been obtained at irradiation temperature above 385°C in fast reactors [8], which is much higher than LWR temperature. Thus the databases used as references in standards actually could have quite different condition from the commercial LWRs.

As a conclusion, based on limited research resources and capability, it is almost impossible to build a complete database of mechanical properties to exactly match all kinds of component working environments in LWRs. The effects of different ageing factors (such as temperature, dose, etc.) need to be understood, so that the mismatch between actual component working conditions and the database values could be evaluated. To achieve this, it is necessary to trace back to the origin of mechanical degradation phenomena, or to be more precise, the microstructure evolution process under irradiation.

- Unknown degradation mechanisms may exit.

The standards and databases set up currently are based on the current understandings of the ageing possesses. Since the ageing process of stainless steel components is actually very complicated, it is still not fully understood despite of the extensive efforts done in the past decades. Therefore, it could be possible that there are still some unknown ageing mechanisms of stainless steel components that could occur under some specific conditions; or perhaps some unknown factors that previously do not attract people's attention could turn to be determinative in some situations.

For example, previously the formation of γ' phase Ni-Si precipitates in irradiated stainless steels were unknown to us, until their existence was discovered by Cawthorne et al. [9] and Brager et al. [10] in 1977~1978. And then, for a long time, the γ' precipitates were believed to form only in low density, until the recent development in atom probe tomography (APT) revealed the number density of Ni-Si precipitates to be almost one order higher than that previously observed by transmission electron microscopy (TEM) [11]. The existence of the very dense Ni-Si precipitates in irradiated stainless steels has been unknown to us for many years. They should have some impacts on the ageing processes such as hardening and crack growth, but they were not considered in the old standards of ageing management. If efforts had not been made to trace back to the origin of mechanical property degradation, Ni-Si precipitates might not be discovered.

Similarly, due to the limitation of current knowledge base on ageing, there may be other unknown phenomena or mechanisms that are not included in the current standards. Continuous efforts should be made to improve the current knowledge base of ageing. In this way, the unknown factors could be reduced, and the uncertainties in standards that are introduced by the existence of unknown factors could be minimized.

Thus as a conclusion, although it is effective and practical to carry out standards based on databases of macroscopic mechanical properties, continuous efforts should also be made to trace back to the microstructure evolution process, which is the origin of the mechanical degradation. The knowledge base of ageing mechanisms should be kept updating, to bridge the mismatch between actual component working conditions and database values, and to reduce the uncertainties in standards introduced by possible unknown factors.

1.3 Current understanding of microscopic ageing mechanisms

When speaking of the microscopic ageing mechanisms of stainless steel components under irradiation, we are usually referring to the formation mechanisms of various radiation defects.

Various types of radiation defects form in stainless steel materials during irradiation. The radiation defects contribute more or less to various kinds of degradation modes of stainless steel components. And finally, the degradation modes cause the reported safety issues in reactors. This relationship is generally illustrated in Fig. 1-3. It will be described in detail in the following subsections, together with the previous results which improved the understanding of each process and better clarified their relationship.

1.3.1 Radiation defect formation

Microstructure evolution in irradiation is a very complicated process. Extensive studies have been done on it focusing on different stages of evolution. T. Muroga and N. Sekimura have summarized the general irradiation damage evolution based on time scale, as shown in Fig. 1-4 [12].

Here, only the most related processes and results about radiation defect formation in stainless steel are described. When one irradiation particle hits material surface, it knocks a series of atoms off their lattice positions, creating a displacement cascade containing many interstitials and vacancies, which is called the collisional phase. Most of such point defects quickly recombine in cooling phase in less than 10 picoseconds. After cooling phase, only some point defects survive, in the form of single point defects or defect clusters. These point defects and defect clusters may diffuse, recombine, agglomerate, emit point defects or be trapped by sinks in a much longer time scale. In this stage, radiation defects of larger size, such as loops, precipitates and cavities, are formed. More detailed explanation could be found in the textbook written by Gary Was [13]。

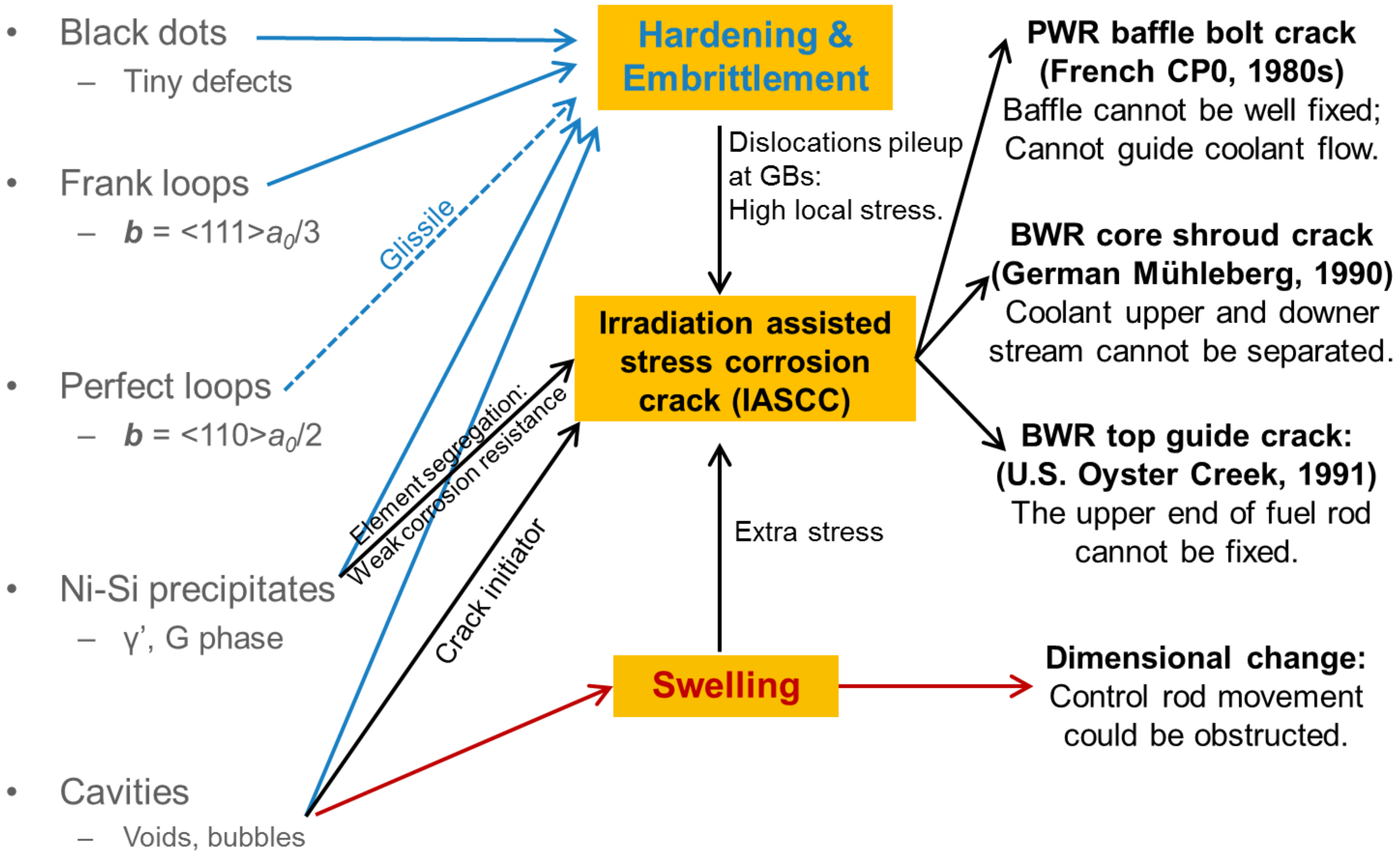

Fig. 1-3 General relationship between radiation defects, major degradation modes and reported safety issues of stainless steel components in reactor.

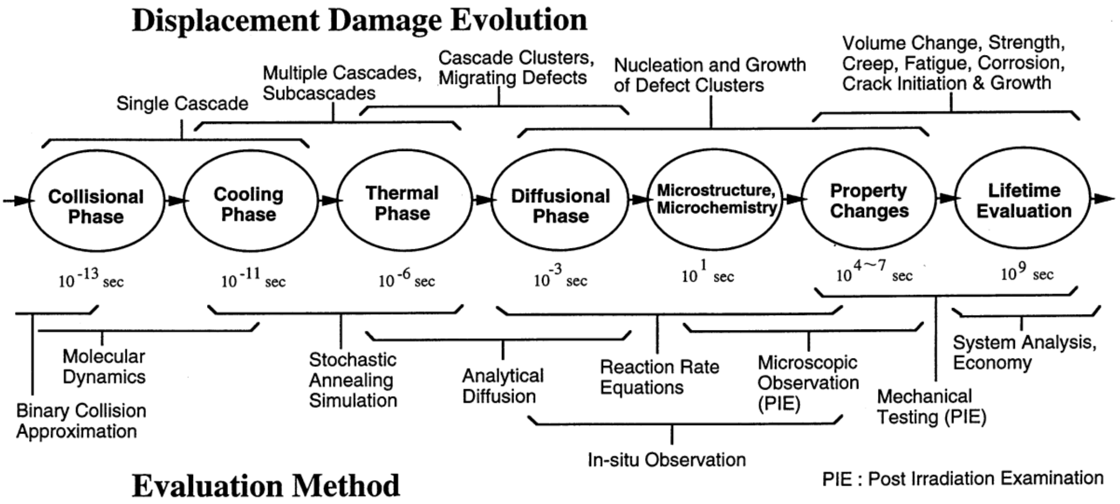

Fig. 1-4 A schematic of time evolution of irradiation damage [12]

One thing to note is that irradiation beam is actually continuous. The different time stages are defined here for easy understanding of irradiation processes. It does not mean that these stages are appearing one by one in a time sequence. In fact, the cascades are repeatedly created and collapsed, and the processes such as point defect diffusion, agglomeration and recombination are occurring during the whole period of irradiation. This makes the scenario completed to clarify.

The various types of radiation defects that may form in stainless steel materials during irradiation have been previously studied by transmission electron microscopy (TEM). The radiation defects can be classified into the following categories:

- Frank loops.

Frank loops, or named as faulted loops, are the partial dislocation loops with Burgers vector of <111>a_0/3 in face-centered cubic (FCC) lattice. Each Frank loop contains a stacking fault of {111} plane.

They are the most commonly-observed kind of dislocation loops in irradiated stainless steel. They could be stable with almost unchanged morphology even at very high doses (>70dpa). But when irradiation temperature is also high (>400°C), Frank loops could unfault by dislocation reactions and become perfect loops [14]. Frank loops could be very dense when irradiation dose is around 5dpa or higher, which brings difficulty on detailed formation mechanism study [11]. Frank loops are sessile dislocation loops which can climb but cannot glide. This makes them one of the major contributors in irradiation hardening.

- Perfect loops.

Perfect loops, or named as unfaulted loops, are the type of dislocation loops that can be both observed under irradiation or cold work. They have the Burgers vector of $<110>a_0/2$ and do not contain stacking fault. Since perfect loops are glissile, their contribution to irradiation hardening is regarded to be much smaller than Frank loops.

- Ni-Si precipitates

Carbides are also an important type of precipitates in carbon-containing stainless steels. But in high purity stainless steels such as 304L or 316L, Ni-Si precipitates are the major focus. Generally two possible types of Ni-Si precipitates could be seen under irradiation, the γ’ phase and the G phase. And γ’ phase is the one that is most commonly-observed under irradiation. γ’ phase is an irradiation-induced phase, and is theoretically Ni_3Si in composition. It does not form in thermal ageing experiments. γ’ precipitates also contribute to irradiation hardening.

The observation of γ’ phase under TEM is usually difficult, as γ’ phase has similar lattice structure, lattice constant and orientation with the austenite matrix, and is usually coherent with the matrix [15]. Recent studies start to use atom probe tomography (APT) for better characterization of γ’ phase, but data is still not enough to clarify the formation mechanism of γ’ precipitates.

Dislocation loops may provide nucleation sites for γ’ precipitate formation. Jiao et al. observed some ring-shaped precipitates, which may be formed on dislocation loops due to its special shape [16]. Etienne et al. found precipitates and dislocation loops having similar number density and size [17], but Toyama et al. found in their experiment that the number density of precipitates is one order higher than that of loops [18]. Proofs still lacks on the relationship between precipitates and dislocation loops.

- Cavities

Two types of cavities, bubbles and voids, can be generated under irradiation. The former is caused by helium generation in neutron irradiation [19], and the latter is not.

Due to the stabilization effects of helium gas, bubbles can form at lower temperatures than voids. Cavities are the major cause of swelling. Addition of minor alloying elements can have pronounced effects on cavity formation [20-23]. Low dose rate will also enhance cavity formation [24]. Both bubbles and voids contribute to irradiation hardening. They also cause irradiation swelling.

- Black dots

Black dots do not refer to a specific type of radiation defects, but are the general name for tiny defects (several nanometers in size) observed under TEM. Since the size of black dots is comparable to the resolution limit of TEM, their nature are difficult to identify. Black dots could be point defect clusters, tiny dislocation loops, stacking fault tetrahedra, or maybe tiny precipitates in nature [25]. Black dots also contribute to irradiation hardening.

1.3.2 Degradation modes

The formation of radiation defects mentioned above directly leads to stainless steel degradation. Generally speaking, the degradation modes of stainless steel components that are most important to LWR safety are the following three:

- Hardening and embrittlement

After irradiation, stainless steel components will increase in yield strength and hardness, and decrease in ductility. Fig. 1-5 illustrates the typical engineering stress-strain curve of stainless steel after proton and spallation neutron irradiation [26]. Pronounced increase in yield strength is observed after irradiation. Elongation reduces as well, which is an indicator of reduced ductility.

Stainless steel has to survive loads and stress during LWR operation. The loss in ductility will cause the stainless steel components easy to fracture.

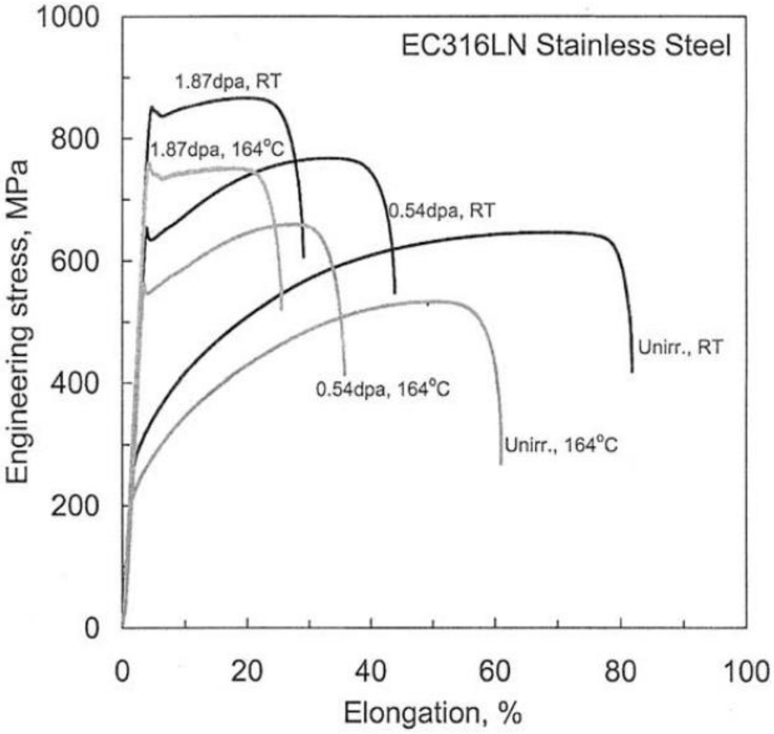

Fig. 1-5 Typical irradiation hardening of stainless steel after proton and spallation neutron irradiation [26]

- Swelling

Stainless steel components will grow in size during irradiation, and this is called the swelling process. The percentage of dimensional change could be small, but as the original sizes of some stainless steel components are large, the absolute value of dimensional increase cannot be ignored. Swelling is mainly caused by the voids and bubbles formed during irradiation.

- Irradiation assisted stress corrosion cracking (IASCC)

IASCC means that some stainless steel components become susceptible to inter-granular cracking in LWRs, and would crack even under low stresses. IASCC is the major issue faced by stainless steel in reactors [27], and is a very complicated degradation process. Its origin is still not clear enough, but it should result from the synergy effects of irradiation damage, corrosive water environment, local stress, material composition and manufacturing process [28-30]. Irradiation hardening and cavity formation will also contribute to IASCC.

In fact, the degradation process in stainless components is very complicated. The three degradation modes described above cannot be fully separated from each other. For example, irradiation hardening can contribute to IASCC because it increases local stressing, especially the high local stress caused by dislocation pileup near grain boundaries; the voids and bubbles which cause swelling may also be the crack initiators in IASCC; also swelling itself exerts extra stress between components and thus aggravates IASCC. There are other degradation modes such as fatigue that should also draw people’s attention.

The IASCC degradation has been reported in actual reactors both for PWRs and boiled water reactors (BWRs). For PWR, in 1980s, the French reactor CP0 discovered baffle bolt crack that may well be the result of IASCC [5]. The cracking of baffle bolts would cause problems in baffle fixing and coolant flow guidance. For BWR, the cracking of core shroud was found in the German Mühleberg reactor in 1990, and the cracking of top guide was reported in the U. S. Oyster Creek reactor in 1991 [31]. The failure of core shroud will also lead to problems in coolant guidance, while the top guide cracking will cause loose fixing of the fuel rod upper end.

1.3.3 The Orowan hardening model for neutron irradiation

The relationship between microscopic radiation defects mentioned above and macroscopic hardening and has been previously set up by the Orowan model in neutron irradiation [32, 33]. When a moving dislocation encounters a radiation defect, the defect may act as an obstacle to the dislocation movement. A strong obstacle will bow the dislocation line, as illustrated in Fig. 1-6. Such dispersed barrier hardening caused by bowing mechanism is quantitatively described by the Orowan model:

$$\Delta\sigma = (\sum_{k} \Delta\sigma_k{}^2)^{1/2} \tag{1-1}$$

$$\Delta\sigma_k = \alpha_k M \mu b (N_k d_k)^{1/2} \tag{1-2}$$

where $\Delta\sigma$ is the increase in yield strength, which can be converted from hardening;

k is one type of radiation defect, could be black dots, Frank loops, precipitates and cavities.

$\Delta\sigma_k$ is the contribution to yield strength change by type k defects;

N_k is number density of type k defects;

d_k is average size of type k defects;

M is the Taylor factor;

μ is the shear modulus;

b is the length of Burgers vector;

α_k is the hardening coefficient for type k defects, a factor between 0~1. Its value changes for different types of defects, and represents the strength of a specific defect as a barrier. For a perfectly hard barrier k, the α_k value would be 1.

M, μ and b are constants, also $\Delta\sigma$, N_k and d_k are experimentally measurable, therefore linear plot of $\Delta\sigma_k$ versus $(N\times d)^{1/2}$ have been previously performed in neutron irradiation to extract the value of α_k for each type of radiation defects [18, 32]. In this way, neutron hardening data can be explained by their corresponding radiation defect formation via the Orowan model.

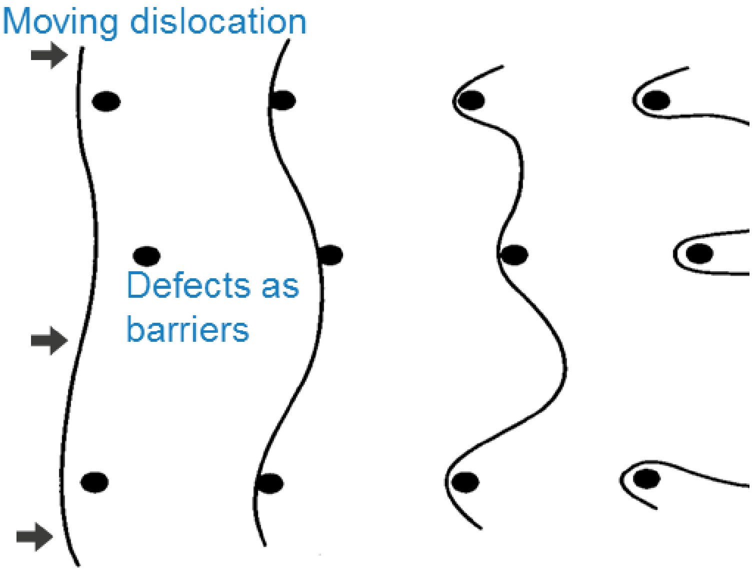

Fig. 1-6 Irradiation hardening caused by bowing mechanism

In this study, the microscopic degradation mechanisms in stainless steel components and their corresponding irradiation hardening and embrittlement are the focuses. The radiation defects formed under irradiation will be discussed, and special attention will be drawn on Ni-Si precipitates. Because despite of their high density recently observed in some irradiated stainless steels, their influences on microstructure evolution and irradiation hardening are still unclear. The effects of some important component service parameters, such as irradiation temperature, dose and Si content, on material degradation will be evaluated. The model to quantitatively correlate macroscopic irradiation hardening with microscopic radiation defects will be discussed.

1.4 Design of current research

From the previous literature results summarized above, the major difficulties faced in previous research and how attempts are made in this study to try to overcome these difficulties are discussed below.

1.4.1 Attempts to simplify defect interactions

One difficulty in studying radiation defect formation mechanism is the complex interactions between different types of defects. Roughly speaking, there are two major types of interactions:

- Firstly, the existence of one type of radiation defect can provide nucleation site for another type of defect. For example, small MC (carbides) particles were observed at the edge of loops or at network dislocations [34]. Possibly, dislocation loops have provided nucleation site for carbides.
- Secondly, some types of radiation defects are competing for interstitials or vacancies. Two examples of direct competition are: network dislocations introduced by cold work compete with radiation-induced loops for interstitials; fine helium bubbles compete with voids for vacancies [35].

The actual interactions between defects may be even more complicated than the two mentioned above. When the formation mechanism of one type of radiation defect is aimed to be studied, it will be ideal if other kinds of defects will not appear in the irradiated material. If such isolation of defect formation is possible, the defect formation process could be more straightforward to be observed and analyzed.

Such isolation of defect formation may be possible by carefully controlling the irradiation conditions. Extensive previous TEM observation data on irradiated stainless steel could be good references. With the help of such databases, it could be possible to select some combination of irradiation temperatures and doses, in which only one or two types of defects appear as the major radiation defects.

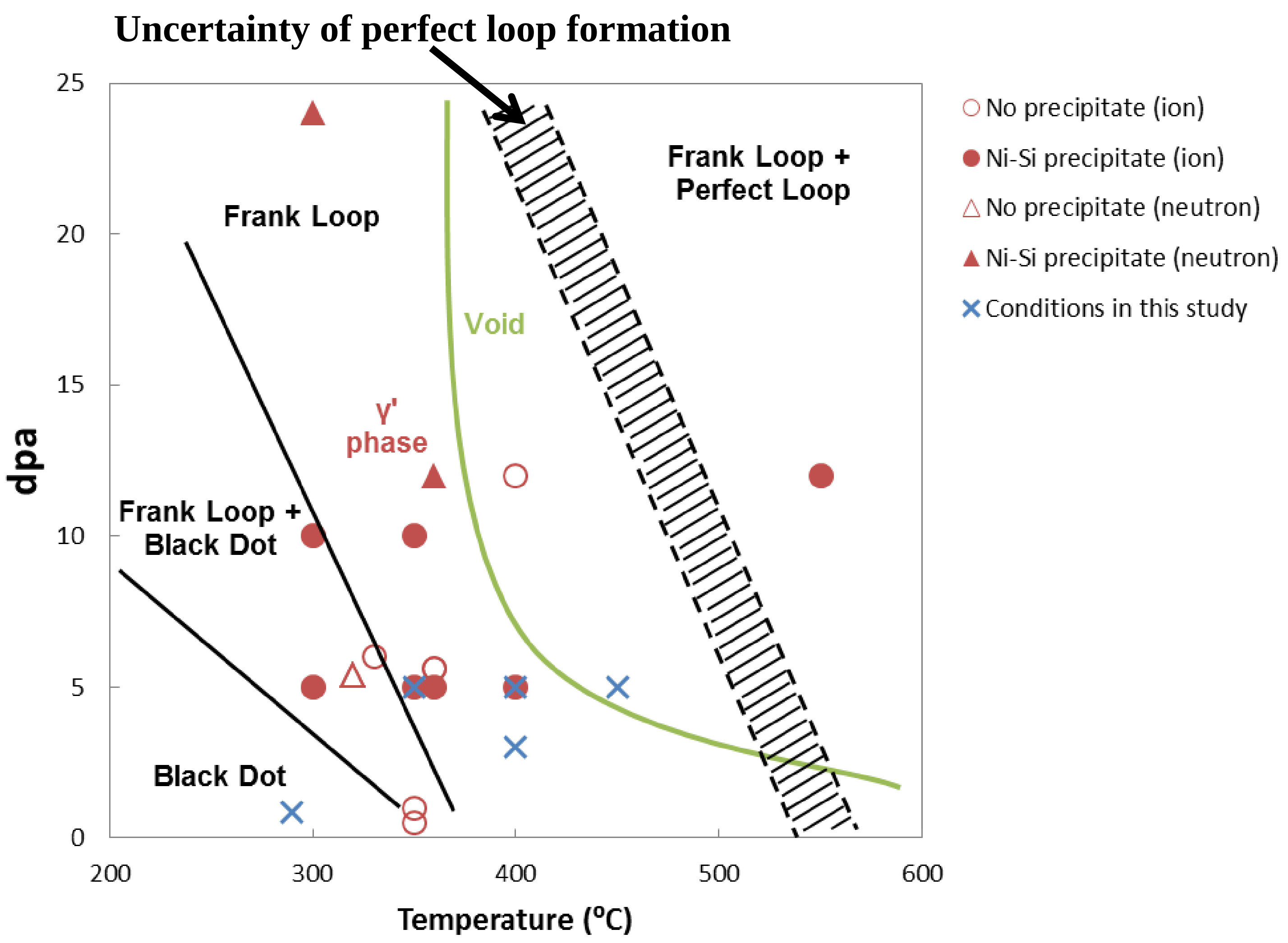

Fig. 1-7 A literature data summary of defect formation conditions in stainless steel. Black dots, loops and voids data comes from TEM observation results in neutron irradiation; Ni-Si precipitates data comes from the recent APT data in neutron (triangle) and ion irradiation (circle) with Si content of 0.4~0.8wt.%. Dash regions represent data uncertainties.

Fig. 1-7 summarizes the literature data of defect formation conditions in austenite stainless steel. The formation condition data of black dots, loops and voids comes from the reviews of TEM observation results in neutron-irradiated stainless steel [35, 36]. The formation condition of Ni-Si precipitates comes from the recent atom probe tomography (APT) data in neutron (triangle point) and ion irradiation (circle point) with Si content of 0.4~0.8wt.% [16-18, 37-42]. The dash region represents the data uncertainty of perfect loop formation. Due to the recent development of APT observation technique, Ni-Si precipitates are discovered to be formed at lower temperature and lower dose than previously expected by TEM observation. Currently, still not much APT data of Ni-Si precipitate formation is published.

The irradiation conditions selected in this study are marked as blue crosses in Fig. 1-7. The 290°C and 0.8 dpa condition is for black dot study only. At higher temperatures of 350°C and 400°C, Frank loops are the main focus in samples without Si addition. Then samples with Si addition are also irradiated at these conditions, to try to find out the boundary condition for γ’ precipitate formation. At the highest temperature of 450°C and 5dpa, γ’ precipitates are expected to form in large density. Voids or perfect loops may also be formed in this condition, and discussion about their interactions will be attempted in this most completed scenario, based on the knowledge obtained from the other simpler conditions in this study.

1.4.2 Silicon content tuning

Since the γ’ precipitates (Ni_3Si) are one focus in this study, the Si content of stainless steel must be considered. Actually, besides directly contributing to the formation of γ’ precipitates, Si is believed to affect many aspects of the microstructure evolution process. Even small amount of silicon addition (~0.5wt.%) can bring pronounced effects on radiation defect formation.

Generally speaking the effects of Si alloying element is pronounced but complicated in irradiated stainless steel. Sekimura et al. have found that in neutron irradiation, addition of only 0.14wt.% Si in stainless steel model alloy promoted irradiation swelling, but further addition of Si turned to dramatically suppress swelling, as shown in Fig. 1-8 [20].

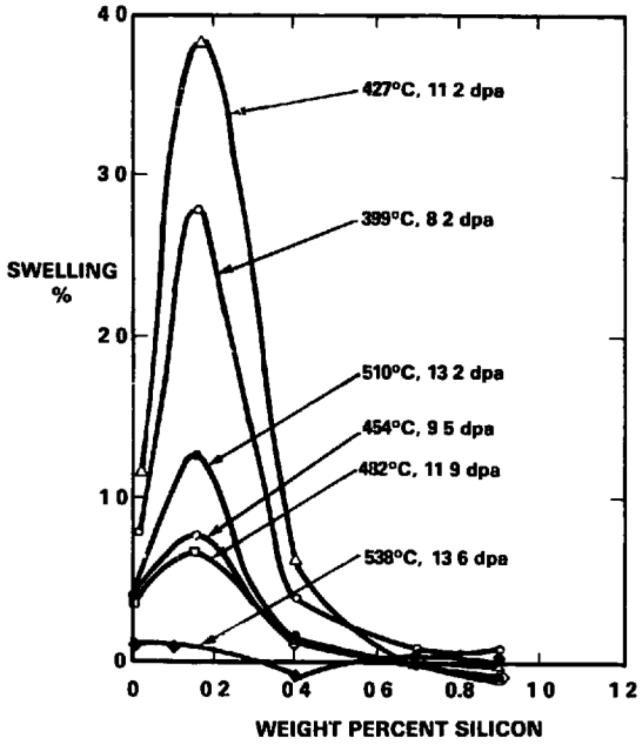

Fig. 1-8 Si effects on swelling in neutron-irradiated Fe-15Cr-25Ni-Si alloys [20]

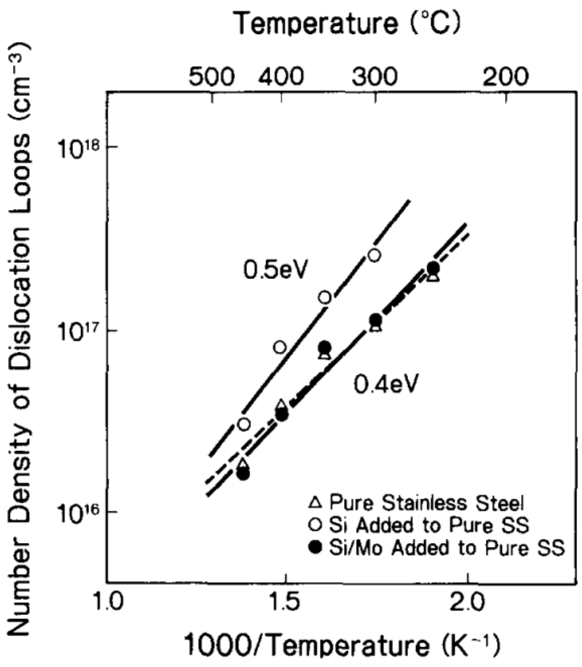

Fig. 1-9 Si effects on dislocation loop density in stainless steel model alloys irradiated at various temperatures by 300keV He^+ to 0.1dpa

The effects of Si addition on dislocation loops are also complex. Shigenaka et al. found in He^+ irradiated stainless steel model alloys that the addition of 0.30wt.% Si promoted the number density of dislocation loops at several temperatures, but further addition of 2.52wt.% Mo cancelled the loop density promotion, as shown in Fig. 1-9 [43]. Fukuya et al. also found Si addition to enhance loop nucleation [44]. However, Miwa found loop density was suppressed by Si addition in their experiments [45]. It seems that the trend observed of Si effects on dislocation loops could be different under different irradiation conditions.

Fundamentally speaking, such silicon effects on radiation defect formation should be attributed to its influences on point defect diffusion. Si is an undersized fast-diffusing element in austenite stainless steel. Currently mainly two mechanisms for Si diffusion in stainless steel are proposed: the vacancy exchange mechanism and the interstitial dragging mechanism.

- Vacancy exchange mechanism.

The vacancy diffusion mechanism assumes Si atom diffuses through swapping positions with vacancies. It could be been modeled and is used to explain the reason why swelling is suppressed by Si addition [46]. However, it alone cannot explain the Si segregation at sinks. In the theory of vacancy diffusion mechanism, Si atoms are supposed to diffuse up vacancy gradient, which means they tend to be away from vacancy sinks.

- Interstitial dragging mechanism.

The interstitial dragging mechanism assumes Si atom diffuses through solute-interstitial binding complexes. In this mechanism, Si atoms can trap interstitials by binding, so that interstitial loop formation could be refined with higher loop density [21, 47, 48]. Also Si atoms will diffuse down interstitial gradient, which explains the segregation of Si at various sinks [41]. But due to the complexity of interstitial diffusion process which includes interstitial jumping and direction changing of dumbbells, the details of such diffusion mechanism are still not clear.

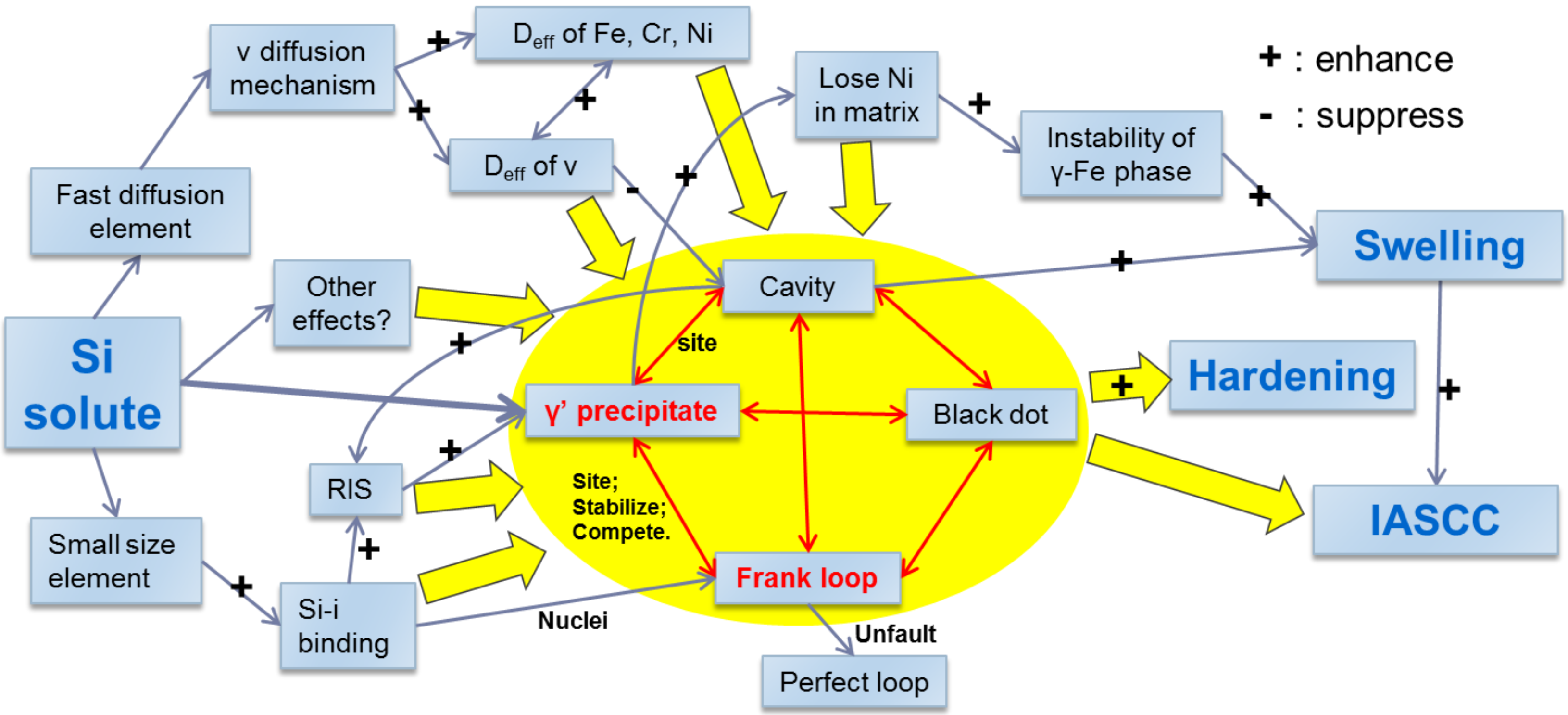

Fig. 1-10 Brief summary of Si effects on microstructure evolution of stainless steel under irradiation

Currently, none of the two theories are satisfying enough to explain the major Si effects during irradiation. They need to be improved to be more detailed, and their applicable conditions need to be clarified.

In fact, the current difficulty in clarifying Si effects on defect formation is that the role of Si in microstructure evolution is just too complicated. Si is influencing almost all the important aspects of microstructure evolution under irradiation in austenite stainless steel, as briefly summarized in Fig. 1-10. It changes the point defect diffusion rate. It may change the diffusion rate of other elements. It directly induces the formation of γ' precipitates, but it also influences the formation of other radiation defects. The four major types of radiation defects (in the yellow circle) also interact with each other, which make the scenario even more complicated.

In this study, via the proper selection of irradiation parameters, as described in Section 1.4.1, the scenario is expected to be simplified. In such a simpler situation, Si effects could be a tool instead of an obstacle when studying microstructure evolution, as Si interacts with point defect diffusion and determines Ni-Si precipitate formation. If only one or two major radiation defects are formed under one selected irradiation condition, their forming mechanism could be further analyzed by tuning the Si content of model alloys, to see what effects of the changed point defect diffusivity will have on the defect formation.

1.4.3 Utilization of advanced technologies

- Atom probe tomography (APT)

As described in Section 1.3.1, due to the similarity in lattice structure between γ phase austenite matrix and γ' phase precipitates, TEM is not suitable for the study of the initial stage of precipitation or small precipiates. Fig. 1-11 are images of some typical γ' phase precipitates observed under TEM [32]. The weak contrast brings difficulty on precipitate size and density measurement. This limits the previous works on precipitate analysis.

In this study, the APT technology which becomes mature in recent years will be applied. APT is sensitive to element species, so is suitable for precipitates analysis. APT can also provide atom maps of near atomic resolution.

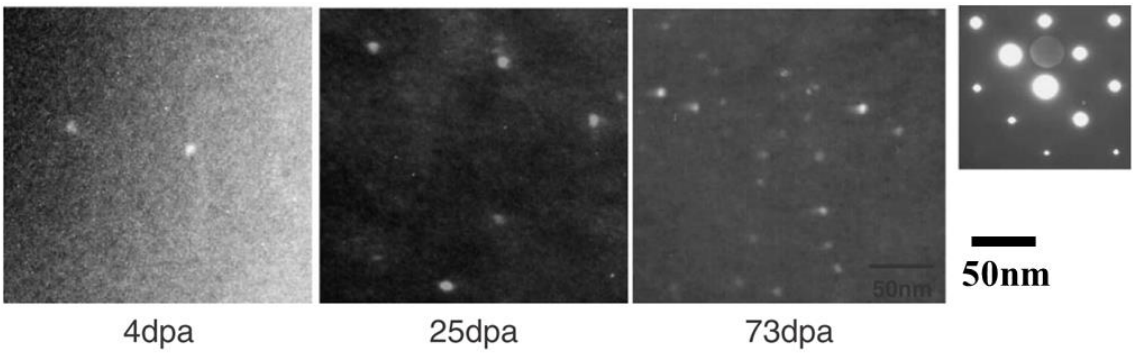

Fig. 1-11 TEM γ’ precipitate images under selected area dark field conditions. The specimen is cold-worked 316 stainless steel irradiated by neutron at 292~ 323°C [32]

- First principle simulation

In fact, the atom map reconstructed from APT technique contains huge quantity of useful information. Around 50% of all the atoms in an APT specimen are captured by APT technique, and their species and position information are all recorded in the atom map.

However, how to interpret the large amount of information is a problem. Many attempts have been previously made to reveal or explain the trend contained in atom maps. In this work, first principle modeling is applied. First principle modeling has atomic scale resolution and is suitable to be compared with the near-atomic-scale atom map. Currently, there is difficulty in simulating the austenite stainless steel by first principle calculation [49], due to the complexity in magnetic spin selection. But the simulation of the γ’ phase precipitates, which are the focus of the APT analysis in this work, could be possible.

- Cross-section sample by focused ion beam (FIB)

The twin-jet thinning electrochemical polishing method is the traditional way to prepare TEM samples. For specimen irradiated by heavy ions, the irradiation damage is concentrated at a certain depth. Therefore it is quite difficult to control the twin-jet parameters so that the TEM thin foil is exactly made at the irradiation damage peak depth.

In this work, cross-section samples are made by FIB technique. It has the advantage that all the depths influenced by irradiation could be observed. The disadvantage is that FIB would cause extra irradiation damage on sample surface, which needs to be removed by careful electro-chemical polishing for very short time.

- Reciprocal lattice rod (relrod) technique

When dpa goes to around 5dpa, the dislocation loops could be too dense to be clearly identified in stainless steel [11]. They may intersect or overlap with each other, making it difficult to confirm their number density. Besides, although Frank loops and perfect loops could be visible under different ***g*** vectors in TEM, the distinguish work could be actually difficult when the stress field observed under TEM is complex due to the existence of very dense loops.

An easier way to identify Frank loops in irradiated stainless steel is to use the relrod technique [50]. It is only sensitive to stacking faults of {111} plane, so only Frank loops will be observed. It shows only one fourth of the existing Frank loops, so the density of visible Frank loops could be much reduced, result in convenience in distinguishing and counting.

The perfect loops density could be deduced from the traditional dark field images with known Frank loop density obtained from the relrod images.

1.4.4 Hardening model for heavy ion irradiation

As neutron irradiation is costly both in time and money, heavy ion irradiation is often used as an alternative tool to study irradiation process and to emulate neutron damage. Unlike neutron irradiation, the damage distribution in heavy ion irradiation is heterogeneous. For example, Shao et al. observed the heterogeneous depth distribution of voids in self-ion irradiated pure iron, as shown in Fig. 1-12 [51]. Therefore, the defect density and average size (N_k, d_k) could be different at different depth of the ion-irradiated material, which makes it difficult to directly apply the Orowan model for hardening explanation.

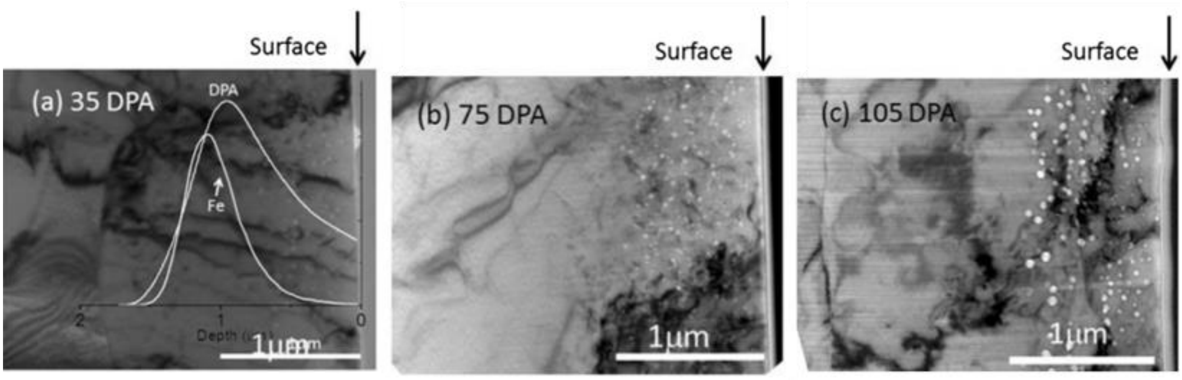

Fig. 1-12 Depth distribution of voids in 3.5 MeV self-ion irradiated pure iron to peak values of a) 35, b) 70, and c) 105 dpa [51]

Sekimura et al. have successfully correlated such defect distribution in heavy ion irradiation with irradiation hardening. By carefully analyzing the load-depth curve of nano-indentation, the contribution of the heterogeneously-distributed defects to hardening is reflected by indentation curve, as shown in Fig. 1-13. However, the quantitative relationship is still unavailable.

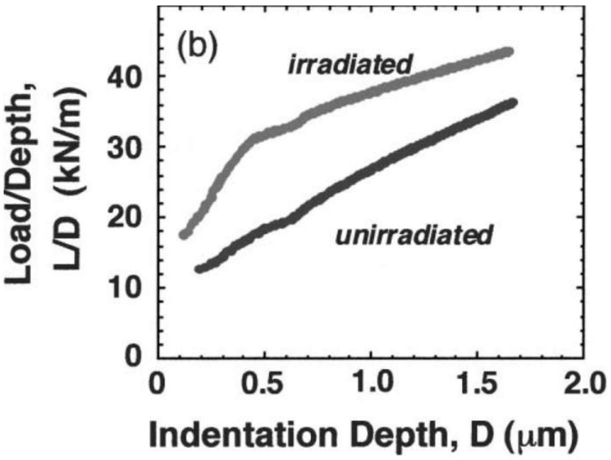

Fig. 1-13 Nano-indentation curve of Fe–0.3Cu alloy irradiated with 12MeV Ni^{3+} ions at 300°C to 9.0 dpa. [52]

As a conclusion, the heterogeneous distribution of defects in heavy ion irradiation makes it difficult to correlate irradiation hardening with microstructure change. The Orowan model for neutron irradiation damage needs to be modified to make it applicable in the case of heavy ion irradiation.

1.5 Research objectives

As discussed above, the main objective of this research is to improve the knowledge base of radiation defect formation for future ageing management standards of stainless steel components in LWRs.

1) As the first step toward the objective, the formation of black dots and Frank loops in stainless steel is isolated by controlling irradiation condition, and their formation mechanisms are discussed by tuning the Si content.
2) By raising irradiation temperature and dose, γ’ precipitates (Ni_3Si) are introduced. The formation mechanisms of γ’ precipitates in stainless steel are analyzed by combining near-atomic scale three dimensional atom maps with first principle calculation, and their possible relationship with dislocation loops are discussed.
3) Additionally, attempts are made to quantitatively correlate these microscopic defects with macroscopic hardening by utilizing the heterogeneous defect depth distribution observed in heavy ion irradiation.

Chapter 2 describes the irradiation details in this study. Model alloy compositions, irradiation conditions and the calculated dpa profile by the SRIM code are shown. Chapter 3 shows the TEM observation results of black dots and dislocation loops, respectively. In Chapter 4, irradiation temperature is raised to 450ºC. γ’ precipitates are formed in this condition, and are analyzed by APT. Their possible relationship with dislocation loop formation is also discussed. The composition deviation in γ’ precipitates is experimentally observed in Chapter 4, and its origin is discussed by first principle calculation in Chapter 5. In Chapter 6, the Orowan model is applied to explain the irradiation hardening by the heterogeneous defect depth distribution observed in Chapter 3.

References in Chapter 1

[1] IAEA, Nuclear Share of Electricity Generation in 2014, http://www.iaea.org/PRIS/

[2] L. Liu, Z. C. Li, N. Sekimura. Ageing management of nuclear power plants in China. E-Journal of Advanced Maintenance, 2015, 7 (1).

[3] IAEA, Ageing Management for Nuclear Power Plants, Vienna, 2009.

[4] IAEA, Material degradation and related managerial issues at nuclear power plants, Vienna, 2005.

[5] IAEA, Assessment and Management of Ageing of Major Nuclear Power Plant Components Important to Safety: PWR Vessel Internals, Vienna, 2009.

[6] JANSI. Inspection and Evaluation Guidelines for PWR Reactor Vessel Internals (Second edition). 2014.

[7] EPRI. Materials Reliability Program: PWR Internals Inspection and Evaluation Guidelines. 2011.

[8] NRC. Degradation of LWR Core Internal Materials due to Neutron Irradiation 2010.

[9] C. Cawthorne, C. Brown. Occurrence of an Ordered Fcc Phase in Neutron-Irradiated M316 Stainless-Steel. J Nucl Mater, 1977, 66 (1-2): 201-202.

[10] H. R. Brager, F. A. Garner. Swelling as a Consequence of Gamma Prime Gamma ' and M23(C,Si)6 Formation in Neutron-Irradiated 316 Stainless-Steel. J Nucl Mater, 1978, 73 (1): 9-19.

[11] K. Fukuya. Current understanding of radiation-induced degradation in light water reactor structural materials. J Nucl Sci Technol, 2013, 50 (3): 213-254.

[12] T. Muroga, N. Sekimura. New insights into the temperature effects on neutron irradiation of structural materials. Fusion Eng Des, 1998, 41: 39-46.

[13] G. S. Was, Fundamentals of Radiation Materials Science: Metals and Alloys, Springer, 2007.

[14] S. G. Song, J. I. Cole, S. M. Bruemmer. Formation of partial dislocations during intersection of glide dislocations with Frank loops in fcc lattices. Acta Mater, 1997, 45 (2): 501-511.

[15] E. H. Lee, L. K. Mansur. Relationships between Phase-Stability and Void Swelling in Fe-Cr-Ni Alloys during Irradiation. Metall Trans A, 1992, 23 (7): 1977-1986.

[16] Z. Jiao, G. S. Was. Novel features of radiation-induced segregation and radiation-induced precipitation in austenitic stainless steels. Acta Mater, 2011, 59 (3): 1220-1238.

[17] A. Etienne, B. Radiguet, P. Pareige, et al. Tomographic atom probe characterization of the microstructure of a cold worked 316 austenitic stainless steel after neutron irradiation. J Nucl Mater, 2008, 382 (1): 64-69.

[18] T. Toyama, Y. Nozawa, W. Van Renterghem, et al. Irradiation-induced precipitates in a neutron irradiated 304 stainless steel studied by three-dimensional atom probe. J Nucl Mater, 2011, 418 (1-3): 62-68.

[19] N. Sekimura, F. A. Garner. Microstructural Evolution of Neutron-Irradiated Fe-Cr-Ni Ternary Alloys at High Helium Generation Rates. J Nucl Mater, 1993, 205: 190-197.

[20] N. Sekimura, F. A. Garner, J. W. Newkirk. Silicons Role in Determining Swelling in Neutron-Irradiated Fe-Ni-Cr-Si Alloys. J Nucl Mater, 1992, 191: 1244-1247.

[21] S. I. Porollo, S. V. Shulepin, Y. V. Konobeev, et al. Influence of silicon on swelling

and microstructure in Russian austenitic stainless steel EI-847 irradiated to high neutron doses. J Nucl Mater, 2008, 378 (1): 17-24.

[22] F. A. Garner, H. R. Brager. The Influence of Mo, Si, P, C, Ti, Cr, Zr and Various Trace-Elements on the Neutron-Induced Swelling of Aisi-316 Stainless-Steel. J Nucl Mater, 1988, 155: 833-837.

[23] T. Okita, W. G. Wolfer, F. A. Garner, et al. Effects of titanium additions to austenitic ternary alloys on microstructural evolution and void swelling. Philos Mag, 2005, 85 (18): 2033-2048.

[24] T. Okita, T. Sato, N. Sekimura, et al. The synergistic influence of temperature and displacement rate on microstructural evolution of ion-irradiated Fe-15Cr-16Ni model austenitic alloy. J Nucl Mater, 2007, 367: 930-934.

[25] W. Van Renterghem, A. Al Mazouzi, S. Van Dyck. Influence of post irradiation annealing on the mechanical properties and defect structure of AISI 304 steel. J Nucl Mater, 2011, 413 (2): 95-102.

[26] T. S. Byun, K. Farrell, E. H. Lee, et al. Temperature effects on the mechanical properties of candidate SNS target container materials after proton and neutron irradiation. J Nucl Mater, 2002, 303 (1): 34-43.

[27] S. J. Zinkle, G. S. Was. Materials challenges in nuclear energy. Acta Mater, 2013, 61 (3): 735-758.

[28] T. Onchi, K. Dohi, M. Navas, et al. Crack initiation mechanism in non-ductile cracking of irradiated 304L stainless steels under BWR water environment. J Nucl Sci Technol, 2006, 43 (8): 851-865.

[29] T. Onchi, K. Dohi, N. Soneda, et al. Mechanism of irradiation assisted stress corrosion crack initiation in thermally sensitized 304 stainless steel. J Nucl Mater, 2005, 340 (2-3): 219-236.

[30] K. Fukuya, M. Nakano, K. Fujii, et al. Role of radiation-induced grain boundary segregation in irradiation assisted stress corrosion cracking. J Nucl Sci Technol, 2004, 41 (5): 594-600.

[31] IAEA, Assessment and management of ageing of major nuclear power plant components important to safety: BWR pressure vessel internals, Vienna, 2005.

[32] K. Fukuya, K. Fujii, H. Nishioka, et al. Evolution of microstructure and microchemistry in cold-worked 316 stainless steels under PWR irradiation. J Nucl Sci Technol, 2006, 43 (2): 159-173.

[33] G. E. Lucas. The Evolution of Mechanical Property Change in Irradiated Austenitic Stainless-Steels. J Nucl Mater, 1993, 206 (2-3): 287-305.

[34] E. H. Lee, E. A. Kenik. Nucleation and Amorphization of Radiation-Produced Phases in a Modified Austenitic Stainless-Steel during Ni-Ion Irradiation. J Mater Res, 1988, 3 (5): 840-844.

[35] P. J. Maziasz. Overview of Microstructural Evolution in Neutron-Irradiated Austenitic Stainless-Steels. J Nucl Mater, 1993, 205: 118-145.

[36] P. J. Maziasz, C. J. Mchargue. Microstructural Evolution in Annealed Austenitic Steels during Neutron-Irradiation. Int Mater Rev, 1987, 32 (4): 190-219.

[37] K. Kondo, Y. Miwa, N. Okubo, et al. Development of corrosion-resistant improved Al-doped austenitic stainless steel. J Nucl Mater, 2011, 417 (1-3): 892-895.

[38] A. Etienne, B. Radiguet, P. Pareige. Understanding silicon-rich phase precipitation under irradiation in austenitic stainless steels. J Nucl Mater, 2010, 406 (2): 251-256.

[39] R. Krummeich, P. Pareige, J. P. Massoud, et al. Solute cluster formation in

austenitic and ferritic alloys under ion irradiation: a three-dimensional atom probe characterization. Surf Interface Anal, 2004, 36 (5-6): 575-580.

[40] P. Pareige, A. Etienne, B. Radiguet. Experimental atomic scale investigation of irradiation effects in CW 316SS and UFG-CW 316SS. J Nucl Mater, 2009, 389 (2): 259-264.

[41] A. Etienne, B. Radiguet, N. J. Cunningham, et al. Atomic scale investigation of radiation-induced segregation in austenitic stainless steels. J Nucl Mater, 2010, 406 (2): 244-250.

[42] K. J. Stephenson, G. S. Was. Comparison of the microstructure, deformation and crack initiation behavior of austenitic stainless steel irradiated in-reactor or with protons. J Nucl Mater, 2015, 456: 85-98.

[43] N. Shigenaka, T. Hashimoto, M. Fuse. Effects of Alloying Elements (Mo, Si) in an Austenitic Stainless-Steel on Dislocation Loop Nucleation under Ion Irradiation. J Nucl Mater, 1993, 207: 46-52.

[44] K. Fukuya, S. Nakahigashi, S. Ozaki, et al. Effects of Phosphorus, Silicon and Sulfur on Microstructural Evolution in Austenitic Stainless-Steels during Electron-Irradiation. J Nucl Mater, 1991, 179: 1057-1060.

[45] Y. Miwa, T. Tsukada, S. Jitsukawa, et al. Effect of minor elements on irradiation assisted stress corrosion cracking of model austenitic stainless steels. J Nucl Mater, 1996, 233: 1393-1396.

[46] Z. Jiao, J. T. Busby, G. S. Was. Deformation microstructure of proton-irradiated stainless steels. J Nucl Mater, 2007, 361 (2-3): 218-227.

[47] H. Watanabe, A. Aoki, T. Muroga, et al. Effect of Combined Addition of Phosphorus and Titanium on Microstructural Evolution in Fe-Cr-Ni Alloys. J Nucl Mater, 1991, 179: 529-533.

[48] R. S. Averback, P. Ehrhart. Diffuse-X-Ray Scattering Studies of Defect Reactions in Electron-Irradiated Dilute Nickel-Alloys .1. Ni-Si. J Phys F Met Phys, 1984, 14 (6): 1347-1363.

[49] T. P. C. Klaver, D. J. Hepburn, G. J. Ackland. Defect and solute properties in dilute Fe-Cr-Ni austenitic alloys from first principles. Phys Rev B, 2012, 85 (17).

[50] D. J. Edwards, E. P. Simonen, S. M. Bruemmer. Evolution of fine-scale defects in stainless steels neutron-irradiated at 275 degrees C. J Nucl Mater, 2003, 317 (1): 13-31.

[51] L. Shao, C. C. Wei, J. Gigax, et al. Effect of defect imbalance on void swelling distributions produced in pure iron irradiated with 3.5 MeV self-ions. J Nucl Mater, 2014, 453 (1-3): 176-181.

[52] N. Sekimura, T. Kamada, Y. Wakasugi, et al. Evaluation of radiation hardening in Fe alloys under heavy ion irradiation by micro-indentation technique. J Nucl Mater, 2002, 307: 308-311.

2. Irradiation procedures

2.1 Model alloys selected for irradiation

Three high purity 316L austenite stainless steel model alloys are selected here. Table 2-1 shows their compositions, and their major difference is Si content. They all meet the ASTM standard for 316L stainless steel [1].

Here model alloys of high purity are selected, so that the effects of Si can be focused on. The effects of other minor elements will not occur to interfere. For example, P has been previously reported to have similar behavior as Si under irradiation [2, 3]. Therefore, a very low content of P is necessary to simplify the mechanism analysis of Si effects.

Table 2-1 Chemical composition of selected 316L stainless steel model alloys

	Alloying elements (wt.%)						Impurity (wt. ppm)				
	Fe	Cr	Ni	Mo	Mn	Si	P	S	Ca	C	N
Low Si (LS)	Bal.	16.9	13.0	2.29	1.00	<0.001	—	<10	—	82	<10
Base Si (BA)	Bal.	17.3	13.2	2.36	0.88	0.42	—	<10	—	111	<10
High Si (HS)	Bal.	17.0	13.5	2.27	0.99	0.95	—	<10	—	97	<10

Also, the model alloys have been solution annealed at 1080°C for 0.5 hours to minimize possible pre-existing dislocation lines or stress fields. In this way, almost all the defects observed after irradiation should be introduced by irradiation process. This will also simplify the mechanism analysis afterwards.

The original grain size of selected model alloys have been confirmed by electron backscatter diffraction (EBSD), as shown in Fig. 2-1. The grain size is not much influenced by Si content, and is all around ~50μm, with quite large scattering. The lath-shaped grains may be twin grains, which usually exist in materials with low stacking fault energy (SFE) [4], such as austenite stainless steel. The homogeneous color in each grain indicates that possible internal stress fields have been quite well removed during solution annealing process.

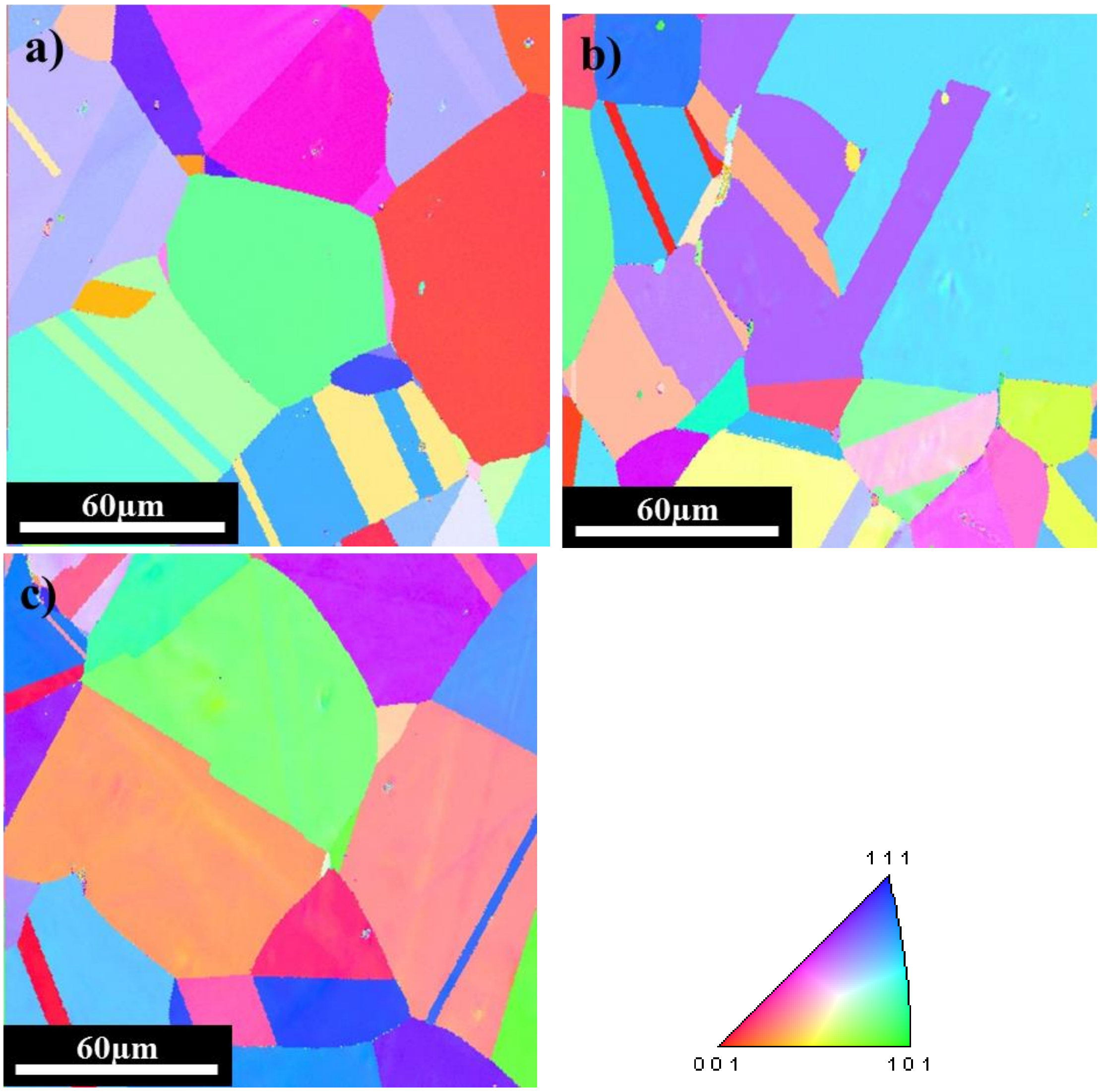

Fig. 2-1 Grain size of unirradiated a) low Si, b) base Si, c) high Si model alloys by EBSD

2.2 Sample preparation for irradiation

Samples for irradiation are prepared by the following procedures:

- Cut into small pieces.

The model alloys are cut into small pieces of around 10×2×0.5mm in dimension. 0.5mm is the thickness, and the surface of 10×2 mm is for irradiation. Thick bulk specimen is used for irradiation to reduce surface sink effects [5].

- Paper polishing.

The surface for irradiation is first polished by emery paper. Samples are polished by 500#, 1500# and 2400# SiO_2 polishing paper in sequence. A clean surface with fine scratches is obtained in this step.

- Buff polishing.

Paper-polished samples are then buff polished by 3μm diamond solution and polishing cloth. A mirror-like surface with minor remaining scratches is obtained.

- Electrochemical polishing.

Finally samples are electrochemically polished by the electrolyte of 90% CH_3COOH and 10% $HClO_4$. The polishing is conducted at around 10ºC for 20s with electric current of ~1A in ice-water bath. After cleaning in, the sample surface should be mirror-like, free of scratches, and are then ready for irradiation. It should remove the possible mechanical damage layer left by paper polishing. Fig 2-2 shows a typical electro-chemical polished sample and its surface morphology under scanning electron microscopy (SEM). It is a cleaning surface with almost no scratches and has an acceptable low density of corrosion pits.

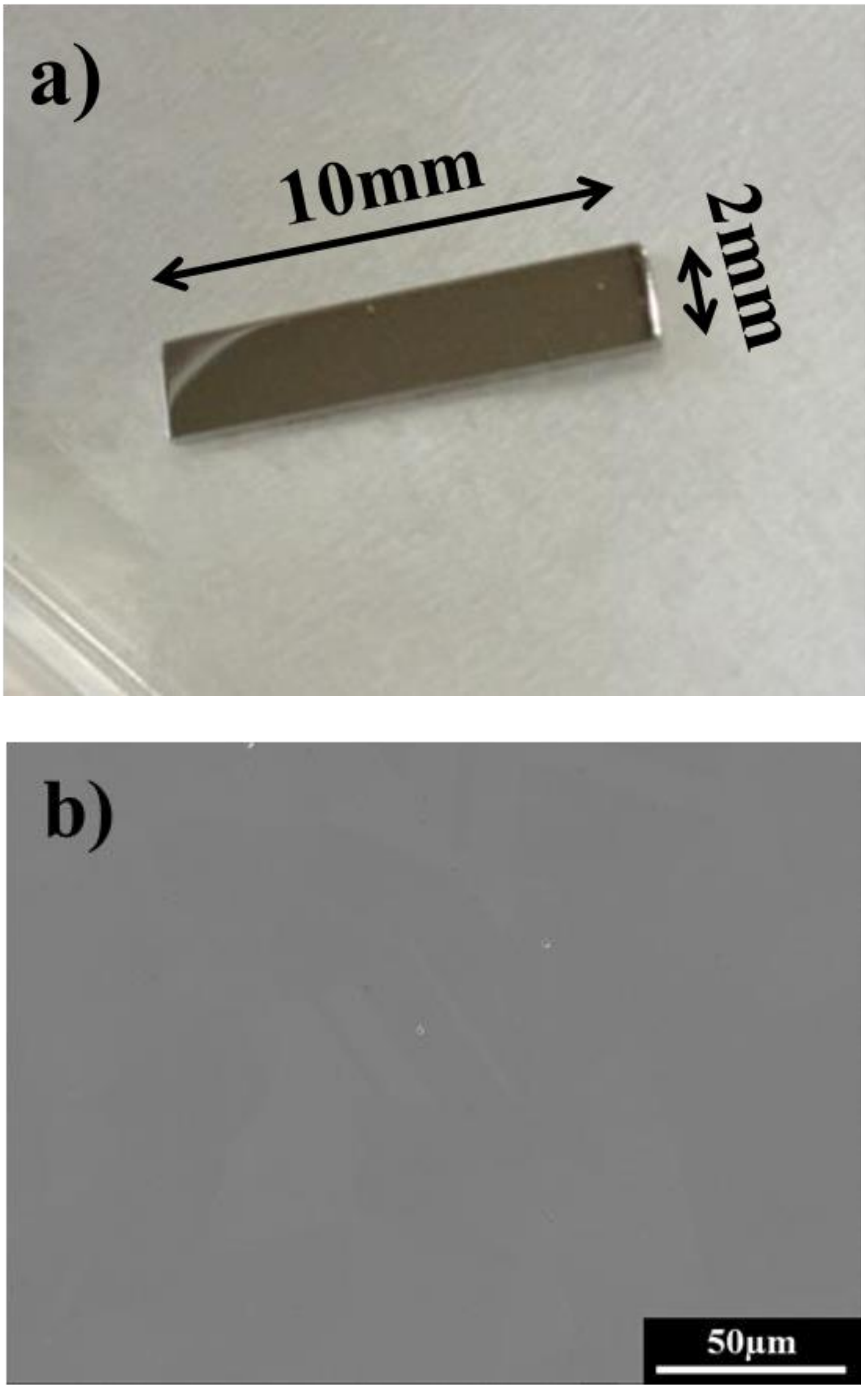

Fig. 2-2 Typical electro-chemical polished sample for irradiation, a) 10×2×0.5mm in dimension, b) surface morphology under SEM

2.3 Heavy ion irradiation

The heavy ion irradiation is performed in beam line 5 and beam line 6 of in High Fluence Irradiation Facility (HIT), at Tokai campus of the University of Tokyo. Tandetron accelerator is used, and 3MeV Fe^{2+} or Ni^{2+} are used as the irradiation particles, to achieve the selected irradiation conditions for defect isolation, as previously shown in Fig. 1-7 in Chapter 1.

In each irradiation, the damage profile is calculated by SRIM 2013 code [6] with displacement energy of 40eV [7-9], as shown in Fig. 2-3. For example, a sample irradiated to 5dpa means the arithmetic average dose from sample top surface the peak dpa depth is 5dpa.

Most of the irradiation works in this study are performed in beam line 5. In beam line 5, the three samples of different Si content are fixed on the same stage, as shown in Fig. 2-4. A total number of 20 Faraday cups are installed at the specimen chamber end to monitor the actual irradiation beam current. Each Faraday cup is 2mm in diameter. The distance between the centers of each two faradays cup is kept at 4 mm, and the 20 Faraday cups are placed in a 5×4 array to ensure a uniform current distribution on the specimen stage. Beam current is checked every 30min to confirm its stability. The vacuum condition is kept at around $\sim 1\times10^{-5}$ Pa during each irradiation.

Irradiation temperature is controlled by both heater and water cooling system, and is online monitored by two thermal couples. The thermal couples are attached to the sample stage, and their signals are transported to the temperature control program. The water cooling system runs all the time during irradiation. When the detected temperature is low, the heater output is automatically increased by the temperature control program; when temperature is high, the heater output is automatically decreased, and due to the running of water cooling system, temperature is decreased. It is a dynamic equilibrium. The temperature fluctuation in reading number during irradiation is less than ±2°C. The metal samples are directly and tightly attached to the metal sample stage without any glues or adhesives between, just to minimize the possible temperature difference between sample and stage.

In heavy ion irradiation in beam line 6, only one thermal couple is used, and it is directly attached to the sample surface, so that the temperature detected is exactly the sample temperature. Beam current is checked every 60min.

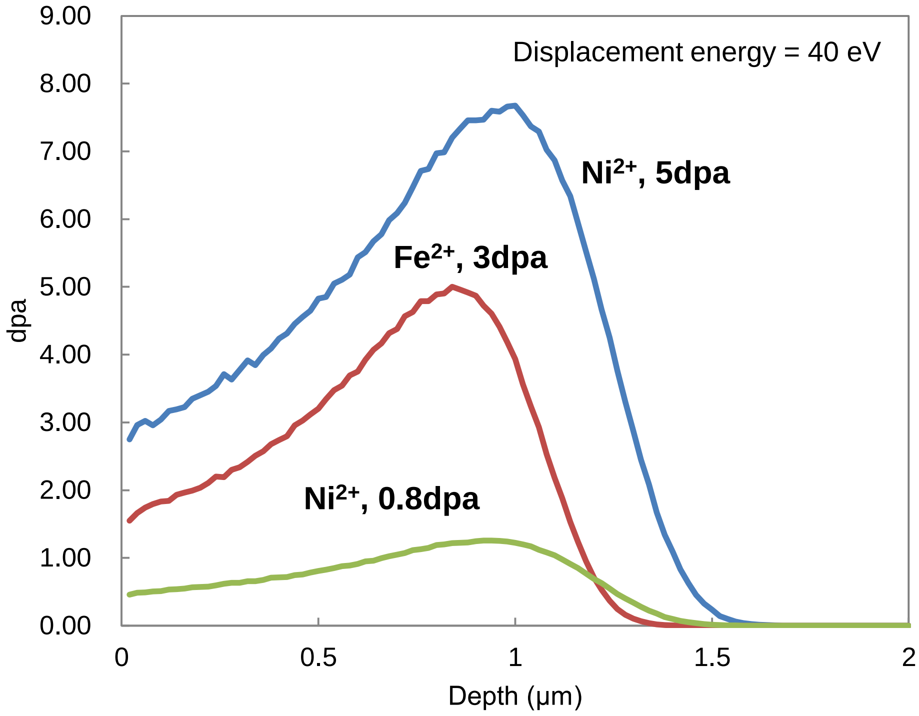

Fig. 2-3 Damage profile calculated by SRIM 2013 code

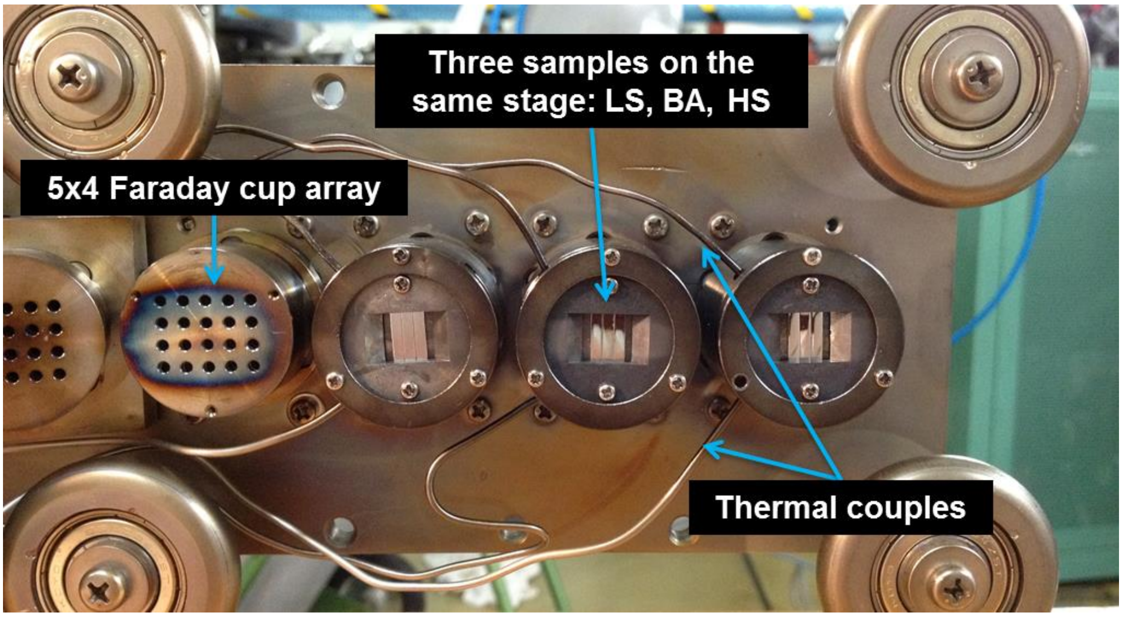

Fig. 2-4 The specimen stage of beam line 5 in HIT facility

The detailed information about all the heavy ion irradiations performed in this study is summarized in Table 2-2. Note that the dose rate in this heavy ion irradiation is controlled at the order of 10^{-4} dpa/s. Other researchers also tend to use this order of dose rate in their heavy ion irradiation experiments [10-16].

Table 2-2 Heavy ion irradiation conditions in HIT facility

Ion	Beam line No.	Temperature (°C)	Fluence (ions/cm^2)	Dose (dpa)	Dose rate (dpa/s)
3MeV Ni^{2+}	6	290	1×10^{15}	0.8	$\sim1\times10^{-4}$
3MeV Fe^{2+}	5	400	5×10^{15}	3	$\sim4\times10^{-4}$
3MeV Ni^{2+}	5	350, 400, 450	7×10^{15}	5	$\sim3\times10^{-4}$

- Possible dose rate effects

It is true that the dose rate in this work is orders higher than that in actual light water reactors (10^{-10}~10^{-8} dpa/s) [17]. This is a common problem that will be faced when trying to use heavy ion irradiation to emulate neutron irradiation damage.

Generally speaking, when irradiation temperature and dose are kept the same, lower dose rate (correspond to longer irradiation time) allows more sufficient point defect diffusion. A theory of irradiation temperature shift has been described in detail by G. Was [18, 19]. It means when considering the number of defects lost to sinks per unit volume is invariant, the irradiation phenomena at lower dose rate and lower temperature are similar to that irradiated at higher dose rate and higher temperature. Quantitative verification has also been attempted [20]. By this theory, the high dose irradiation in this study can give hints to explain the neutron irradiation phenomena at lower temperatures.

To be more detailed on dose rate effects, quantitative relationship has been previously set up in the dose rate region of 10^{-8}~10^{-5} dpa/s by neutron and electron irradiation study. When the irradiation time is fixed, the net vacancy flux, which represent the void growth rate, is proportional to $(\text{dpa/s})^{1/2}$ instead of (dpa/s) [21, 22]. The saturated loop density is also found to be proportional to $(\text{dpa/s})^{1/2}$ instead of (dpa/s)

[23]. Allen et al. found that lower dose rate will lead to greater radiation induced segregation [24]. Since the formation of Ni-Si precipitates is closely related to radiation induced segregation, it is supposed that low dose rate will also promote the formation of Ni-Si precipitates. All these results mean that radiation defect formation is enhanced at lower dose rate when total dpa is fixed.

When try to extrapolate the correlation to higher dose regions, such as to the order of 10^{-2} dpa/s, more data is needed for concluding any quantitative relationship. But the trend is found to be similar. For example, it has also been found that low dose rate shortens the swelling incubation period in this dose rate region [25].

As a conclusion, the higher dose rate in this study is expected to hinder defect formation, and the results in this study can help extend the defect formation database to high dose rate region.

Even if the irradiation conditions with high dose rate in this work cannot be directly compared to a corresponding neutron irradiation condition, it does not mean heavy ion irradiation with high dose rate is meaningless. The microstructure evolution process of stainless steel under irradiation is so complex that the mechanisms of many processes are still unknown. Heavy ion irradiation has the advantages of low cost and easy parameter tuning, so it is usually much easier to discover the microstructure evolution mechanism by ion irradiation. Even though the mechanism discovered in heavy ion irradiation may be somehow different from that in neutron irradiation due to the difference in dose rate, it can greatly inspire and simplify the research work needed in neutron irradiation. This is the contribution of heavy ion irradiation to understanding the neutron irradiation damage.

- Possible cascade effects

Another issue that needs to be considered in high dose rate irradiation is the effect of cascades. When dose rate is high, irradiation cascades are created at a high rate in the material, which may lead to overlapping between these cascades.

The average spacing between cascades could be roughly estimated in this experiment. The irradiation current detected by the Φ2mm Faraday cup is at the order of ~5×10^{-9}A, so the flux is roughly ~5×10^{11} cm^{-2} s^{-1}. When considering the lifetime (formation plus quenching) of cascades, which is at the order of 1×10^{-11} s, the average spacing between cascades is estimated to be at the order of millimeters, much larger than the size of cascades themselves (usually at the order of several tens of nanometers). Even when the thermal phase is also considered by applying the lifetime of 1×10^{-6} s (Fig. 1-4), the average spacing is still at the order of 10^{-5} m, which is also much larger than the cascades size. Thus, the cascade overlapping could be ignored here.

The voltage of irradiation ions and dose rate are not tuned in the experiment, so the stability of radiation defects under cascades is not the focus in this study. It needs to be discussed in future works.

References in Chapter 2

[1] ASTM. Standard Specification for Chromium and Chromium-Nickel Stainless Steel Plate, Sheet, and Strip for Pressure Vessels and for General Applications. A 240/A 240M - 2004.

[2] K. Fukuya, S. Nakahigashi, S. Ozaki, et al. Effects of Phosphorus, Silicon and Sulfur on Microstructural Evolution in Austenitic Stainless-Steels during Electron-Irradiation. J Nucl Mater, 1991, 179: 1057-1060.

[3] N. Sekimura, F. A. Garner, J. W. Newkirk. Silicons Role in Determining Swelling in Neutron-Irradiated Fe-Ni-Cr-Si Alloys. J Nucl Mater, 1992, 191: 1244-1247.

[4] W. Van Renterghem, A. Al Mazouzi, S. Van Dyck. Influence of post irradiation annealing on the mechanical properties and defect structure of AISI 304 steel. J Nucl Mater, 2011, 413 (2): 95-102.

[5] S. Ishino, K. Fukuya, T. Muroga, et al. Insitu Microstructural Observation of Radiation-Damage in Nickel Produced by Energetic Heavy-Particles. J Nucl Mater, 1984, 122 (1-3): 597-601.

[6] J. F. Ziegler. http://www.srim.org/.

[7] K. Fujii, K. Fukuya. Effects of radiation on spinodal decomposition of ferrite in duplex stainless steel. J Nucl Mater, 2013, 440 (1-3): 612-616.

[8] J. T. Busby, M. M. Sowa, G. S. Was, et al. Post-irradiation annealing of small defect clusters. Philos Mag, 2005, 85 (4-7): 609-617.

[9] A. Lupinacci, K. Chen, Y. Li, et al. Characterization of ion beam irradiated 304 stainless steel utilizing nanoindentation and Laue microdiffraction. J Nucl Mater, 2015, 458: 70-76.

[10] J. Gan, E. P. Simonen, S. M. Bruemmer, et al. The effect of oversized solute additions on the microstructure of 316SS irradiated with 5 MeV Ni++ ions or 3.2 MeV protons. J Nucl Mater, 2004, 325 (2-3): 94-106.

[11] A. Etienne, B. Radiguet, P. Pareige. Understanding silicon-rich phase precipitation under irradiation in austenitic stainless steels. J Nucl Mater, 2010, 406 (2): 251-256.

[12] A. Etienne, B. Radiguet, N. J. Cunningham, et al. Atomic scale investigation of radiation-induced segregation in austenitic stainless steels. J Nucl Mater, 2010, 406 (2): 244-250.

[13] A. Etienne, B. Radiguet, N. J. Cunningham, et al. Comparison of radiation-induced segregation in ultrafine-grained and conventional 316 austenitic stainless steels. Ultramicroscopy, 2011, 111 (6): 659-663.

[14] A. Etienne, M. Hernandez-Mayoral, C. Genevois, et al. Dislocation loop evolution under ion irradiation in austenitic stainless steels. J Nucl Mater, 2010, 400 (1): 56-63.

[15] T. Miura, K. Fujii, K. Fukuya, et al. Influence of crystal orientation on hardness and nanoindentation deformation in ion-irradiated stainless steels. J Nucl Mater, 2011, 417 (1-3): 984-987.

[16] T. Okita, T. Sato, N. Sekimura, et al. The synergistic influence of temperature and displacement rate on microstructural evolution of ion-irradiated Fe-15Cr-16Ni model austenitic alloy. J Nucl Mater, 2007, 367: 930-934.

[17] K. Fukuya. Current understanding of radiation-induced degradation in light water reactor structural materials. J Nucl Sci Technol, 2013, 50 (3): 213-254.

[18] G. S. Was, Fundamentals of Radiation Materials Science: Metals and Alloys, Springer, 2007.

[19] G. S. Was, T. Allen. Intercomparison of Microchemical Evolution under Various Types of Particle Irradiation. J Nucl Mater, 1993, 205: 332-338.

[20] G. S. Was, J. T. Busby, T. Allen, et al. Emulation of neutron irradiation effects with protons: validation of principle. J Nucl Mater, 2002, 300 (2-3): 198-216.

[21] T. Okita, T. Kamada, N. Sekimura. Effects of dose rate on microsturctural evolution and swelling in austenitic steels under irradiation. J Nucl Mater, 2000, 283: 220-223.

[22] T. Okita, T. Sato, N. Sekimura, et al. The primary origin of dose rate effects on microstructural evolution of austenitic alloys during neutron irradiation. J Nucl Mater, 2002, 307: 322-326.

[23] H. Watanabe, A. Aoki, H. Murakami, et al. Effects of Phosphorus on Defect Behavior, Solute Segregation and Void Swelling in Electron-Irradiated Fe-Cr-Ni Alloys. J Nucl Mater, 1988, 155: 815-822.

[24] T. R. Allen, J. I. Cole, E. A. Kenik, et al. Analyzing the effect of displacement rate on radiation-induced segregation in 304 and 316 stainless steels by examining irradiated EBR-II components and samples irradiated with protons. J Nucl Mater, 2008, 376 (2): 169-173.

[25] A. S. Kalchenko, V. V. Bryk, N. P. Lazarev, et al. Prediction of swelling of 18Cr10NiTi austenitic steel over a wide range of displacement rates. J Nucl Mater, 2010, 399 (1): 114-121.

3. Formation of black dots and dislocation loops

3.1 Methodology

3.1.1 Cross-section sample preparation

To observe depth distribution of dislocation defects, it is necessary to prepare cross-section samples for TEM. By FIB technique, it is quite easy to extract cross-section samples from the bulk. However, FIB process would also introduce extra irradiation damage on the surface of cross-section sample by the Ga beam it uses. Such extra damage will make it difficult for TEM observation of defects that are caused by the heavy ion irradiation.

There are generally two candidate methods to remove or lessen the extra FIB irradiation damage:

- Gentle mill by Ar ions.

Gentle mill bombards low energy Ar ions onto the surface of cross-section samples at a small angle of incidence. Such Ar beam will slowly remove the damage layer caused by Ga ion polishing, but it will also cause new irradiation damage layer by itself. Due to its low energy and small incidence angle, the new damage layer could be very thin.

The advantage of gentle mill is that the slow polishing rate makes it easy to control the final sample thickness for TEM. The disadvantage is the very thin damage layer of Ar irradiation left by gentle mill.

- Electrochemical polishing.

The electrochemical polishing can completely remove the Ga irradiation damage without causing extra irradiation damage, so that nice TEM samples could be made. The disadvantage is that the polishing rate is too high that the polishing condition (especially the polishing time) is very difficult to control. Besides, the electrochemical polished samples are susceptible to oxidation.

Both two methods have been attempted in this work. The TEM samples made through the gentle mill method turned out to be not so satisfactory for observation, since the tiny defects introduced by Ar mill cannot be neglected indeed.

Thus, for the aim of high-resolution and high-reliability TEM observation, the electrochemical polishing method is used as the only method in this study. Since the difficulty in electrochemical polishing is quite large, much work has been done on developing the methodology with appropriate parameters. The developed sample preparation process is listed here:

- Sample cross-section extraction and pre-thinning

The FIB machine used in this study is Hitachi FB-2100. First of all, a layer of tungsten is deposited on the irradiated sample surface to avoid too much Ga damage. A slice of cross-section sample is extracted and welded onto a 3mm TEM semi-disk within the chamber of FIB machine. The cross-section sample covers the range from top sample surface to ~4μm depth, which surely covers all the depths that is influenced by heavy ion irradiation (<2μm, as shown in Fig. 2-3).

The cross-section sample is further pre-thinned by 40kV Ga beam of FIB to ~200nm thick. The morphology of pre-thinned sample is observed under SEM, as shown in Fig. 3-1.

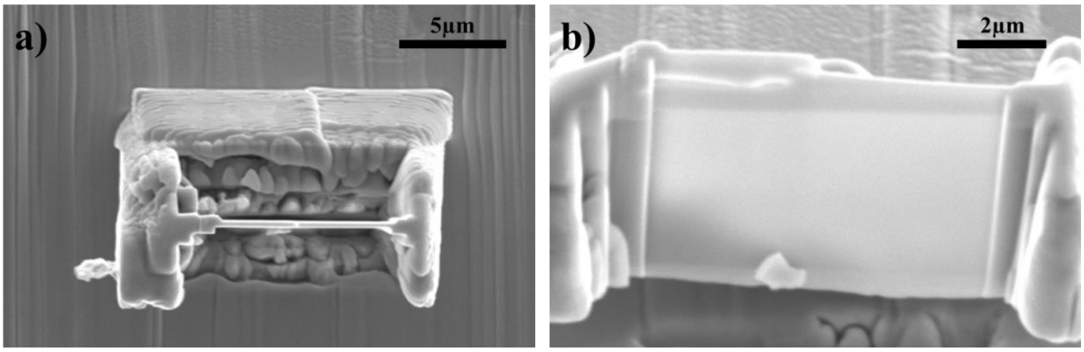

Fig. 3-1 Typical pre-thinned cross-section sample under SEM, a) top view, b) side view

- Parameters for electrochemical polishing

Pre-thinned sample is then electrochemically polished by electrolyte of 5% perchloric acid and 95% ethanol at ~3°C in an ice-water bath. The polishing voltage is 40V, and the polishing time is only 0.01~0.1sec.

There isn’t a proper commercial timer for such short polishing time, so a resistor–capacitor (RC) timing circuit is made here to generate instant voltage pulse. The duration of the voltage pulse is controlled by the type of resistor installed, and the output wave is confirmed by an oscilloscope. An overview of the electrochemical polishing system is shown in Fig. 3-2.

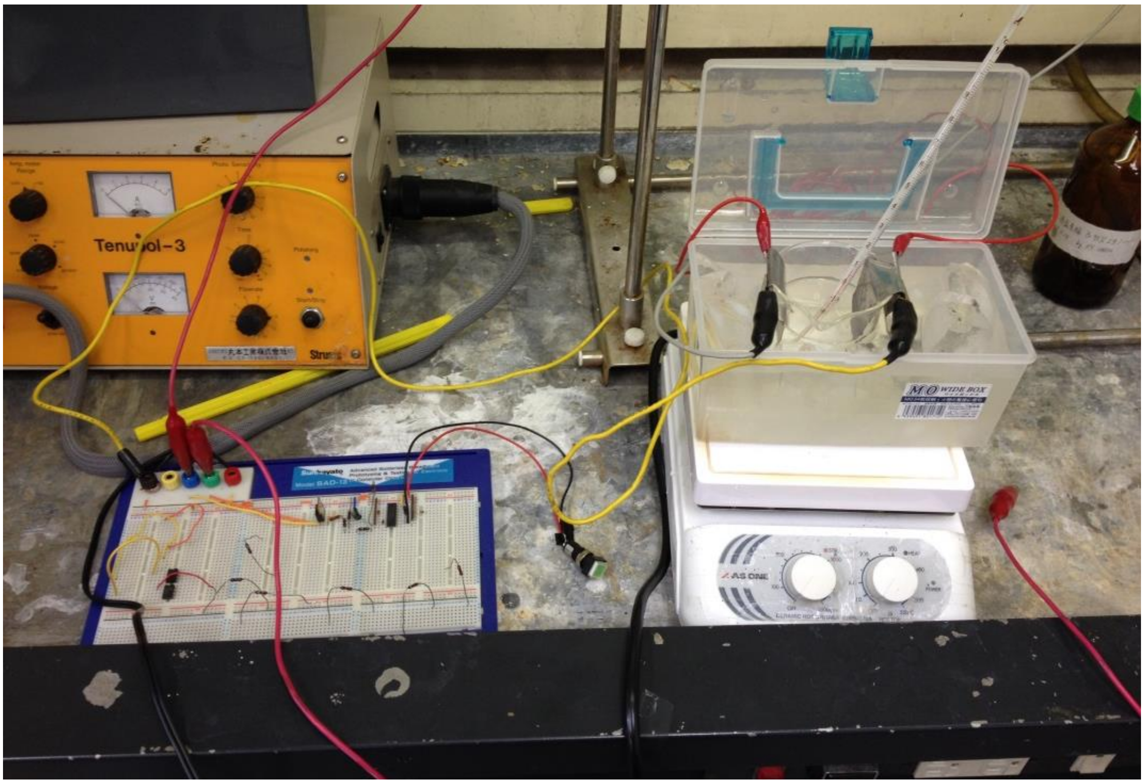

Fig. 3-2 An overview of the electrochemical polishing system

The purpose of electrochemical polishing is to remove the FIB damage and finalize the TEM specimen thickness to be in the range of about 60~160nm. The result of the electrochemical polishing is later confirmed by TEM observation. The region beyond depth of 2μm should be almost defect-free under TEM; otherwise it indicates the FIB damage was not successfully removed by electrochemical polishing. The sample thickness is inferred by thickness fringes. The thickness near the surface region is usually around 100nm or less, and thickness increases as depth increases. The thickness at the damage peak depth is usually around 130~160nm.

The prepared TEM samples are preserved in desiccators, but they should be observed under TEM as quickly as possible to avoid oxidation.

3.1.2 TEM observation techniques

JEOL JEM-2000FX and JEM-2100 are the TEM used in this study. The acceleration voltage is 200kV.

Traditionally, to obtain high resolution TEM images of dislocation loops, the technique of weak beam dark field (WBDF) image is often applied [1]. However, when dislocation loops are very dense, their stress fields may interact and become difficult to be distinguished under WBDF. Also, the procedures to tell apart Frank loops (***b***=<111>) and perfect loops (***b***=<110>) by WBDF is quite complicated, as several ***g*** vectors need to be carefully selected for observation.

Edwards et al. proposed the reciprocal lattice rod (relrod) technique for better observation of Frank loops [2]. As we know, each Frank loop has one {111} plane stacking fault, and such stacking faults can produce extra diffraction spots, or called relrods, on the diffraction map, as illustrated in Fig. 3-2. By tilting the TEM specimen ~7° off the <110> zone axis while maintaining g=<113> dynamic two beam condition, one relrod is intensified. By selecting the relrod using objective aperture, the edge-on Frank loops are visible in dark field image as short bright dash.

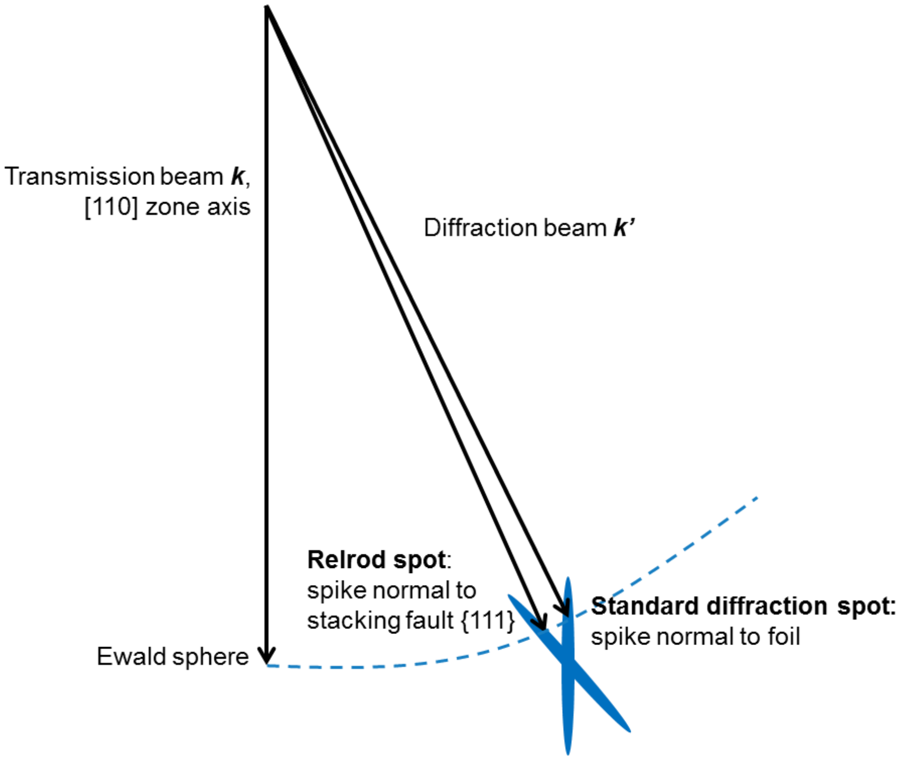

Fig. 3-2 A schematic of relrod observation technique in TEM

As there are in total four variants of {111} stacking faults and here only one is selected, the visible Frank loops are only 1/4 of the total number of Frank loops. Also, since perfect loop has no stacking fault, it will not appear in the relrod dark field image. Therefore, relrod image offers Frank loop observation in high contrast, without the interference from loop overlapping or possible perfect loops existed.

Both WBDF and relrod techniques are used in this study for dislocation loop observation under TEM. The sample thickness is estimated under ***g***=<200> and ***g***=<111> by thickness fringes [3].

3.2 Black dot formation

Black dots are supposed to form in conditions that diffusivities of point defects are limited, or in other words, low temperature irradiation conditions. Here, a typical LWR temperature 290°C is selected. Low Si and high Si samples are irradiated to ~0.8 dpa at 290°C, and the desired microstructure with black dots as the major defects is successfully obtained.

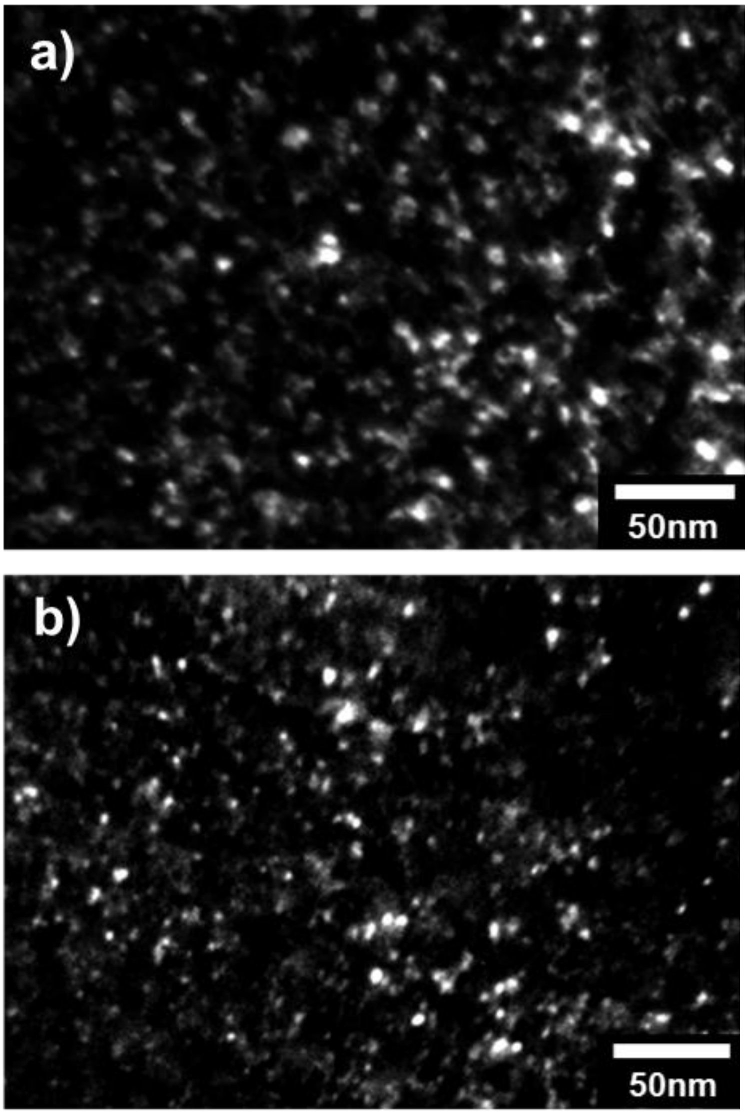

Fig. 3-3 TEM dark field image of a) low Si, b) high Si sample irradiated at 290°C to 0.8dpa (***g***=<111>). The images are taken at the peak dpa depth.

Fig. 3-3 shows the typical ***g***-3***g*** weak beam dark field image of low Si and high Si sample at the peak dpa depth under ***g*** vector of <111>. Tiny and dense black dots are found to be the major type of defects in both two samples, and precipitates or voids are not observed in this condition. The element distribution of these two samples has also been confirmed under APT, and no visible Ni-Si precipitates are found in the atom map.

A count of black dot density and size is performed under different ***g*** vectors, as shown in Table 3-1. For each observation condition, the number of counted black dots is more than 100; but in the case of ***g***=<220> in high Si sample, the count is 38. As we know, all dislocation defects with Burgers vector in <111> direction will be visible under ***g*** vector of <111> or <200>, while only 50% of such defects will be visible under ***g*** vector of <220>. In Table 3-1, the number density of black dots counted under ***g*** vector <220> is about half of that counted under g vector <200> or <111>, while their size are similar. This indicates the majority of black dots observed here are Frank loops in nature with Burgers vector of a_0/3<111>. Pokor et al. also came to the similar conclusion that black dots are actually small Frank loops in nature by density and size comparison [4].

Table 3-1 Black dot number density and size counted under different ***g*** vectors.

	Si	***g*** vector	Number density	Average size	Size standard deviation
	wt.%		x10^{22} m^{-3}	nm	nm
Low Si	~0	<111>	5.2±0.2	4.2	1.5
		<220>	2.9±0.2	3.9	1.6
High Si	0.95	<111>	5.2±0.5	3.8	1.0
		<200>	4.1±0.4	4.4	1.4
		<220>	2.1±0.3	5.4	1.7

When comparing the low Si and high Si sample in Table 3-1, it can be drawn that the black dot number density and average size in the two samples are almost the same in value. Thus, the addition of Si does not show much effect on black dot formation. The number density of black dots in high Si sample may seem a little lower, but as the counting uncertainty here might be quite large due to the very tiny size and possible overlapping of black dots, it could still be within the counting error range.

As a conclusion, the microstructure with black dots as the major type of radiation defect has been successfully obtained by ion irradiation at 290°C to 0.8dpa. No evident change is introduced on both black dot number density and average size by the addition of Si. The observed black dots should be mainly Frank loops in nature.

3.3 Frank loop formation affected by Si at 400°C

Frank loops tend to form at higher temperature and higher dpa. Therefore, the three compositions of model alloys are irradiated at 400°C to 3dpa to try to produce Frank loops as the major type of irradiation defects.

The specimen prepared by FIB technique from the irradiated bulk alloys are observed by TEM under different ***g*** vectors. Fig. 3-4 shows the dynamic bright field images at the damage peak depth of the three samples under the ***g*** vector of <200>. Frank loops are observed to be the major defects. Black dots exist, but are in low density compared to Frank loops. No visible voids or precipitates are observed under TEM. The depth distribution of Frank loops is measured here to discuss the inhomogeneous depth distribution of radiation defects in heavy ion irradiation [5-8].

3.3.1 Depth distribution of Frank loops

Although the contrast of Frank loops in Fig. 3-4 is quite good, the loops are still too dense to be accurately counted. Therefore, relrod images are applied here for detailed loop analysis instead of traditional bright field or dark field images. Fig. 3-5 is the relrod image of sample cross section, covering the regions from sample top surface to around 1µm depth along the irradiation beam direction. The white dash marks the irradiation depth, and the white circle in the diffraction pattern is the position where objective aperture is placed at. The distribution of Frank loops is observed to be inhomogeneous. In near surface region, Frank loop density is low. Loop density increases with depth, and reaches maximum in region around 800~900nm depth. In deeper regions, loops rapidly decrease in number density, and finally disappear in regions beyond ~1.1µm depth. Average size of Frank loops also reaches maximum at roughly 800~900nm depth, which is similar to the number density distribution. But the change in size is not as evident as that in number density.

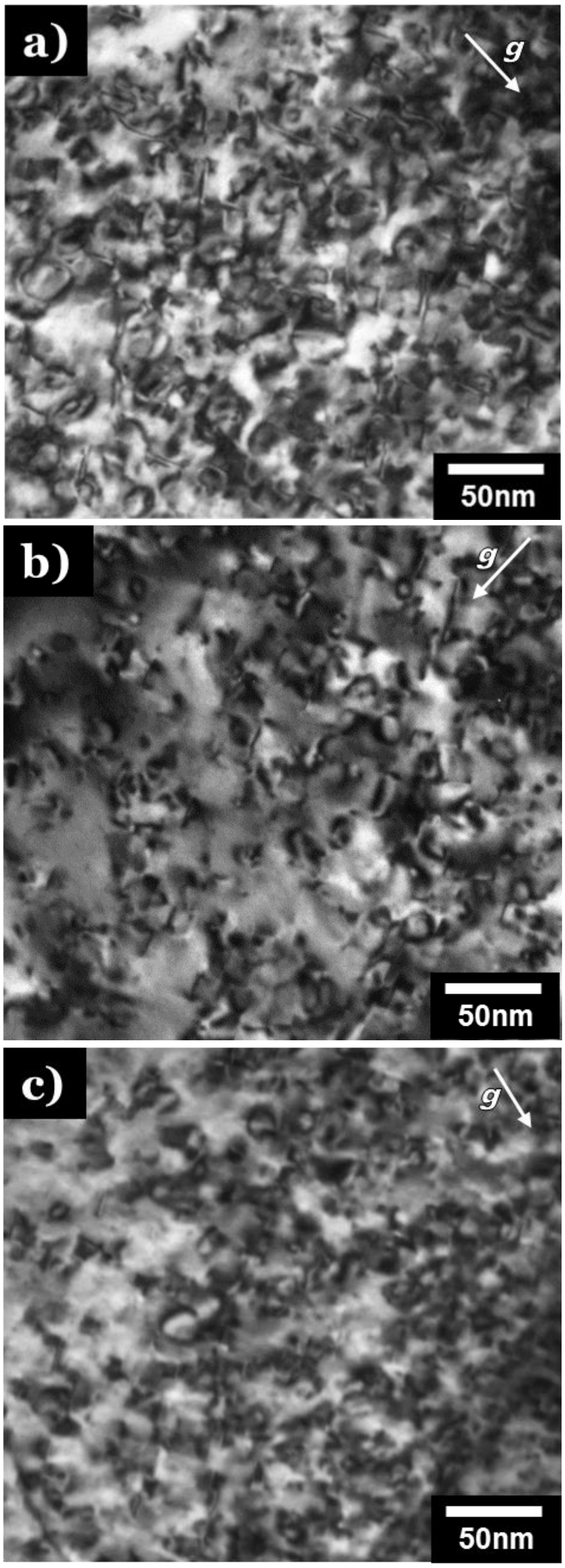

Fig. 3-4 TEM dynamic bright field images at the damage peak depth of a) low Si, b) base Si, c) high Si samples irradiated at 400°C to 3dpa (***g***=<200>).

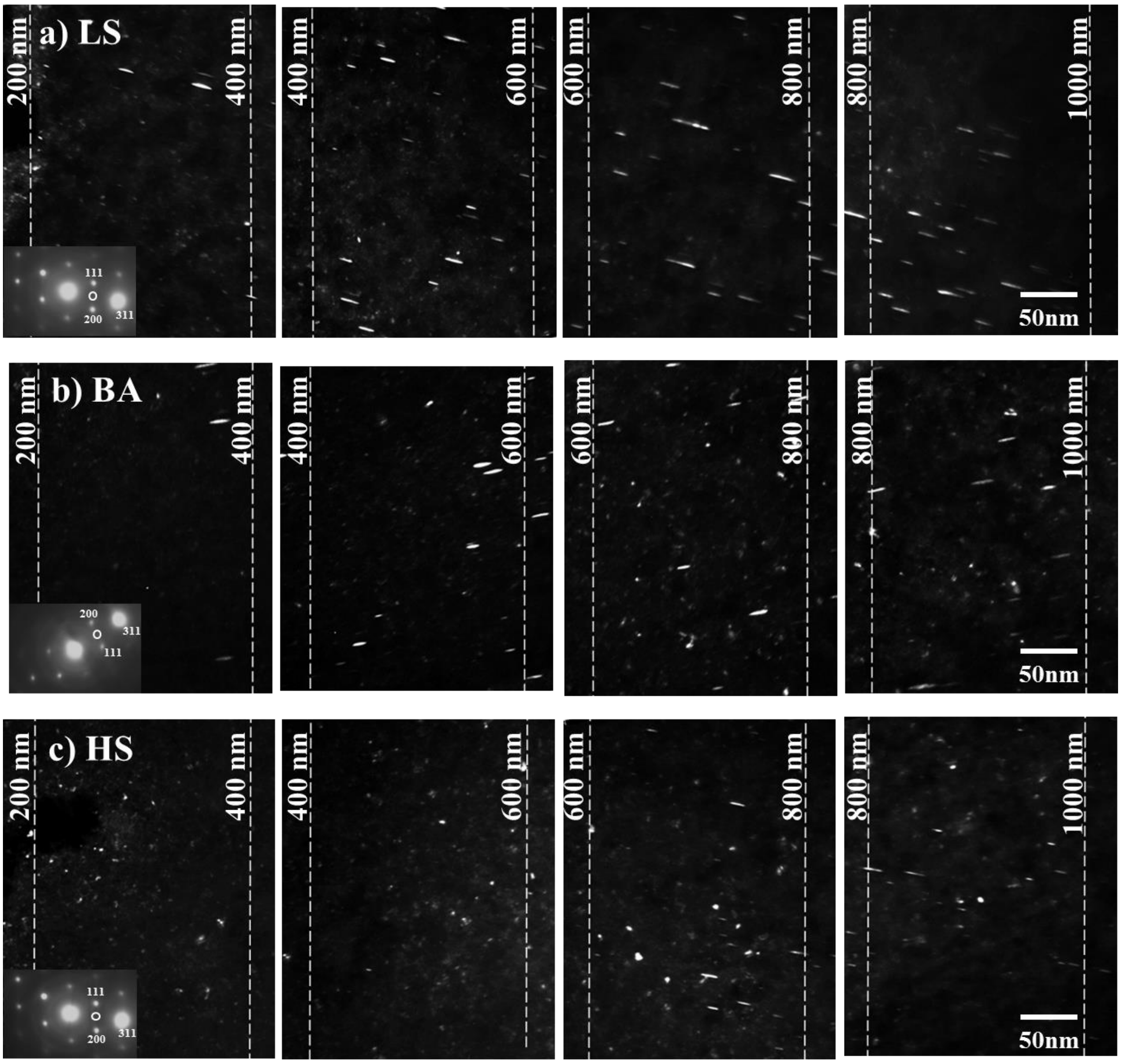

Fig. 3-5 Low magnification TEM relrod images of a) low Si, b) base Si, c) high Si samples irradiated at 400°C to 3dpa. The white dash marks the irradiation depth. The white circle in the diffraction pattern is the position where objective aperture is placed at.

The quantitative Frank loop data are counted in each 200nm depth interval parallel to the sample surface. The loop number density and average size in each region is averaged from the counting results of 3~4 high magnification relrod images (×200k) taken at the same depth but at different positions. The very top region of 0~200nm depth is not analyzed here, because of the interference of inevitable FIB damage existed from sample top surface to around 30nm depth. The error bars of defect number density is calculated by assuming Poisson distribution error in counting, which means count error equals the square root of the count number.

The counting results of Frank loops at different depth are listed in Table 3-2, and the corresponding depth distribution is plotted in Fig. 3-6. The loop number density is at the order of $10^{22}m^{-3}$ and the average size is around 10nm, this matches the previous TEM observation results [9, 10]. The peak dpa depth calculated by SRIM code is marked in the figure for reference. As we know, the dpa profile calculated by SRIM code indicates the differences in damage production rate at different depths, and does not take temperature or diffusion into consideration.

Thus, it is quite surprising to see that in low Si (0% Si) and base Si (0.42% Si) samples, the depth distribution of Frank loop number density is very similar with the dpa profile calculated by SRIM code in Fig. 2-3. But in high Si sample (0.95% Si) its density distribution curve does not follow the calculated dpa in the shallower region (depth<600nm). The change in average size at different depths is not so much compared to Frank loop number density, as shown in Figure 3-6 (b). Only an increase in average size at around the damage peak depth could be distinguished. In fact, the distribution curve of average size does not show a very clear trend here, as the data scattering cannot be ignored. This is most probably caused by the relatively larger counting error when measuring average loop size. Although relrod image can clearly reveal Frank loops with diameter above 3nm, the contrast is usually weak and the distinguishing work could be difficult for tiny Frank loops around 1~2nm. If one or two tiny Frank loops are mistakenly missed during counting process, its number density will not be much influenced, but its average size will be quite overestimated.

Table 3-2 Frank loops counted at different depths in the samples irradiated at 400°C to 3dpa. Counting is performed in relrod images. The thickness of cross-section sample increases as depth increases.

	Depth	Loop Count	Loop density	Loop average size	Loop density error	Loop size error
	nm	count	$10^{21}/m^3$	nm	$10^{21}/m^3$	nm
LS (0% Si)	300	53	13	9.4	1.7	6.4
	500	89	13	9.4	1.4	4.8
	700	179	21	9.6	1.5	5.5
	900	218	23	11.9	1.6	5.7
	1100	117	17	6.9	1.6	2.5
	1300	4	0.42	9.9	0.21	2.7
BA (0.42% Si)	300	19	8.1	9.4	1.9	3.5
	500	41	9.2	7.9	1.4	4.2
	700	59	15	8.9	2.0	4.8
	900	116	17	9.0	1.6	4.7
	1100	61	9.7	6.6	1.2	2.0
	1300	0	0	-	0	-
HS (0.95% Si)	300	2	0.83	3.8	0.59	0.8
	500	6	1.0	3.8	0.42	0.7
	700	91	12	6.6	1.3	3.2
	900	118	15	6.0	1.4	2.9
	1100	38	5.8	5.7	0.95	1.1
	1300	0	0	-	0	-

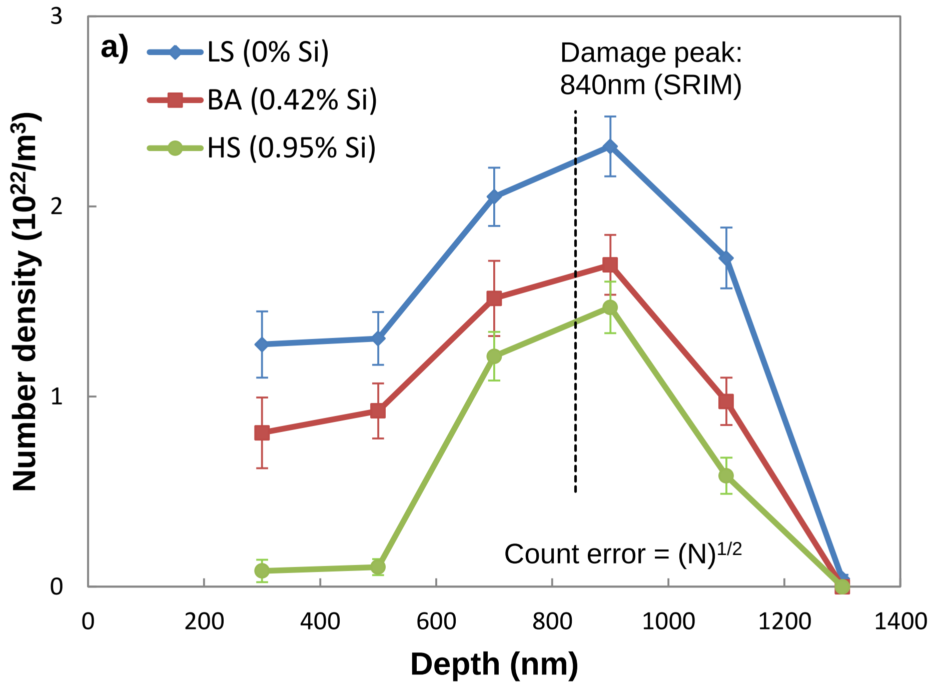

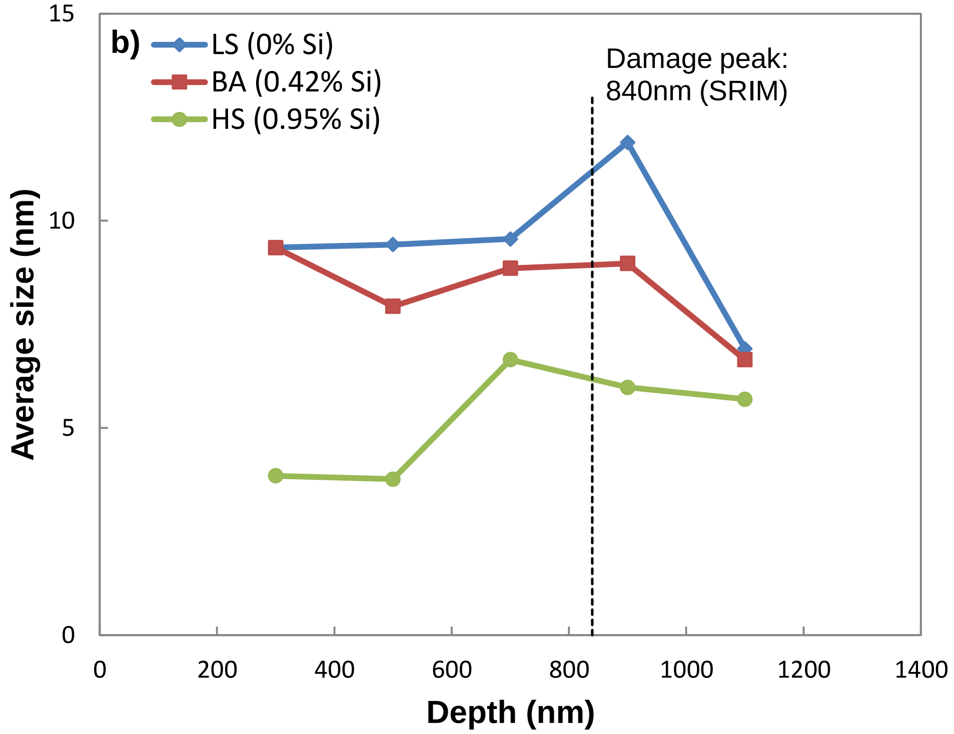

Fig. 3-6 Depth distributions of Frank loop a) number density and b) average size in 400°C and 3dpa irradiated samples. Measurement is performed in relrod images.

Similar phenomena have been previously observed in cavity formation that cavity density changes at different depths while its average size is almost independent of depth [11, 12]. It indicates that in low Si and base Si samples, the nucleation of Frank loops at a certain depth is determined by the damage production rate there, while loop growth is affected by some other factors as well.

The Si effects on Frank loop formation are distinct here. As shown in Fig. 3-6, Both Frank loop number density and average size monotonically decreases at all the depths as Si content increases. Actually in high Si sample, the Frank loop number density is almost zero in the near-surface region (200~600nm), which directly leads to a density distribution curve that is very different from the dpa profile. The addition of Si to 0.95wt.% should have altered the point defect diffusion process and made the Frank loop nucleation no longer determined by damage production rate.

3.3.2 Size distribution of Frank loops

Since the results of Frank loop average size could be misleading due to the possible error discussed above, a detailed loop size distribution in damage peak region (600~1000nm depth) is checked under relrod image, with >200 loop counts for each sample, as shown in Fig. 3-7. Frank loops in high Si sample are mainly in the range of around 2~7nm, while in low Si and base Si sample they have a broader distribution. This curve shape change seems to indicate that Si addition narrows the size distribution curve of Frank loops, but the possibility of a left-shift of the curve caused by Si addition cannot be ruled out here. Actually as 1~2nm is near the resolution limit here, a peak shift may exist but not be detected [13].

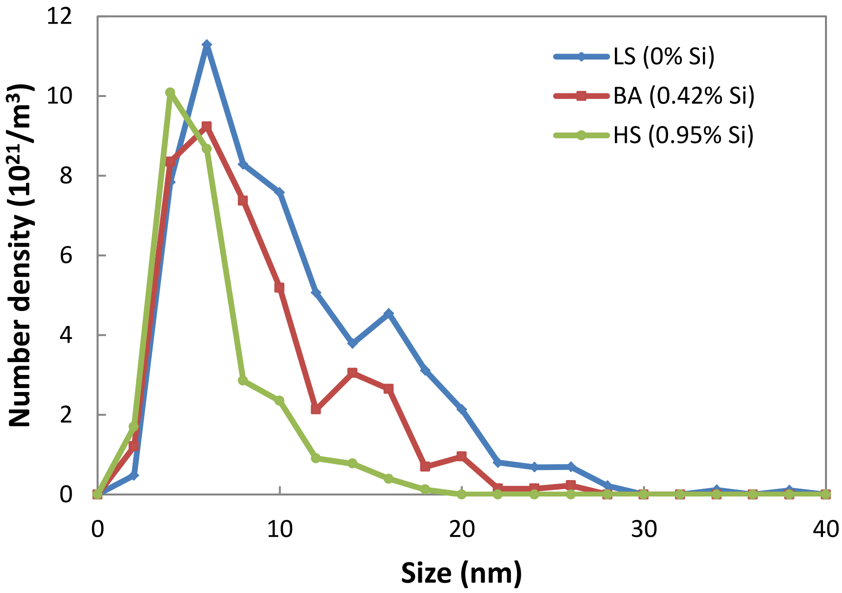

Fig. 3-7 Frank loop size distribution in the damage peak region (600~1000nm depth) of model alloys irradiated at 400°C to 3dpa

In Fig. 3-7, there seems to have a second peak at 16~19nm for low Si sample and at 12~16nm for base Si sample, as marked by the arrows. In high Si sample the second peak may still exist but just be hard to observe due to the suppressed loop size. It is difficult to say if such second peaks are statistically significant, or are just artifacts brought up by data processing. Possible artifacts could be caused by the limitation of loop counts or the choice of bin width, etc. However, such insignificant second peaks have been previously observed in ~300°C neutron irradiation, and the reported loop sizes for the first and second peaks are also ~5 and ~15nm, respectively [2, 14, 15]. In the result of Edwards et al., the second peak appears only in high purity 304/316 steel with lower Si content, which is consistent with our results [2]. If exists, the bi-modal loop size distribution suggests different growth mechanisms for Frank loops at two peaks. Or to be more precise, some fraction of the small Frank loops (4~10nm) can hardly grow larger. Maybe the larger loops grow at an earlier stage of microstructure evolution, and have left limited space for other loops to grow. More works are needed to verify this phenomenon and to clarify its inner mechanism.

3.3.3 Discussion

In the irradiation at 400°C to 3dpa, Frank loops is observed to be the major type of radiation defect. By increasing the Si content of irradiated model alloys, substantial decrease in Frank loop density and average size are observed by TEM, especially in the near surface region. In literature, Miwa et al. have found Frank loop density as well as irradiation hardening has been suppressed by Si addition [16, 17]. But more researchers have observed Frank loops to be refined by Si addition, which means larger loop number density and smaller loop size with Si addition [18-20].

Such contradiction in literature data should be caused by the fact that Si could play multiple roles during microstructure evolution. In different irradiation conditions, the dominant role of Si may change, resulting in different density and size of Frank loops observed in literature. The discussion of Si effects should be strictly based on the irradiation condition selected.

At the relatively high irradiation temperature of 400°C, the Frank loops observed should be mainly interstitial in nature [21, 22], and their depth distribution is an indicator of interstitial point defect distribution. The Si effects here should be attributed to Si’s effects on interstitials and vacancies.

Si is an undersized, fast-diffusing element in austenite stainless steel. It interacts with both interstitials and vacancies during irradiation [23]. Currently mainly two mechanisms for Si diffusion in stainless steel are proposed: the vacancy exchange mechanism and the interstitial dragging mechanism. They are discussed respectively in the following part.

1) Si-interstitial interaction

As an undersized element in stainless steel, Si will trap interstitials and form Si-interstitial complexes. Such trapping and binding mechanism is believed to refine the interstitial loop structure with smaller loop size and higher loop density [24-26]. This conflicts with our results that Frank loop number density is also suppressed by the addition of Si.

If the Si addition can increase the number of interstitials trapped by the surface sink, then the phenomena could be explained. If so, the surface sink will trap more interstitials in high Si sample; cause the interstitial density to be lower than that of the other two samples, especially in the near surface region; and finally result in a lower Frank loop density and average size. However, the effects of Si on increasing interstitial diffusivity or enhancing the surface trapping of interstitials were NOT found in previous literatures, thus this is actually a questionable assumption. It needs further theoretical confirmation.

2) Si-vacancy interaction.

In heavy ion irradiation, interstitials is believed to concentrate at deeper regions than vacancies: first, due to forward scattering effect, the peak of interstitial distribution will be a little deeper than that of vacancies [27]; secondly, surface sputtering caused by irradiation beam can increase vacancy density in near-surface region [28]; finally, when point defect diffusion is considered, sample surface will be a preferential sink for interstitials, as interstitials diffuse orders faster than vacancies [9, 29].

In this study, the number density of interstitial-type Frank loops reaches maximum at around the peak dpa depth. Therefore, the peak of vacancy distribution should be somewhere between sample top surface and the peak dpa depth. Previous observations of void distribution also indicate that vacancies concentrate in regions shallower than the peak dpa depth [11, 27, 30].

The effective vacancy diffusivity could be written as the summation of all the elements diffusing through the vacancy mechanism [31]:

$$D_v^{eff} = D_{v,Fe}C_{Fe} + D_{v,Ni}C_{Ni} + D_{v,Cr}C_{Cr} + D_{v,Si}C_{Si} + \ldots\ldots$$

Where $D_{v,X}$ is the diffusivity of element X via vacancy exchange mechanism. C_X is the atomic fraction of element X. Si can diffuse fast through the vacancy mechanism, thus even when small amount of Si is added, it evidently promotes effective vacancy diffusivity [18, 31-34]. As the slow diffusion rate of vacancies is usually the bottle neck of recombination, the recombination between vacancies and interstitials is also enhanced with Si addition. Therefore, in the shallower region where vacancies concentrate, the 0.95% addition of Si enhances recombination and thus substantially suppresses interstitial-type Frank loops in both number density and average size. At other depths, the addition of Si also suppresses Frank loop density and size in the same way, but the suppression will not be so pronounced due to the lower density of vacancies.

3.4 Perfect loop formation

By raising irradiation temperature and dose, perfect loops may also form besides Frank loops. How perfect loop formation, together with Frank loops formation, is influenced by Si content and irradiation temperature is discussed below.

3.4.1 Perfect loop formation affected by Si at 450°C

When samples are irradiated at 450°C to 5dpa, Ni-Si precipitates and perfect loops may be formed. The precipitate formation at this condition will be checked in the next chapter, and the loop formation is first examined here by TEM.

Fig. 3-8 shows the bright field images at damage peak depth of the three irradiated samples. The ***g*** vector selected is <200>, and the images are captured under dynamic two beam condition. Very dense dislocation loops are observed in these images. The density of black dots is very low, and no voids are found in all the three compositions of alloys. Since the irradiation condition here is high temperature of 450°C and high dose of 5dpa, the unfaulting of Frank loops may become evident. Special care should be taken when treating these dislocation loops, because they could be either Frank loops or perfect loops.

An easy method to differentiate Frank loops and perfect loops is to apply the relrod technique, as relrod images only show the stacking faults of Frank loops. Also, the very dense Frank loops in Fig. 3-8 can be better imaged through relrod technique to avoid the difficulty in distinguishing overlapping loops. In this way, at least the Frank loops here can be counted and measured with high reliability and small error.

The relrod images of the three irradiated model alloys at the damage peak depth are shown in Fig. 3-9. At this high temperature, the size of Frank loops turns out to be large in all the three samples. The number density of Frank loops in the high Si sample looks larger than that in the other two samples.

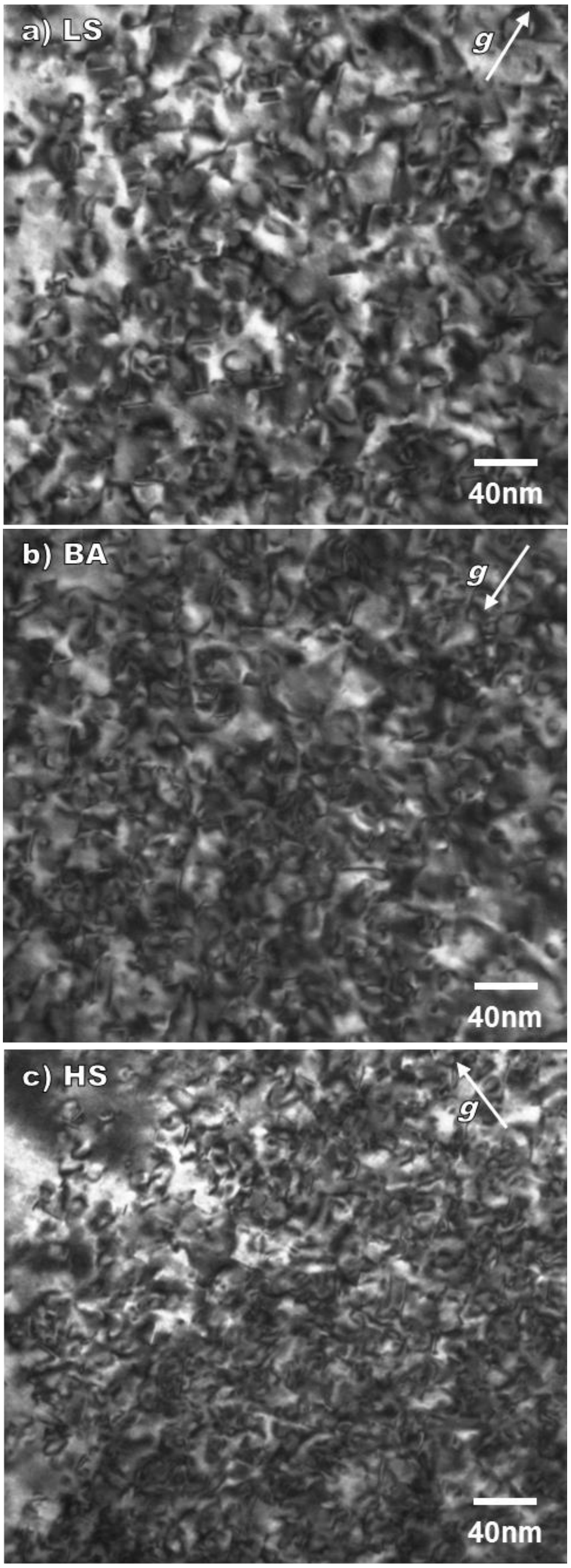

Fig. 3-8 TEM dynamic bright field images (***g***=<200>) at the damage peak depth of a)low Si, b)base Si, c)high samples irradiated at 450°C to 5dpa

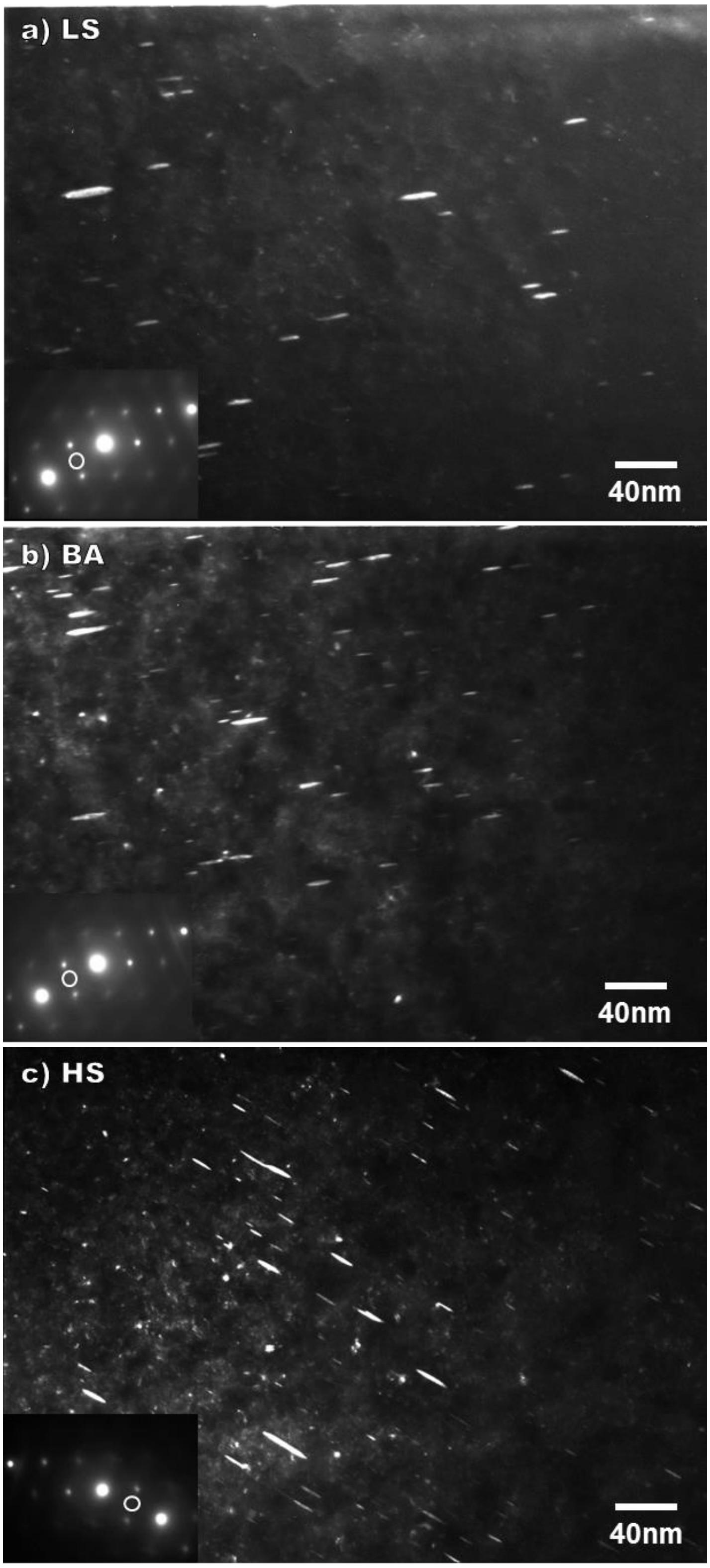

Fig. 3-9 TEM relrod images at the damage peak depth of a)low Si, b)base Si, c)high Si samples irradiated at 450°C to 5dpa. The white circle in the diffraction pattern marks the position of objective aperture.

Quantitative loop measurement is performed at different depths to extract the depth distribution of Frank loops. At each depth, the counting results in 3~4 images are averaged, and the final results of number density and average loop size are shown in Fig. 3-10. The peak dpa depth is calculated by SRIM code and is marked in the figure for reference. The error bars in Frank loop number density is also calculated by the square root of the counting number.

In 400°C and 3dpa irradiation, the addition of Si suppresses both Frank loop number density and average size, as previously described in Section 3.3. However, here in 450°C and 5dpa irradiation, Si effects seem to be different. As shown in Fig. 3-10(a), the addition of Si does not much change the Frank loop number density in the region of 200~600nm depth. In deeper regions of 600~1000nm depth, higher the Si content, larger the Frank loop number density, which seems to be exactly the opposite from the trend in 400°C and 3dpa irradiation. In region beyond 1200nm depth, Frank loops almost disappear and their number density is very low.

In Fig. 3-10(b), the average size of Frank loops is less affected by depth compared to its number density, and is slightly suppressed by Si addition. These trends are similar to that observed in 400°C and 3dpa irradiation. The Frank loop average size is large in this relatively high temperature and high dose irradiation. Besides, the data scattering in average size distribution cannot be ignored, thus it could be quite difficult to draw further conclusions.

The number density of perfect loops is deduced by combining the information in relrod images and weak beam dark field images. As we know, in relrod images 100% Frank loops and 0% perfect loops will be observed; in weak beam dark field images under ***g*** vector of <200>, 100% Frank loops and 2/3 perfect loops will be observed. When dislocation loops are counted at the same depth in both two kinds of images, then the total dislocation loop number density which contains 100% Frank loops and 100% perfect loops can be calculated. The observation and calculation results at the damage peak depth are listed in Table 3-3. Note that although the measurement of Frank loops in relrod images is of high accuracy, the error of counting in dark field images could be quite large because of the dense and overlapping loops.

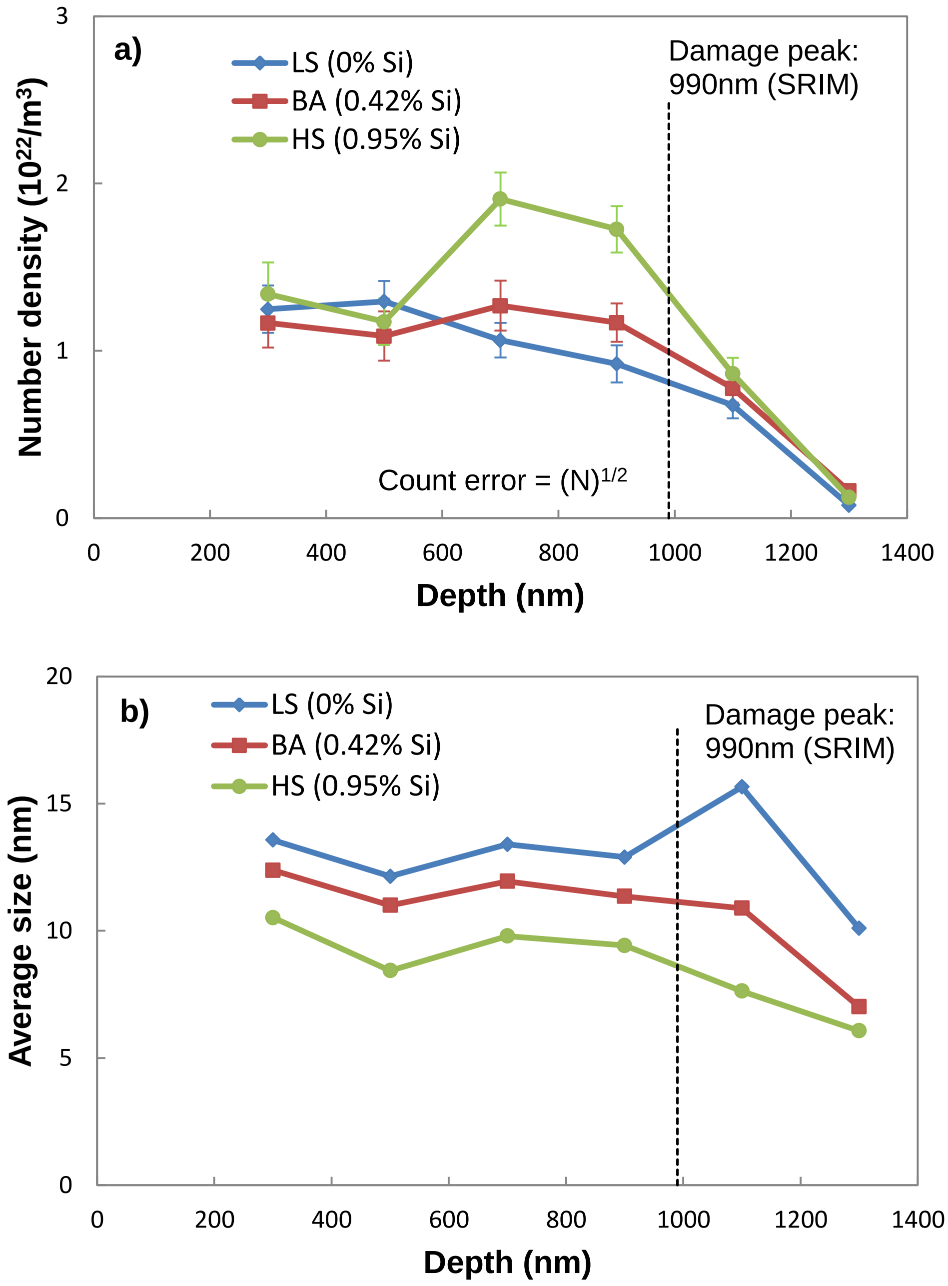

Fig. 3-10 Depth distributions of Frank loop a) number density and b) average size in 450°C and 5dpa irradiated samples. Measurement is performed in relrod images.

Table 3-3 Loop number density and average size in damage peak region (800~1000nm depth) by relrod and weak beam dark field (***g***=<200>) techniques. Samples are irradiated to 5pa at 450°C.

	Observation Method	Observed loop density ($\times 10^{21}$ m^{-3})	Observed loop average size (nm)	Calculated total loop density, faulted + unfaulted ($\times 10^{21}$ m^{-3})
Low Si (0%Si)	Relrod	9.2	12.9	23
	g=<200> dark field	18	13.5	
Base Si (0.42wt.%Si)	Relrod	12	11.4	25
	g=<200> dark field	21	14.7	
High Si (0.95wt.%Si)	Relrod	17	11.3	25
	g=<200> dark field	23	12.2	

The calculated total loop number density is on the same level for the three compositions of model alloys. The dislocation loop density seems to saturate at this high dpa due to the limited space for microstructure evolution. The addition of Si leads to a higher number density of Frank loops, but also results in a lower density of perfect loops. And for low Si sample, the number density of Frank loops at the dpa peak region is even smaller than that in regions with lower dpa. This indicates that the major process of dislocation loop development at this stage is the conversion from Frank loops to perfect loops instead of the formation of more Frank loops, and Si addition here is shown to hinder the unfaulting process of Frank loops. Similar results have been discussed in the previous section that Si addition suppresses the formation process of Frank loops in 400°C and 3dpa irradiation. As a conclusion, the addition of Si tends to regard the microstructural development of dislocation loops at these two irradiation conditions, or Ni-Si precipitate formation, which has been confirmed in this study by APT in Section 4.2, may help to stabilize Frank loops against unfaulting at 450°C [18].

The loop average size observed under dark field images is larger than that observed under relrod. This is because perfect loops are larger than Frank loops in average. The effect of Si content on average loop size seems to be not so clear, may well due to the relatively larger error when measuring average size. Generally speaking, the addition of Si tends to reduce the loop size a little bit.

3.4.2 Perfect loop formation affected by Si by temperature

The effects of irradiation temperature are also discussed. As the first step, only the microstructure of low Si samples (~0% Si) are analyzed in this work, so that the Ni-Si precipitates need not to be considered. Low Si samples are irradiated at 350°C, 400°C and 450°C respectively, and the irradiation dose is fixed at 5dpa.

The cross-section TEM specimens are also prepared by FIB, and are checked under ***g*** vector of <200> and <111>. Fig.3-11 shows the TEM bright field images at the damage peak depth of low Si sample irradiated at 350°C~450°C to 5dpa. The images are taken under ***g***=<200> at dynamic two beam condition. The dislocation loops are so dense that it is difficult to tell the differences between the three samples. No voids are found. The major radiation defect is dislocation loops, and black dots are in low density.

The relrod technique is also applied to distinguish Frank loops. In dark field images with ***g***=<200>, all the Frank loops are visible, and only 2/3 perfect loops could be seen; in relrod images, all the Frank loops are visible, and none of the perfect loops could be seen. By counting the visible loops under dark field images and compare with the Frank loop number density observed by relrod technique, the number density of perfect loops could be obtained. The counting results in the damage peak region are listed in Table 3-4.

For irradiation at 350°C, no unfaulting of Frank loops is observed, as the observed loop number density in dark field images (***g***=<200>) is almost the same with that observed by relrod technique. When irradiation temperature is raised to 400°C, perfect loops exist but are in low number density, as the observed loop number density in dark field images is slightly higher than that in relrod images. The temperature of 400°C seems to be the boundary of perfect loop formation. Since the dose at this depth is ~7dpa, this combination of temperature and dose seems to be a little smaller than the boundary condition in neutron irradiation summarized by Maziasz and Mchargue [35]. When irradiation temperature is further increased to 450°C, the number density of Frank loops dramatically decreases, while the total loop number density maintains the same.

This indicates the saturation of loop development at this high dose. The major difference caused by higher temperature is that more Frank loops become perfect loops by unfaulting.

The loop average size is also similar among the three irradiation temperature. The average size at 450°C is a little bit higher than the other two temperatures, which is a reasonable trend.

With relrod technique, the depth distribution of Frank loops is obtained by the same method described in the previous section. The measuring results are shown in Fig. 3-12. As discussed above, since the number density of Frank loops in the dpa peak region is smaller than that in lower dpa regions at 450°C, the decrease in Frank loop density should be caused by unfaulting. The Frank loop density of irradiation at 350°C and 400°C are similar except for the damage peak region. The Frank loops density is much higher for 350°C irradiation in damage peak region. However, difference in average size of Frank loops is very small.

Table 3-4 Loop number density and average size in the damage peak region (800~1000nm depth) by relrod and weak beam dark field (***g***=<200>) techniques. Samples are low Si (~0%) model alloys irradiated to 5dpa

Irradiation temperature °C	Observation Method	Observed loop density ($\times 10^{21}$ m^{-3})	Observed loop average size (nm)	Calculated total loop density, faulted + unfaulted ($\times 10^{21}$ m^{-3})
350	Relrod	21	11.5	~21
	g=<200> dark field	20	11.8	
400	Relrod	19	11.7	24
	g=<200> dark field	22	11.7	
450	Relrod	9.2	12.9	23
	g=<200> dark field	18	13.5	

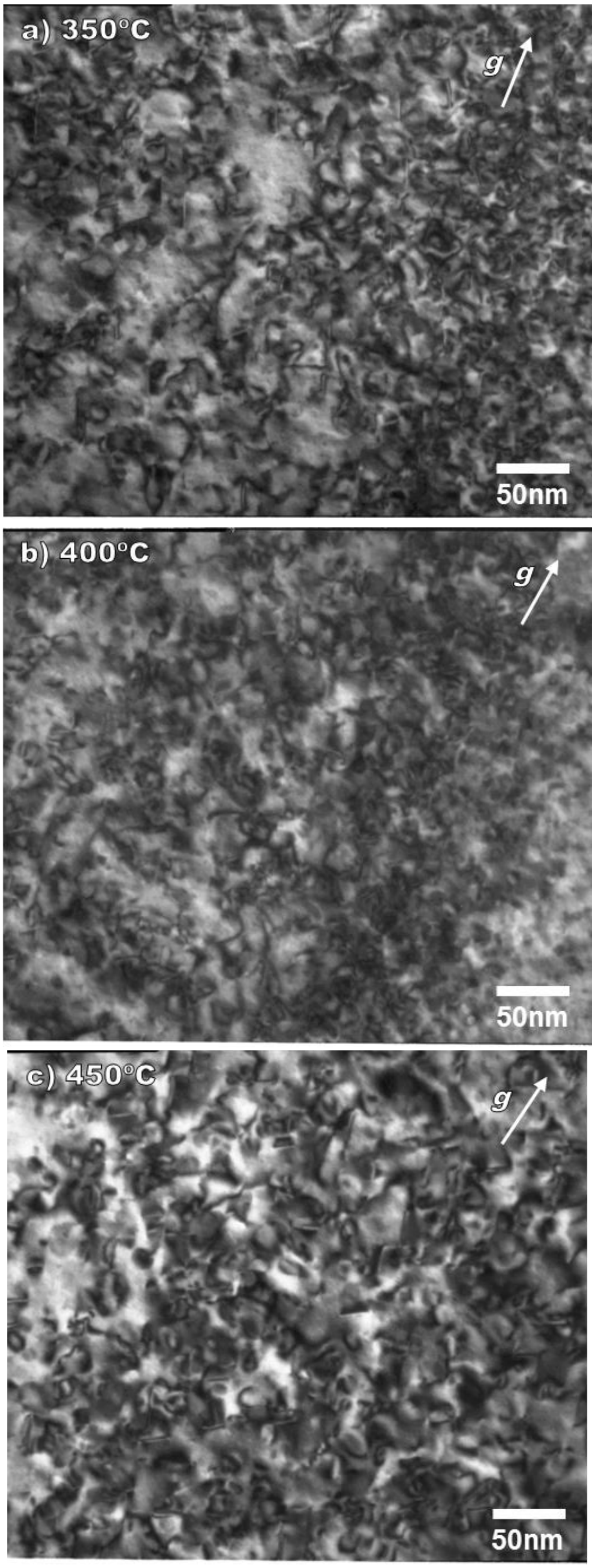

Fig. 3-11 TEM dynamic bright field images at the damage peak depth of low Si sample irradiated at a) 350°C, b) 400°C, c) 450°C to 5dpa (***g***=<200>).

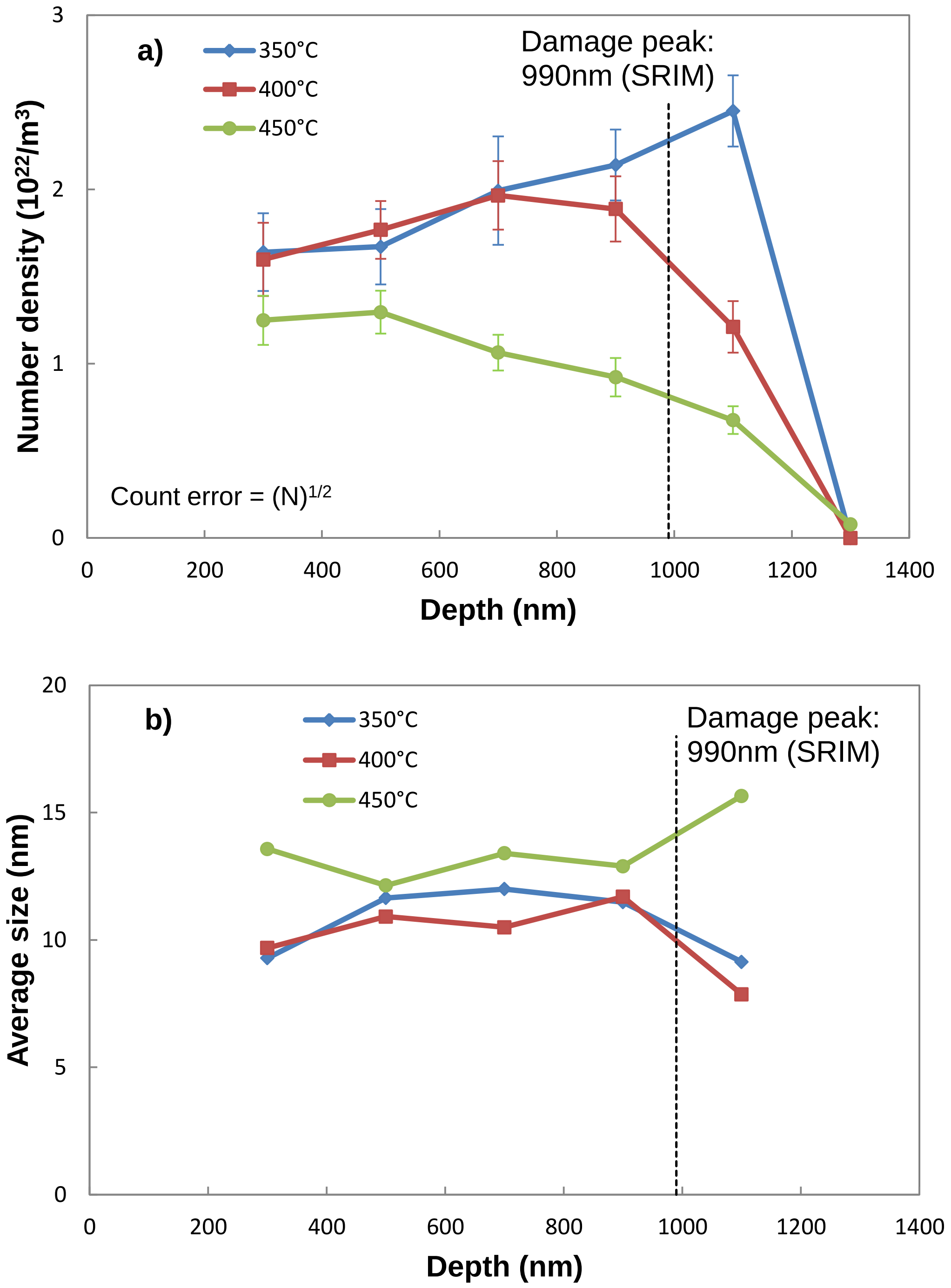

Fig. 3-12 Depth distributions of Frank loop a) number density and b) average size in low Si samples which are irradiated to 5dpa. Measurement is performed in relrod images.

With the total loop density around 2×10^{22} m^{-3}, the average distances between dislocation loops could be estimated to be ~35nm for all the three irradiation temperatures [14]. However the point defects in higher temperature will have longer diffusion range, and will be easier to trigger the self-unfaulting of Frank loops by trapping or emitting point defects. The saturation dose for dislocation loop development is supposed to be 1~5dpa in LWR conditions [36] and 10dpa for temperature range of 300~700 [37]. Bruemmer et al. have pointed out that since the formation and growth of cavities preferentially absorb vacancies, the development of interstitial dislocation loops would quickly saturate in the conditions without cavity formation [38]. This could explain the saturation condition of dislocation loops in here.

3.5 Summary

In this chapter, the formation of black dots and dislocation loops are investigated, respectively. The depth distribution of Frank loops is obtained by observing cross-section TEM samples with relrod technique. The existence of perfect loops is verified by comparing the loop density counted under dark field images and relrod images. The effects of Si content and irradiation temperature on defect formation are discussed. Here are the major conclusions:

1) Black dots are the major radiation defects when samples are irradiated at 290ºC to ~0.8dpa. Observed black dots are mainly Frank loops in nature. The number density and the average size of black dots are not much influenced by Si addition.
2) At higher irradiation temperature of 400ºC (3dpa), Frank loops are the major radiation defects. Frank loops are distinctively suppressed in both density and size by Si addition, especially in the near-surface region. This could be explained by Si's role in enhancing the effective diffusivity of vacancies and thus promoting recombination. It may also be explained if the Si addition can promote the surface trapping effects for interstitials, but this assumption lacks theoretical support currently.
3) The unfaulting of Frank loops is most evident when irradiation temperature is high and Si content is low. Si addition retards the unfaulting of Frank loops, possibly via suppressing Frank loop size or stabilizing Frank loops by precipitation.

References in Chapter 3

[1] M. L. Jenkins. Characterization of Radiation-Damage Microstructures by Tem. J Nucl Mater, 1994, 216: 124-156.

[2] D. J. Edwards, E. P. Simonen, S. M. Bruemmer. Evolution of fine-scale defects in stainless steels neutron-irradiated at 275 degrees C. J Nucl Mater, 2003, 317 (1): 13-31.

[3] P. J. Barton, B. L. Eyre, D. A. Stow. Structure of Fast-Reactor Irradiated Solution-Treated Aisi Type-316 Steel. J Nucl Mater, 1977, 67 (1-2): 181-197.

[4] C. Pokor, Y. Brechet, P. Dubuisson, et al. Irradiation damage in 304 and 316 stainless steels: experimental investigation and modeling. Part I: Evolution of the microstructure. J Nucl Mater, 2004, 326 (1): 19-29.

[5] Z. C. Li, H. Abe, N. Sekimura. Analysis of defects formation and mobility during ion irradiation by coherent precipitates. Mater Trans, 2006, 47 (2): 259-262.

[6] N. Sekimura, M. Taguchi, S. Ishino. Inhomogeneous Microstructural Evolution in Ion-Irradiated Austenitic Steel. J Nucl Mater, 1988, 155: 828-832.

[7] F. A. Garner, M. B. Toloczko. Persistence of microstructural evolution in irradiated metals and its consequences at high radiation exposure. Radiat Eff Defect S, 1999, 148 (1-4): 479-514.

[8] K. Shiraishi, K. Fukai, E. Yagi. Damage Profiles in a Stainless-Steel Irradiated with Ar and N Ions. J Nucl Mater, 1991, 179: 550-553.

[9] A. Etienne, M. Hernandez-Mayoral, C. Genevois, et al. Dislocation loop evolution under ion irradiation in austenitic stainless steels. J Nucl Mater, 2010, 400 (1): 56-63.

[10] J. Gan, G. S. Was. Microstructure evolution in austenitic Fe-Cr-Ni alloys irradiated with protons: comparison with neutron-irradiated microstructures. J Nucl Mater, 2001, 297 (2): 161-175.

[11] S. Ishino, N. Sekimura. Role of Charged-Particle Irradiations in the Study of Radiation-Damage Correlation. J Nucl Mater, 1990, 174 (2-3): 158-167.

[12] N. Sekimura, H. Kawanishi, M. Nodaka, et al. The Effect of Helium on the Microstructural Evolution in Pca as Studied by Dual Beam Irradiation. J Nucl Mater, 1984, 122 (1-3): 322-326.

[13] J. T. Busby, M. M. Sowa, G. S. Was, et al. Post-irradiation annealing of small defect clusters. Philos Mag, 2005, 85 (4-7): 609-617.

[14] K. Fukuya, K. Fujii, H. Nishioka, et al. Evolution of microstructure and microchemistry in cold-worked 316 stainless steels under PWR irradiation. J Nucl Sci Technol, 2006, 43 (2): 159-173.

[15] M. Victoria, N. Baluc, C. Bailat, et al. The microstructure and associated tensile properties of irradiated fcc and bcc metals. J Nucl Mater, 2000, 276: 114-122.

[16] Y. Miwa, T. Tsukada, H. Tsuji, et al. Microstructures of type 316 model alloys neutron-irradiated at 513 K to 1 dpa. J Nucl Mater, 1999, 271: 316-320.

[17] Y. Miwa, T. Tsukada, S. Jitsukawa, et al. Effect of minor elements on irradiation assisted stress corrosion cracking of model austenitic stainless steels. J Nucl Mater, 1996, 233: 1393-1396.

[18] N. Sekimura, F. A. Garner, J. W. Newkirk. Silicons Role in Determining Swelling in Neutron-Irradiated Fe-Ni-Cr-Si Alloys. J Nucl Mater, 1992, 191: 1244-1247.

[19] K. Fukuya, S. Nakahigashi, S. Ozaki, et al. Effects of Phosphorus, Silicon and

Sulfur on Microstructural Evolution in Austenitic Stainless-Steels during Electron-Irradiation. J Nucl Mater, 1991, 179: 1057-1060.

[20] N. Shigenaka, T. Hashimoto, M. Fuse. Effects of Alloying Elements (Mo, Si) in an Austenitic Stainless-Steel on Dislocation Loop Nucleation under Ion Irradiation. J Nucl Mater, 1993, 207: 46-52.

[21] K. V. Tsay, O. P. Maksimkin, L. G. Turubarova, et al. Microstructural defect evolution in neutron - Irradiated 12Cr18Ni9Ti stainless steel during subsequent isochronous annealing. J Nucl Mater, 2013, 439 (1-3): 148-158.

[22] R. D. Carter, D. L. Damcott, M. Atzmon, et al. Effects of Proton Irradiation on the Microstructure and Microchemistry of Type-304l Stainless-Steel. J Nucl Mater, 1993, 205: 361-373.

[23] E. A. Kenik, J. T. Busby. Radiation-induced degradation of stainless steel light water reactor internals. Mat Sci Eng R, 2012, 73 (7-8): 67-83.

[24] S. I. Porollo, S. V. Shulepin, Y. V. Konobeev, et al. Influence of silicon on swelling and microstructure in Russian austenitic stainless steel EI-847 irradiated to high neutron doses. J Nucl Mater, 2008, 378 (1): 17-24.

[25] H. Watanabe, A. Aoki, T. Muroga, et al. Effect of Combined Addition of Phosphorus and Titanium on Microstructural Evolution in Fe-Cr-Ni Alloys. J Nucl Mater, 1991, 179: 529-533.

[26] R. S. Averback, P. Ehrhart. Diffuse-X-Ray Scattering Studies of Defect Reactions in Electron-Irradiated Dilute Nickel-Alloys .1. Ni-Si. J Phys F Met Phys, 1984, 14 (6): 1347-1363.

[27] L. Shao, C. C. Wei, J. Gigax, et al. Effect of defect imbalance on void swelling distributions produced in pure iron irradiated with 3.5 MeV self-ions. J Nucl Mater, 2014, 453 (1-3): 176-181.

[28] J. C. Kim, D. G. Cahill, R. S. Averback. Surface defects created by 20 keV Xe ion irradiation of Ge(111). Surf Sci, 2005, 574 (2-3): 175-180.

[29] R. E. Stoller. Modeling Dislocation Evolution in Irradiated Alloys. Metall Trans A, 1990, 21 (7): 1829-1837.

[30] T. Aruga, Y. Katano, K. Shiraishi. Double Peak of Voidage Depth Profile in Carbon or Nitrogen Ion Irradiated 316-Stainless Steel. J Nucl Mater, 1984, 122 (1-3): 191-195.

[31] B. Esmailzadeh, A. Kumar, F. A. Garner. The Influence of Silicon on Void Nucleation in Irradiated Alloys. J Nucl Mater, 1985, 133 (Aug): 590-593.

[32] Z. Jiao, J. T. Busby, G. S. Was. Deformation microstructure of proton-irradiated stainless steels. J Nucl Mater, 2007, 361 (2-3): 218-227.

[33] F. A. Garner, W. G. Wolfer. The Effect of Solute Additions on Void Nucleation. J Nucl Mater, 1981, 102 (1-2): 143-150.

[34] F. A. Garner, W. G. Wolfer. Factors Which Determine the Swelling Behavior of Austenitic Stainless-Steels. J Nucl Mater, 1984, 122 (1-3): 201-206.

[35] P. J. Maziasz, C. J. Mchargue. Microstructural Evolution in Annealed Austenitic Steels during Neutron-Irradiation. Int Mater Rev, 1987, 32 (4): 190-219.

[36] K. Fukuya. Current understanding of radiation-induced degradation in light water reactor structural materials. J Nucl Sci Technol, 2013, 50 (3): 213-254.

[37] S. J. Zinkle, P. J. Maziasz, R. E. Stoller. Dose Dependence of the Microstructural Evolution in Neutron-Irradiated Austenitic Stainless-Steel. J Nucl Mater, 1993, 206 (2-3): 266-286.

[38] S. M. Bruemmer, E. P. Simonen, P. M. Scott, et al. Radiation-induced material changes and susceptibility to intergranular failure of light-water-reactor core internals. J Nucl Mater, 1999, 274 (3): 299-314.

4. Precipitate formation and its relationship with loops

4.1 APT Methodology

The previous chapter shows the TEM observation results of all the irradiation conditions selected in this study. In this chapter, some of these conditions are selected for further analysis by APT. The 450°C and 5dpa condition is selected here, because Ni-Si precipitates are most likely to be formed at this high temperature. 290°C and ~0.8dpa condition is also selected for comparison, because Ni-Si precipitates are not likely to form and there may be sign of precipitate precursors in this condition.

The atom probe tomography (APT) machine used in this study is CAMECA Local Electrode Atom Probe (LEAP) 3000XSi. The raw APT data is analyzed by IVAS 3.6.6 software provided by CAMECA. The samples for APT are also prepared by focused ion beam (FIB) technique.

First, a tungsten layer is deposed onto the irradiated sample surface to reduce FIB damage to the APT sample. A needle sample is extracted from the irradiated sample by FIB, covering the range from sample top surface to around 200~300nm depth. The observation depth is quite shallow here, but previous work has found that the existence of surface sink does not suppress Ni-Si precipitation [1]. The needle sample is then welded onto the tip of a pre-prepared needle-shape support.

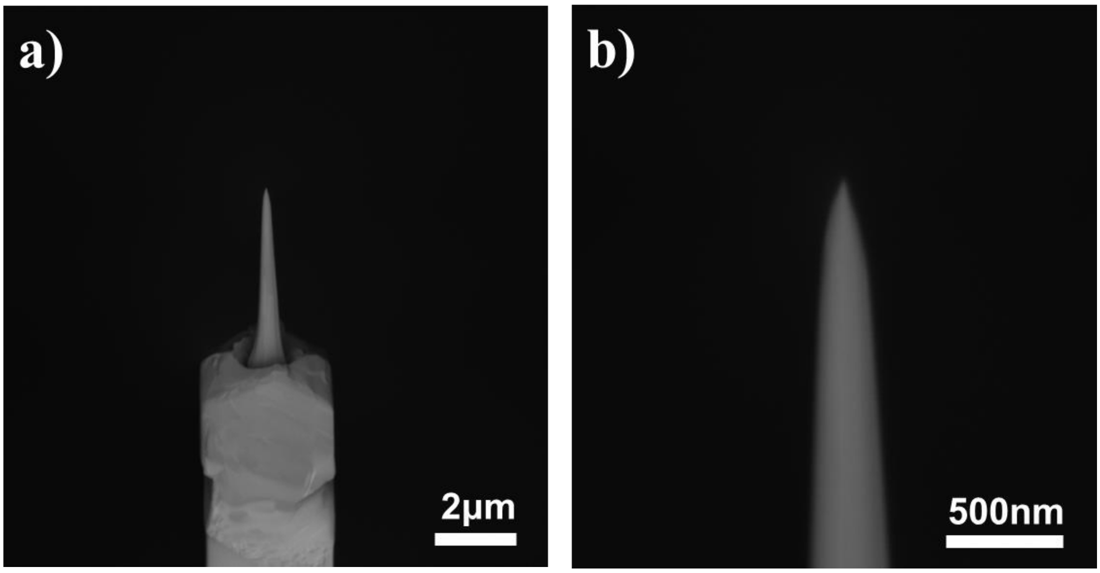

Fig. 4-1 SEM images of typical needle sample prepared for APT under SEM, a) overview, b) tip view

Unlike TEM samples, the observation focus of APT sample is element distribution instead of dislocation defects. Therefore a very thin layer of extra FIB irradiation damage is acceptable in the case of APT samples. Thus as the final step, 10kV and 5kV Ga ions are used in sequence at small angle of incidence to lessen the extra FIB damage. The SEM images of a typical needle sample prepared for APT observation is shown in Fig. 4-1. Only the needle tip of around 200~300nm length could be tested in APT.

The needle samples are then used in APT analysis. In APT, by applying a series of high voltage pulses, the surface atoms of the needle sample tip are field evaporated, and then fly to the detector under a controlled magnetic field, as shown in Fig. 4-2. Atom species and position can be deduced by time-of-flight and their arriving coordinates at the detector. Therefore, atom map of near-atomic resolution can be reconstructed in this way. The APT test is performed at temperature as low as 40K to minimize the interference of atom thermal vibration.

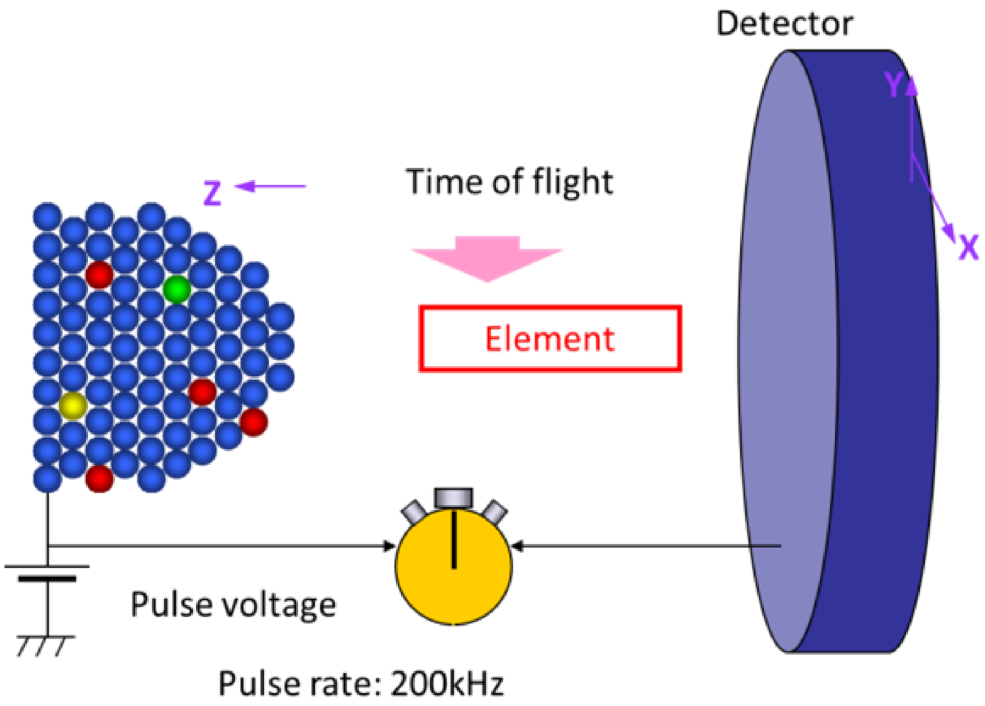

Fig. 4-2 A schematic of APT technique

Before comparing TEM and APT results, two facts need to be kept in mind:

- For the same irradiated model alloy, the tiny TEM and APT samples are picked up by FIB at different positions of the same irradiated bulk sample. TEM and APT samples are both picked up from grains that are close to {111} orientation; but they are not picked up from the same grain.
- The TEM observation can extend to regions much deeper than the damage peak depth of irradiation (>2μm), while APT observation can only extend to 300nm depth in maximum from the bulk sample surface.

4.2 Ni-Si precipitates formed at 450°C

4.2.1 Atom map results

High temperature of 450°C and high irradiation dose of 5dpa are selected to try to produce γ' precipitates in stainless steel. All the three compositions of model alloys are irradiated here. Tiny needle samples are picked up by FIB from the irradiated samples, and are then tested by APT to obtain atom maps.

First of all, the data reliability of APT needs to be first confirmed. It is done by comparing the composition of needle samples tested by APT with the bulk composition of the corresponding prepared model alloys. The results are listed in Table 4-1. The model alloy composition is in atom percentage here, which is converted from the weight percentage value previously listed in Table 2-1. It can be seen from Table 4-1 that the composition data drawn from the two methods matches quite well. The difference in Mo may be a little larger than other alloying elements. Since element segregation usually occurs more or less in irradiated stainless steels and the tested size of APT needle samples is actually very small, such difference is acceptable.

Table 4-1 Comparison between needle samples composition tested by APT and model alloys bulk composition

	Model Alloy bulk composition (at.%)			Needle sample composition by APT (at.%)		
	Low Si	Base Si	High Si	Low Si	Base Si	High Si
Fe	67.0	65.8	64.9	68.2	65.1	65.5
Cr	18.2	18.6	18.1	17.0	17.9	17.1
Ni	12.4	12.5	12.8	12.5	13.4	13.2
Si	0	0.83	1.88	0	0.89	1.84
Mn	1.02	0.89	1.00	0.94	0.98	0.95
Mo	1.34	1.37	1.31	1.01	1.32	1.01

The reconstructed atom maps obtained by APT technique are shown in Fig. 4-3. The atom maps of the six major alloying elements, Fe, Cr, Ni, Si, Mn and Mo are listed. Each dot in the atom maps represents an atom detected by APT. The atom map would be too dense to distinguish if all the atoms detected by APT are illustrated. Thus only a fraction of detected atoms is shown here for better visibility.

The formation of precipitates could be clearly seen in the Si atom map. In high Si sample (Fig. 4-3(c)), large precipitates of size roughly around 10nm could be observed in the Si atom map. Enrichment of Ni and depletion of Fe, Cr, Mn and Mo can also be distinguished in the position of these precipitates by the atom maps of other elements, although the image contrast may not be satisfying enough. It can be concluded that some large Ni-Si precipitates have formed in irradiated high Si sample. Whether they are γ' phase precipitates or not remains to be analyzed.

In base Si sample (Fig. 4-3(b)), precipitates can also be seen in the Si atom map, but with smaller size and lower number density compared with these in high Si sample. In the atom maps of other elements, element enrichment or depletion becomes hard to distinguish this time. So is the case in the atom maps of low Si sample (Fig. 4-3(a)).

4.2.2 Isosurface map results

As discussed above, the raw atom maps directly reconstructed from APT testing results cannot meet the demand for detailed precipitate composition analysis in this study. In fact, this is often the problem faced when using APT technique. A raw atom map of APT contains huge quantity of useful information. Although some atoms are lost during APT test, roughly around ~40% of all the atoms in the needle sample tip could be recorded in the atom map. Their species and positions are all recorded. When speaking of one single atom, the error of its position information could be quite large because of the atom thermal vibration during APT test. But statistically speaking, a raw atom map with huge number of atoms detected will contain the trend of element distribution. The difficulty lies in how to interpret or reorganize the large amount of information contained in an atom map to reveal some clear trends that could be interesting.

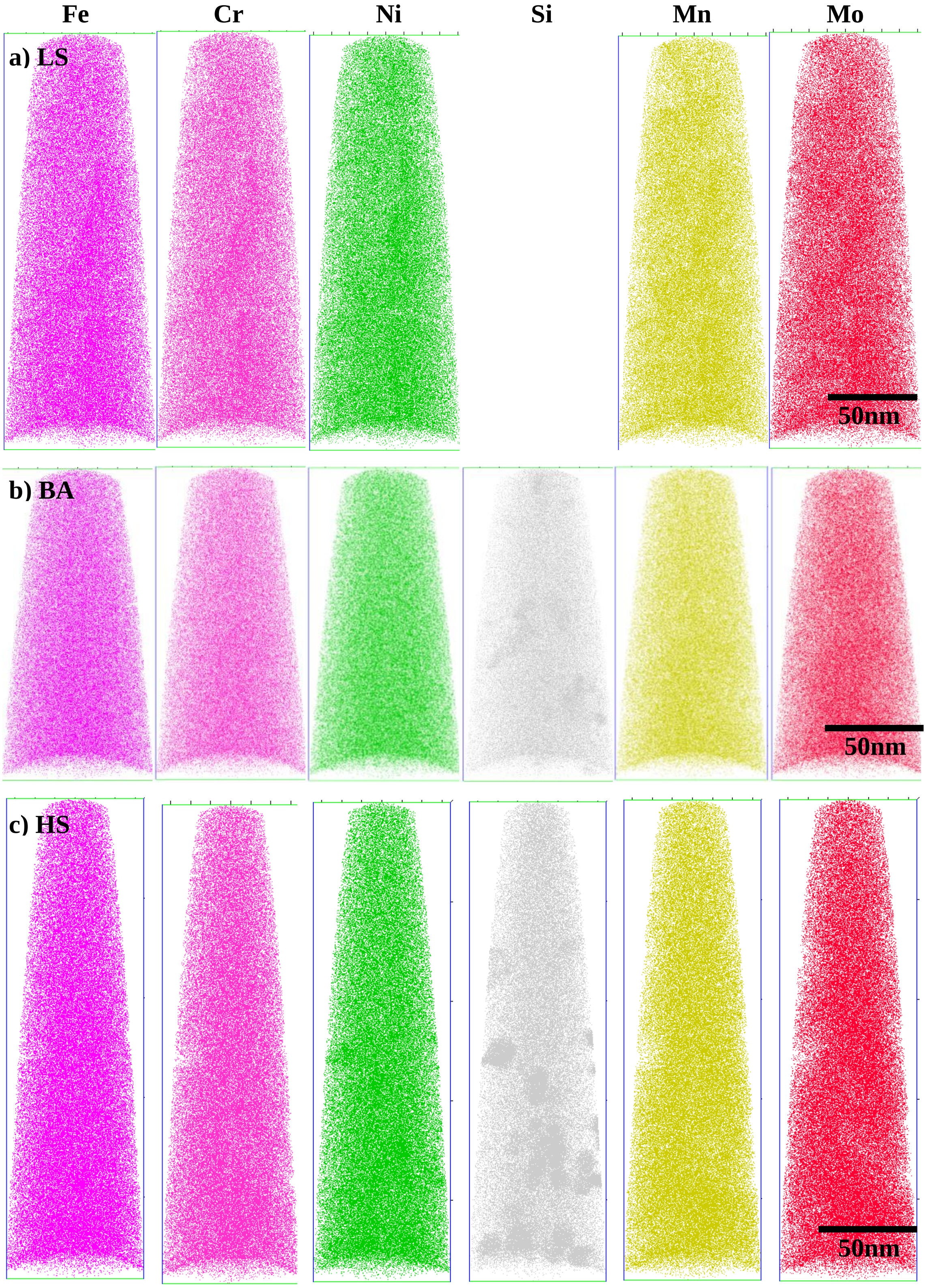

Fig. 4-3 Atom maps of a) low Si, b) base Si, c) high S samples irradiated at 450°C to 5dpa

In this work, several attempts are made to better extract useful information from atom maps. One commonly-used method is to create isosurface maps from atom maps. Isosurfaces are surfaces drawn at any defined threshold value for a specific element. For example, if isosurfaces of 3.5at.% Si is drawn in high Si sample, it means that the surfaces marked in the isosurface map are positions with 3.5at.% Si concentration. Since the bulk Si content of high Si sample is only 1.88at.%, it means that in these marked isosurfaces, Si is enriched. Similarly if Si isosurfaces are drawn at a value smaller than bulk Si content, say 1.0at.%, then the marked isosurfaces are the positions where Si depletes.

The isosurfaces maps of the three model alloys are created from the atom maps in Fig. 4-3, and are shown in Fig. 4-4. The threshold values for isosurfaces are carefully selected to best show the extent of element enrichment or depletion, as listed in Table 4-2. Note that the threshold values selected for the three model alloys are intentionally kept the same for easier comparison. For Ni and Si, threshold value larger than bulk content is chosen, so isosurface map will show the position of element enrichment; For Fe, Cr, Mn and Mo, threshold value smaller than bulk content is chosen, so isosurface map will show the position of element depletion.

Table 4-2 Threshold values selected for isosurface maps of different elements

	Model Alloy bulk composition (at.%)			Isosurface	
	Low Si	Base Si	High Si	Threshold value (at.%)	
Fe	67.0	65.8	64.9	58.0	(deplete)
Cr	18.2	18.6	18.1	11.0	(deplete)
Ni	12.4	12.5	12.8	20.0	(enrich)
Si	0	0.83	1.88	3.50	(enrich)
Mn	1.02	0.89	1	0.30	(deplete)
Mo	1.34	1.37	1.31	0.30	(deplete)

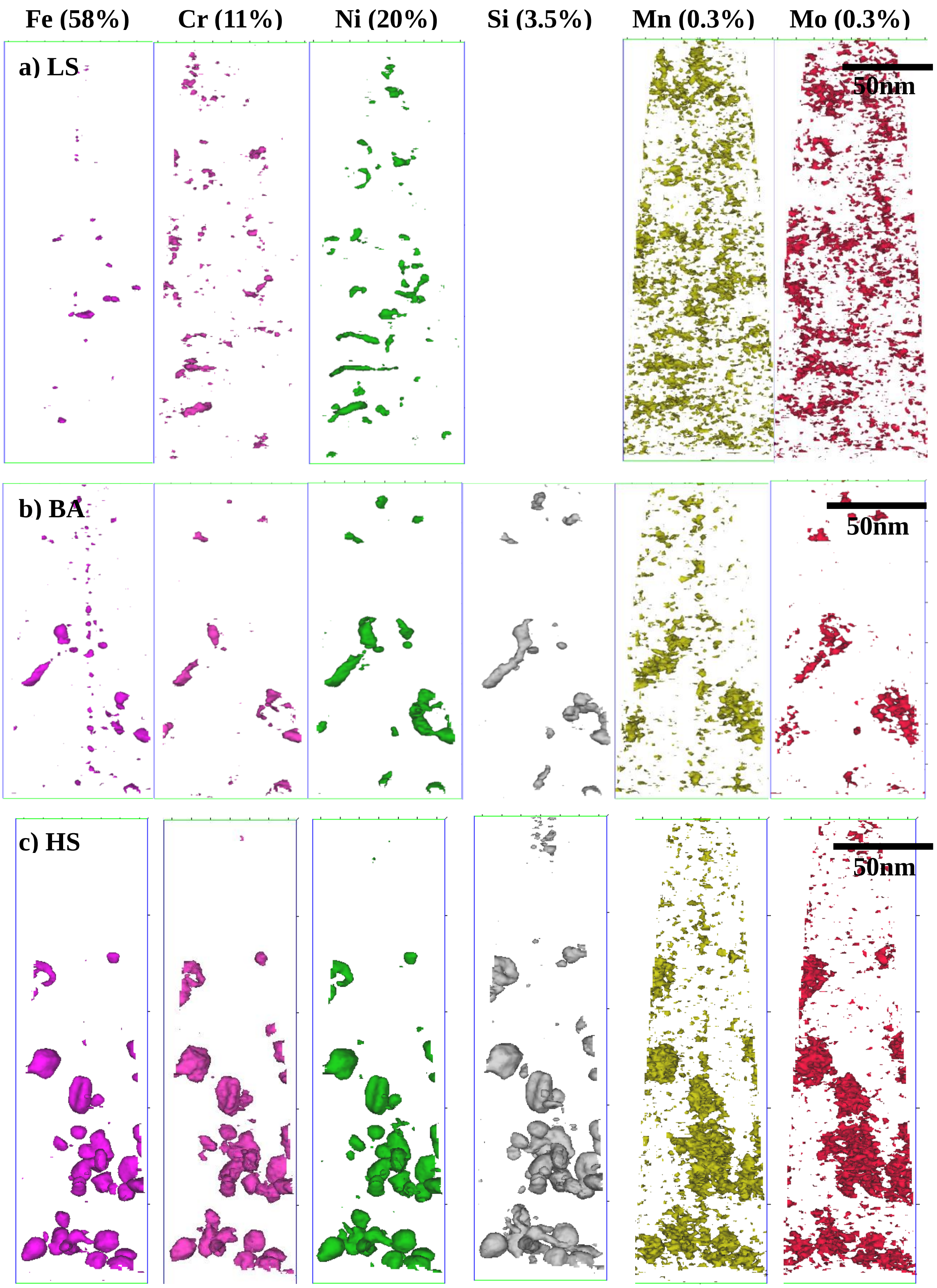

Fig. 4-4 Isosurface maps of a) low Si, b) base Si, c) high Si samples irradiated at 450°C to 5dpa. Isosurface threshold values of each element are marked by at.%.

The isosurface maps in Fig. 4-4 shows similar trends compared to the atom maps in Fig. 4-3, but with much better contrast.

In high Si sample (Fig. 4-4(c)), based on the threshold values selected, the formation of Ni-Si precipitates can be clearly confirmed, with size roughly around 10nm and shape mostly near spherical. In the positions of Ni-Si precipitates, Ni and Si are enriched, and Fe, Cr, Mn and Mo are depleted. The depletion is most pronounced for Mo and Mn, because the isosurface threshold values selected for them are less than 1/3 of their bulk contents. Fe and Cr depletion occurs exactly at the positions where Ni-Si precipitates form, indicating the enrichment and depletion processes are closely related. For Mn and Mo, they also deplete at other places besides Ni-Si precipitation positions. Most precipitates are nearly spherical in shape.

In base Si sample (Fig. 4-4(b)), the formation of Ni-Si precipitates is also confirmed, with smaller size and number density compared to these in high Si sample. The position of Ni, Si enrichment and Fe, Cr depletion also matches well. Mn and Mo also depletes at other positions besides Ni-Si precipitation. In general, enrichment and depletion phenomena observed in base Si sample is similar in trend but smaller in extent when compared to high Si sample.

In low Si sample with contains almost no Si, it is surprising to find out that the enrichment of Ni still occurs at some positions, although the extent is further smaller compared to the other two samples. A large fraction of Ni segregation is observed to be ring-shaped, which indicts they may have formed on dislocation loops.

4.2.3 Quantitative precipitate composition analysis

Although isosurface map has provided some more information about Ni-Si precipitation compared to atom map, it is still difficult to perform quantitative composition analysis only through the isosurface map. This is due to the difficulty in precisely defining the boundary of Ni-Si precipitates. Fig. 4-5 shows the one dimensional line scanning result through a typical Ni-Si precipitate in high Si sample. The line scanning is performed in a Φ3nm cylinder, and the scan width is fixed at 0.5nm. In Fig. 4-5, the center part is the Ni-Si precipitate, and the two sides are the matrix. It can be found that instead of a clear interface between the precipitate and the matrix, there are only gradual composition gradients. Especially for Si, the Si atom concentration keeps changing in the range when distance is 10~15nm, therefore it is difficult to say where the precipitate boundary exactly lies at. The ideal method to solve the boundary definition problem is to build a Ni-Si precipitate database by APT and then manually attempt different kinds of boundary definitions. Currently a precipitate in atom map is usually defined by two major parameters: the distances between atoms and the number of atoms in the precipitate. Values need to be attempted for these two parameters to see if the results of such definition can match the precipitate size, shape and number density visually observed in atom maps.

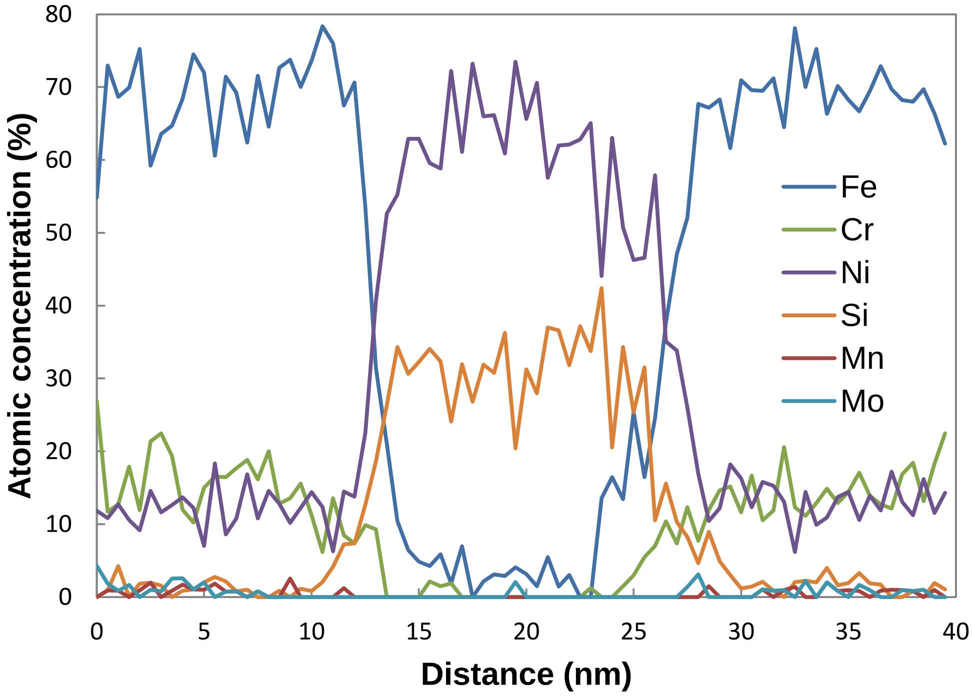

Fig. 4-5 One dimensional line scanning (in Φ3nm cylinder) through a typical Ni-Si precipitate in high Si sample.

In this study, since the number of Ni-Si precipitates observed is limited, it may be misleading to directly draw any kind of precipitate definition. Therefore the composition of precipitate core is used instead of the composition of the whole precipitate, so that its boundary condition could be avoided. As shown in Fig. 4-5, the composition in precipitate core is almost steady. So here, precipitates are randomly selected in each sample, and the composition of each precipitate core, which is defined as a Φ3nm sphere, is averaged to represent the precipitate composition. 3nm is selected here because it is much smaller than the size of Ni-Si precipitates observed, and is large enough to include enough number of detected atoms to minimize error. These precipitate core compositions are plotted in Fig. 4-6. Si concentration is selected as the ***x*** axis because Si concentration is a good indicator of the extent of Ni-Si precipitate growth. Also in this way it will be easier to analyze the Ni/Si atom ratio of precipitates. The concentrations of other elements are plotted against Si concentration.

As shown in Fig. 4-6, both in high Si and base Si sample, two types of Ni-Si precipitates are discovered, as marked in blue and red circles respectively:

- Precipitates in red circle (will-developed Ni-Si precipitates).

The precipitates in the red circle mainly consist of Ni and Si. They have very low Fe or Cr concentration, which is around 5at.% or even less. They are supposed to be the γ’ phase precipitates mentioned the in previous TEM studies in literature. Mo, Mn are fully depleted in these γ’ precipitates, with concentration of ~0%.

- Precipitates in blue circle (developing Ni-Si precipitates).

The Ni-Si precipitates in the blue circle still have quite high concentration of Fe and Cr. For example, the concentration of Fe could be in the range of 25~55at.%. By literature, they could be considered as the γ’ phase precipitates or precursors of γ’ precipitates [2]. Mo, Mn are also fully depleted (~0%) in these precipitates.

As we know, theoretically, standard γ’ phase is Ni_3Si in composition. In a standard γ’ phase precipitate without any impurities or defects, the Ni concentration should be 75at.% and the Si concentration should be 25at.%. However, it is interesting to note that in both high Si and base Si sample, the Ni/Si atom ratio deviates from the standard value 3. In Fig. 4-6, the standard Ni/Si atom ratio is marked as a green dash line, and most of the green dots recorded by APT are actually not on the dash line. Also, the Si concentration far exceeds 25at.% in quite many well-developed precipitates. The Ni-Si precipitates observed in this study seems to have similar stoichiometric ratio to the standard γ’ phase, but in fact the ratio is not strictly followed. This puts doubts on the exact crystal phase of the precipitates observed in this study.

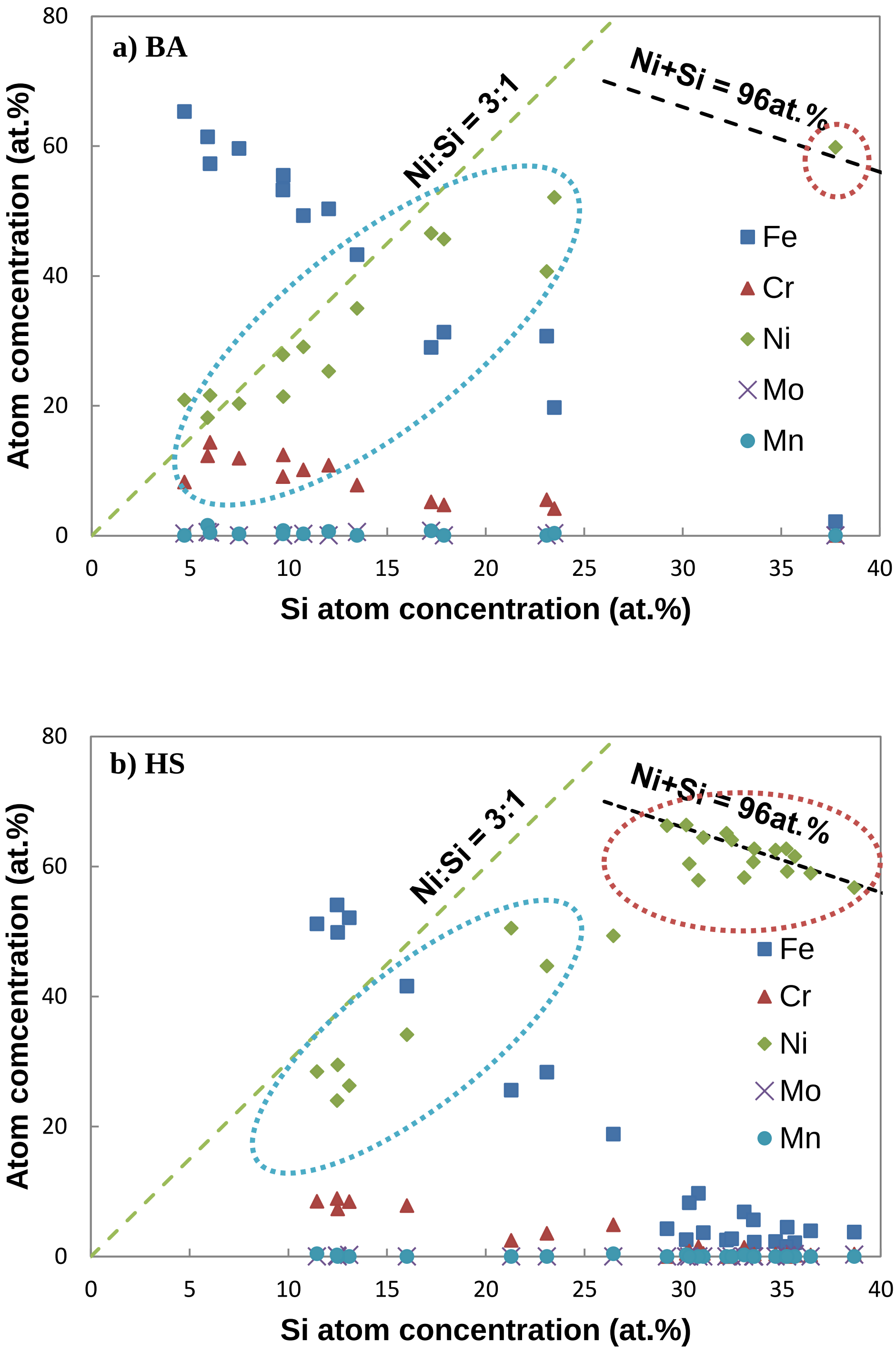

Fig. 4-6 Composition of precipitate core (Φ3nm sphere) in a) base Si, b) high Si samples irradiated at 450°C to 5dpa

By comparing Fig. 4-6(a) and Fig. 4-6(b), the precipitates in base Si and high Si sample have quite different Ni and Si concentrations. In base Si sample (Fig. 4-6(a)), only one precipitate is discovered to have high Ni, Si concentration and low Fe, Cr concentration, and all the other precipitates could be regarded as developing Ni-Si precipitates. But in high Si sample, many precipitates have very high Ni and Si content. Also, base Si sample has precipitates with ~20at.% Ni and ~7at.% Si, while in high Si sample precipitates with so low Ni and Si concentrations are not found. This is easy to understand because Si content of model alloy is a key factor that determines the Ni-Si precipitation. A lower Si content will surely limits both the nucleation and growing process of the precipitates.

However, although the precipitates in base Si sample tend to have less Ni and Si concentration in absolute value than those in high Si sample, the precipitate composition in the two samples seems to follow the same pattern against the Si concentration of the precipitate. Or in other words, if one fixed Si concentration is selected, then the Fe, Cr, Ni, Mn and Mo concentration of precipitates in both base Si and high Si sample are almost the same. This indicates that the formation mechanism of the Ni-Si precipitates in these two samples should be the same, and the major difference is that the precipitates in these two samples are on different growing stages. The smaller Si content in base Si model alloy has limited the growing rate of Ni-Si precipitates or has stopped these precursors from growing into the well-developed Ni-Si precipitates.

In this way, combining the information given in Fig. 4-6(a) and Fig. 4-6(b), a more complete understanding of Ni-Si precipitate growing process can be drawn:

1) At first, Ni-Si precipitates are formed with low Ni and Si concentration. Ni/Si atom ratio is just around the theoretical value 3 at this moment.
2) Then, some of these developing Ni-Si precipitates continue to grow. Ni and Si concentration increases, while the Ni/Si atom ratio decreases, becoming a little less than 3. The concentration of Fe or Cr linearly decreases as a result of precipitate growth.
3) Finally, some developing Ni-Si precipitates grow and become well-developed Ni-Si precipitates. The Fe or Cr concentration is very low at this stage of growth. The Ni/Si atom ratio further decreases and becomes evidently smaller than 3. It seems that the deviation of Ni/Si atom ratio at this growing stage no longer much

influences the remaining low concentration of Fe or Cr. Actually, Ni and Si seems to just replacing each other in composition, following a pattern of Ni+Si = 96at.%, as marked by the black dash line in Fig 4-6. The other alloying elements makes up the remaining 4at.%.

4.2.4 Orientation of Ni-Si precipitates and Ni segregation

Although most of the Ni-Si precipitates observed in Fig. 4-4 are nearly spherical in shape, there are also some ring-shaped Ni-Si precipitates discovered. One typical ring-shaped precipitate observed in base Si sample and one in high Si sample are shown in Fig. 4-7.

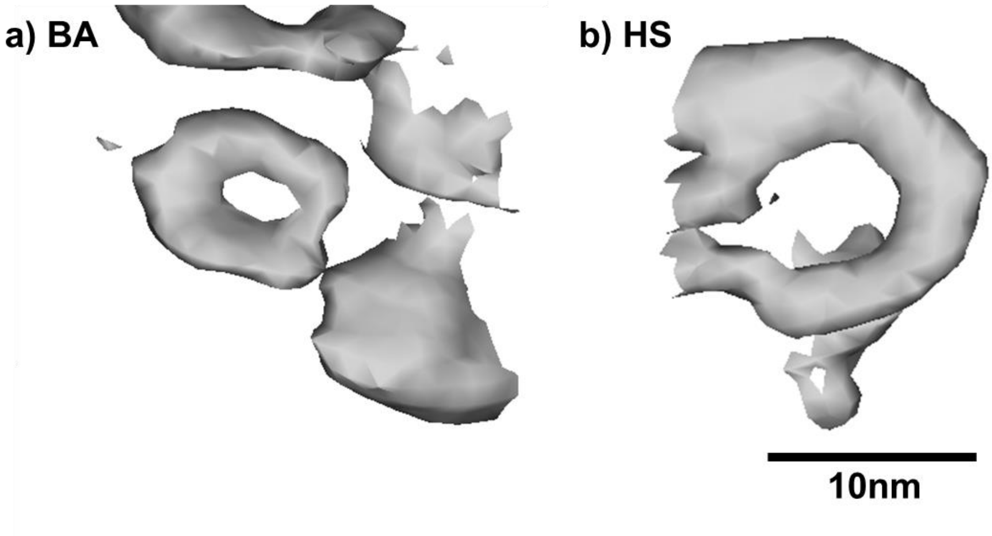

Fig. 4-7 Typical ring-shaped Ni-Si precipitates observed in a) base Si (4at.% isosurface) and b) high Si (7at.% Si isosurface) samples irradiated at 450°C to 5dpa

In the case of low Si sample, a large fraction of Ni segregation is observed to be ring-shaped.

These ring-shaped precipitates or segregation are the focus of this section. There are generally two reasons why the shape of ring is so interesting:

- When considering the minimization of surface energy, second phases in matrix should tend to be spherical in shape.
- The dislocation loops induced by irradiation are also ring-shaped.

Thus, when ring-shaped precipitates or segregation are found, the question whether the existence of dislocation loops is the driving force of such precipitation arises. Unfortunately, APT technique is not sensitive to dislocation loops or stacking faults; TEM is sensitive to dislocation loops, but is insensitive to Ni-Si precipitates. Of course, an ideal solution is to prepare one needle sample, first observe it under TEM, and then analyze it by APT, as Hamaoka et al. did in their outstanding work [3]. But such sample preparation method requires well-experienced experimental technique as well as a bit of luck, and its success rate may be too low to bear.

In this work, another attempt is made to set up the correlation between the loops observed in TEM cross-section specimen and the ring-shaped precipitates observed in APT needle specimen. As we know, in face-centered cubic (FCC) austenite stainless steel, Frank loops lie on the {111} plane, while perfect loops lie on the {110} plane. Since the habit plane of dislocation loops are fixed, the correlation between loops and precipitates could be inferred if the orientation of the Ni-Si precipitates can be deduced in atom map.

Before picking up the APT needle sample from the irradiated bulk sample, the surface of bulk sample is scanned by electron back-scattered diffraction (EBSD) technique. Then a grain very close to {111} orientation is selected, and the APT needle samples are picked up from the center of the selected grain. This means that in each APT needle sample, such as the ones previously shown in Fig. 4-3, its top surface is very close to {111} plane.

For one Ni-Si precipitate or Ni segregation that is ring in shape, although the lattice orientation of its habit planes is unknown, the intersection angle between its habit plane and the top surface {111} plane could be easily measured in atom map, as listed in Table 4-3. Also, the theoretical intersection angles between {111} plane and some other low index planes can be calculated, and the theoretical values are listed in Table 4-4.

By comparing the measured intersection angles in Table 4-3 and the theoretical intersection angles in Table 4-4, it is quite surprising to find out that the angles obtained in these two ways are in good consistency. For segregation No.1 and precipitate No.14, they are almost parallel to the top surface, so it should be on the {111} plane. Segregation No.2~6 and precipitates No.9~13 all have intersection angles of around 70.5° with the top surface, which is the theoretical value of the intersection angle between {111} planes. It is true that the data of intersection angle alone is NOT enough to conclude that these precipitates are on {111} planes. However, such preferential orientation of ten cases cannot simply be attributed to coincidence. Since {111} plane is the habit plane for Frank loops, it is strongly indicated, although not firmly proved, that these precipitates and segregation should have formed on Frank loops. Note that the ring-shaped precipitates in both base Si and high Si sample follow this trend, disregard of their differences in model alloy composition.

Table 4-3 Intersection angles between observed ring-shaped Ni-Si precipitates and the top surface

Model alloy	No.	Ni (at.%)	Si (at.%)	Diameter (nm)	Intersection angle with top surface {111} plane
Low Si (0%Si)	1			~30	1°
	2			~20	66°
	3			~10	68°
	4			~30	69°
	5			~20	68°
	6			~30	68°
	7			~20	75°
	8			~20	18°
Base Si (0.83at.%Si)	9	27.8	9.7	~10	70°
	10	18.2	5.8	~20	67°
High Si (1.9at.%Si)	11	29.5	17.9	~15	68°
	12	26.9	11.7	~10	72°
	13	29	16.5	~15	73°
	14	26	13.4	~15	1°
	15	59.7	35.1	~15	90°

Table 4-4 Theoretical intersection angles between {111} plane and other planes.

Surface plane	Intersection plane	Intersection angle	Remarks
{111}	{100}	54.74°	
	{110}	35.26° or 90.00°	Habit plane for perfect loops
	{111}	0° or 70.53°	Habit plane for Frank loops

Precipitate No.15 is perpendicular to the top surface, so it may lie on the {110} plane, which is the habit plane for perfect loops. Perfect loops form by the unfaulting of Frank loops, which usually appears at the latter stage of microstructure evolution compared to Frank loop formation. And precipitate No.15 is the only well-developed Ni-Si precipitate here, which should also appear at the latter stage, compared to the formation of developing Ni-Si precipitates such as precipitate No.1~6. There may be some relationship between the unfaulting of Frank loops and the growth of Ni-Si precipitates here, but more data is needed for a discussion.

So the conclusion is that a large fraction of Ni segregation is ring-shaped and may well be formed on dislocation loops. The Ni-Si precipitates are mostly spherical in shape, but the ring-shaped precipitates observed should also be formed on dislocation loops.

4.2.5 Possible existence of nano-voids

Although TEM observation found no voids in these three samples irradiated at 450°C to 5dpa, it is still possible that very tiny nano-voids may exist. Therefore, in order to get a full view of the microstructure of the three irradiated samples, the atom density isosurface map of APT is applied here to check the possible existence of such nano-voids.

The results show that in high Si and base Si sample irradiated at 450°C to 5dpa, no sign of nano-voids is found; but in low Si sample, some low atom density regions are found by isosurface maps of atom density, as shown in Fig. 4-8. The bulk average atom density detected by APT is roughly ~40 atoms/nm^3, and in Fig. 4-8 the thresholds set for atom density isosurface maps are a) 3 atoms/nm^3, b) 5 atoms/nm^3 and c) 7 atoms/nm^3, respectively. In Fig. 4-8(c), some low atom density regions are found, which are marked by blue circle. These low density regions may be nano-voids, but when the threshold value of atom density is further decreased in Fig. 4-8 (b) and (a), these regions disappeared. As a conclusion, these regions could be regarded as nano-voids, depending on the definition of nano-voids. If the observed regions are really nano-voids, the phenomenon is also reasonable, because:

- First, the oversized atom Mo is usually an indicator of nano-voids, and it is observed to be enriched at the void surface by Mo concentration isosurface map, as shown in Fig. 4-8(d).
- Second, the possible nano-voids are only observed in low Si sample here. This is consistent with the literature results that large Si content inhibits void formation [4-7].

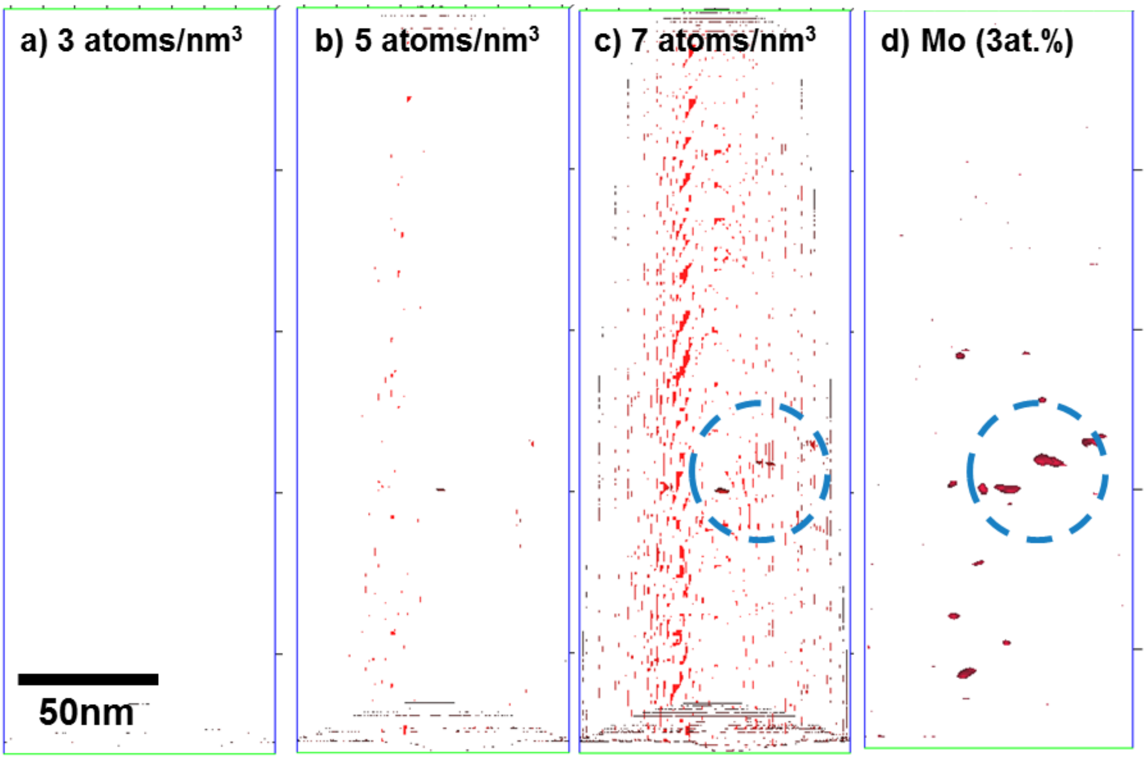

Fig. 4-8 Confirmation of possible nano-voids in low Si sample irradiated at 450°C to 5 dpa. a), b) and c) are the isosurface maps of very low atom density; d) is the isosurface map of 3at.% Mo concentration (Mo enrichment).

4.3 Ni and Si fluctuation in samples irradiated at 290°C

For comparison, the samples irradiated at 290°C to ~0.8dpa is also tested by APT to see if there is any sign of early precipitate nucleation. The atom maps of low Si samples and high Si sample are shown in Fig. 4-9. Visually in the atom maps, no precipitates could be identified, and all the elements seem to be homogenously distributed.

However, element fluctuation may still exist in these samples actually. To better clarify the possible element fluctuation, the isosurface maps of Ni concentration are drawn at the threshold value of 17at.% in Fig. 4-10(b) and Fig. 4-11(b) for low Si and high Si samples, respectively. Since the average bulk concentration of Ni in both two samples is about 13at.%, the green positions in the isosurface maps are where Ni enriches. It is found that the extent of Ni segregation in high Si sample is more severe than that in low Si sample.

One thing to note is that the APT samples did not go through electrochemical polishing process, but were finalized by 5kV Ga ions by FIB. Surely, without electrochemical polishing, the FIB process will leave its ion irradiation damage on the APT sample surface. In the case of 5kV Ga ions, the damage layer thickness should be less than 10nm by SRIM code. When comparing the top view of isosurface map in Fig. 4-10(b) and Fig. 4-11(b), it can be found that in low Si sample, the Ni segregation positions are mostly at sample surface, while in high Si sample, the segregation positions are much denser are almost everywhere. Most likely, the Ni segregation in low Si sample is mostly caused by the FIB damage during sample preparation process, not by the 3MeV heavy ion irradiation that is conducted in the HIT facility. This means the difference in the extent of Ni segregation between the two samples is actually larger than what is visually seen in the isosurface maps, or in other words, Si addition substantially promotes Ni segregation in this irradiation condition.

To further analyze the phenomenon, the isosurface map of Ni concentration and the isosurface map of Si concentration are superimposed, as shown in Fig. 4-11(c). The threshold for Ni concentration is still 17at.%, and the threshold for Si concentration is 4at.%. So this means the green positions are where Ni enriches, and the grey positions are where Si enriches.

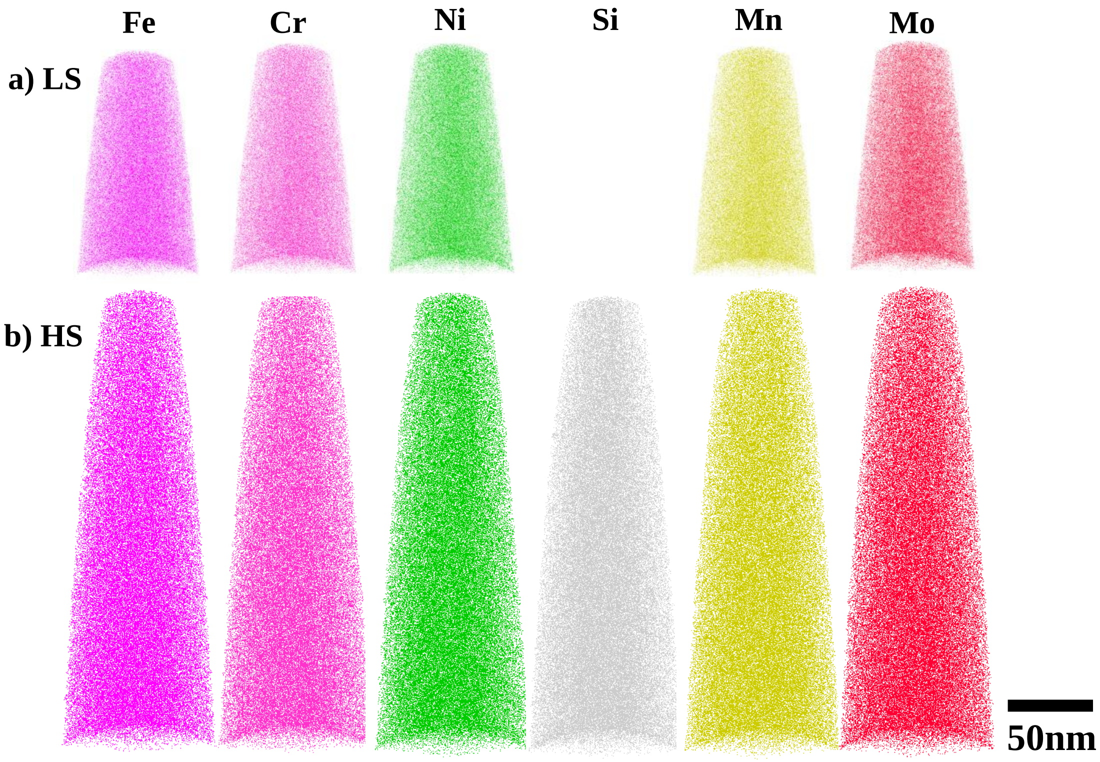

Fig. 4-9 Atom maps of a) low Si, b) high Si samples irradiated at 290°C to ~0.8dpa

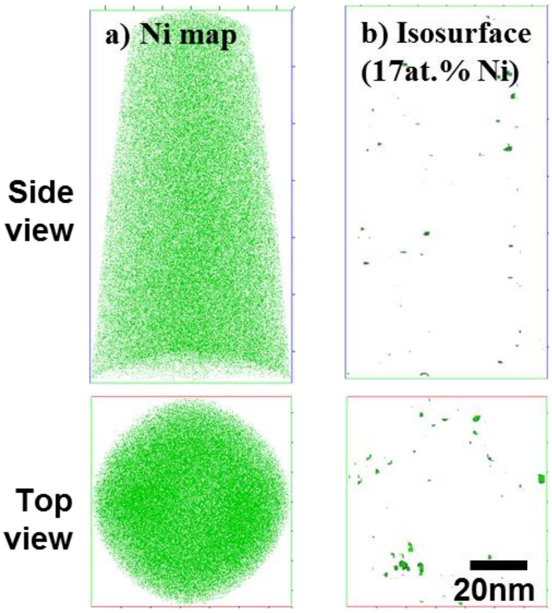

Fig. 4-10 a) Ni atom map and b) Ni isosurface map of low Si sample irradiated at 290°C to ~0.8dpa.

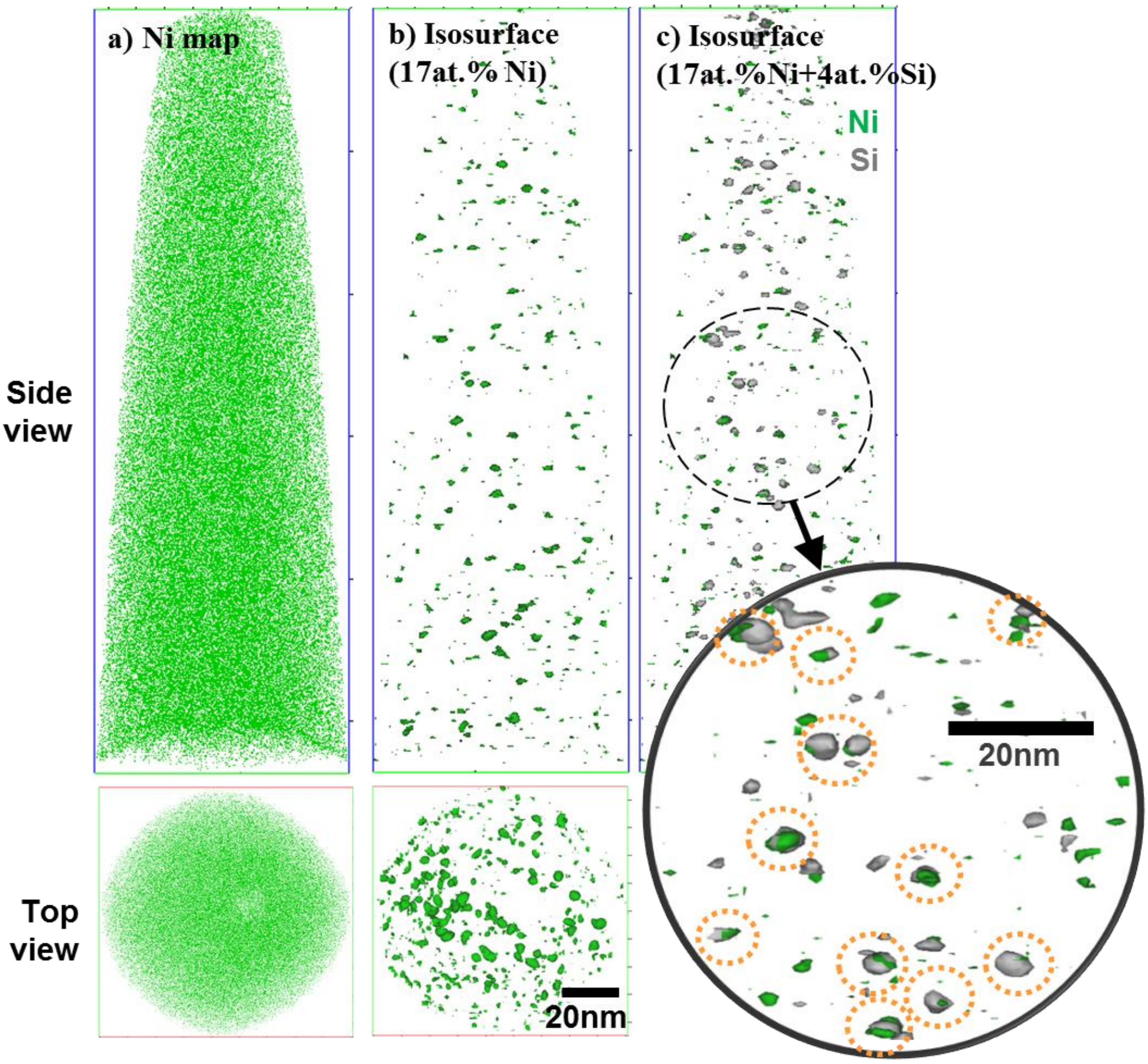

Fig. 4-11 a) Ni atom map, b) Ni isosurface map and c) superimposition of Ni and Si isosurface map of high Si sample irradiated at 290°C to ~0.8dpa. The orange circles in the enlarged figure mark the position around where Ni and Si both enriches.

The positions of Ni enrichment and the positions of Si enrichment in Fig. 4-11(c) are not randomly distributed. In the enlarged figure, it can be seen that Ni actually tends to enrich near the positions where Si enriches, which is marked by the orange circles. So the conclusion goes one step further, the Ni segregation is enhanced by Si addition, because it could segregate near the positions where Si enriches. This is interesting, because the observed Ni-Si enrichment may be the precursor of Ni-Si precipitates.

4.4 Discussion

4.4.1 Discussion on Ni segregation enhanced by Si addition

Before go into detail on experiment result analysis, the basic mechanisms of precipitate formation that is currently known are first listed here. Although the exact formation mechanisms of Ni-Si precipitates are unknown, they are usually believed to be associated with irradiation induced segregation (RIS) at sinks. The sinks could be dislocation loops, cavities, grain boundaries, stacking fault tetrahedra (SFT), point defect clusters, or maybe something else.

As an example, the schematic of Ni and Si segregation near a one-dimensional sink is drawn in Fig. 4-12. The thick black line in the figure represents the sink. In irradiation, the density of interstitials and vacancies is much higher than that in thermal equilibrium condition, so there will be considerable interstitial and vacancy fluxes diffusing toward sinks. This is the driving force of RIS.

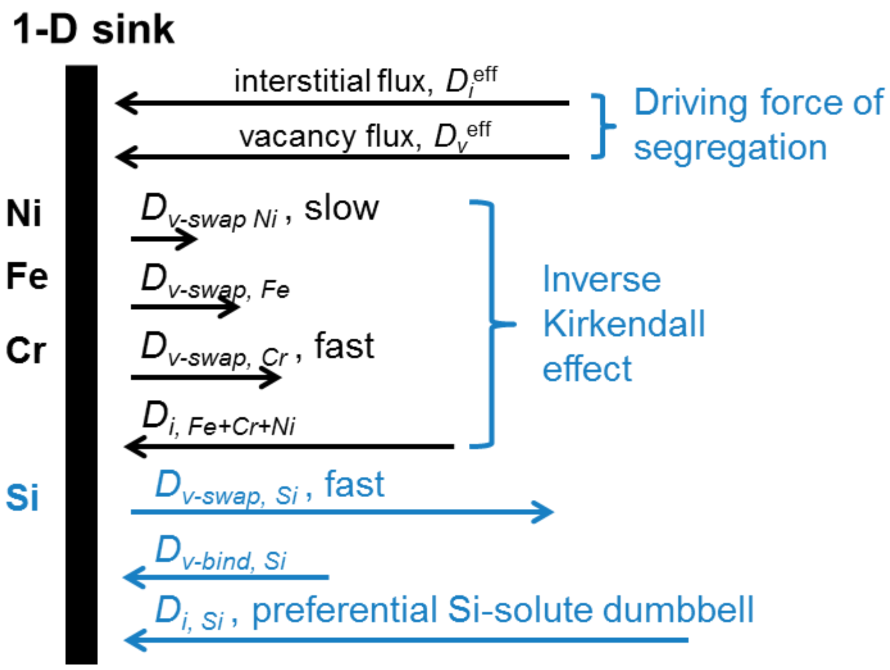

Fig. 4-12 Schematic of Ni and Si segregation near a one-dimensional sink in irradiation. The thick black line represents the sink.

When only Fe, Ni, and Cr are considered, the segregation mechanism is quite straightforward. As vacancies diffuse towards sinks, the solute atoms swap positions with vacancies. Among the three solute atoms, Cr diffuses the fastest, and Ni is the lowest. Fast diffusing elements swap positions with vacancies in higher priority, and thus diffuse upward vacancy fluxes and away from sinks. The slow diffusing solute Ni is left behind, so it diffuses downward vacancy fluxes. This is called the inverse Kirkendall effect. Through the inverse Kirkendall effect, Ni segregate at sinks, and Cr is depleted [8].

The inverse Kirkendall effect considers only vacancy diffusion mechanism, and omits solute-vacancy binding [9]. It has been successfully applied to explain the experiment data of grain boundary segregation in Fe-Cr-Ni ternary alloys [10, 11]. But when Si is added, the situation becomes complex. Si is an undersized element in stainless steel. It not only fast diffuses through vacancy swapping mechanism, but can also interact with interstitials by preferentially forming Si-solute mixed dumbbell. Besides, whether the Si-vacancy binding can be omitted or not is unclear. Currently, the enrichment of Si near sinks is usually explained as Si is dragged by interstitials downward interstitial fluxes and toward sinks [12-14]. However, Si-vacancy binding may also contribute to Si segregation, which is similar to the role of phosphorus -vacancy binding in increasing phosphorus segregation rate [15].

The local enrichment of Ni and Si near sinks is believed to cause Ni-Si precipitation.

Then, in 290°C and 0.8dpa irradiation, why Ni segregation is promoted by Si addition, and why Ni enriches near the positions of Si enrichment? It is discussed in the following two aspects:

- Does Si addition change the sinks for segregation?

No. The samples irradiated at 290°C have been analyzed by TEM in Section 3.2. It has been found that black dots are the major type of defects after irradiation, and not much difference is found in black dot number density or average size between the low Si and high Si samples. The major type of sink, black dot, is not much changed by Si addition.

- Does Si addition enhance the inverse Kirkendall effect of Ni?

Assassa et al. found by isotope tracing that when Si content is increased from 0.1wt.% to 1wt.%, the bulk diffusion coefficients of Fe, Cr and Ni are all increased for by ~40%, and the change is almost independent of temperature [16]. The increased diffusivity would enhance the inverse Kirkendall effect.

Besides, Si can fast diffuse through vacancy mechanism, faster than Cr, so possibly the Si diffusing via vacancy mechanism may also enhance the inverse Kirkendall effect of Ni.

To quantitatively analyze the segregation mechanism in the future, the one-dimensional diffusion modeling work near sinks is needed. The contribution of this current work is that the 1-D line scanning results obtained by APT could be good reference data for the future comparison with modeling work. Such a typical 1-D line scanning across a sink is shown in Fig. 4-13.

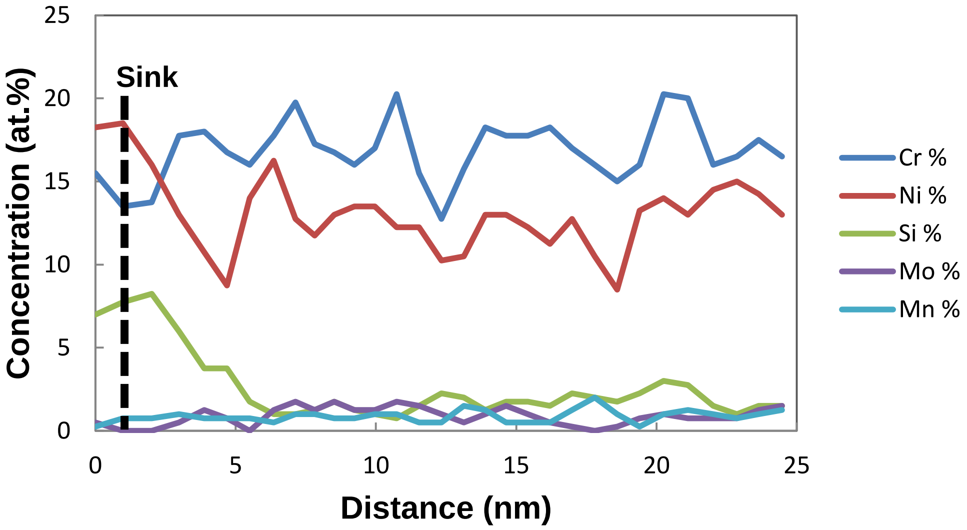

Fig. 4-13 A typical 1-D line scanning across a position where Ni and Si enriches obtained by APT.

4.4.2 Discussion on the possibility of precipitates formed on loops

As discussed in the previous section, Ni and Si atoms can be enriched at sinks by irradiation induced segregation (RIS), and may then cause Ni-Si precipitation. Since dislocation loops are just a typical site for such segregation [17-19], the relationship between Ni-Si precipitates and dislocation loops needs to be investigated.

Direct proofs to support the formation of Ni-Si precipitates on loops are still lacking. The difficulty lies in the available observation techniques. TEM is sensitive to dislocation loops but insensitive to Ni-Si precipitates, while APT is sensitive to Ni-Si precipitates but insensitive to dislocation loops. Since the specimen requirement of APT and TEM are very different, currently it is really difficult to prepare a specimen that could be first observed under TEM and then be tested by APT.

As a result of the limitation in observation technique, researchers could only attempt to find indirect proofs for the relationship between loops and precipitates. For example, since TEM and APT could not be performed on the same specimen, the statistical number density of dislocation loops in the TEM specimen is compared with that of Ni-Si precipitates in the APT specimen. Toyama et al. and Renterghem et al. found that the number density of Ni-Si precipitates is nearly one order of magnitude higher than that of Frank loops, thereby strongly suggesting that Ni-Si precipitates mainly exist at sites independent of Frank loops [20, 21]. Etienne et al. compared the density of dislocation loops with that of Ni-Si precipitates at different doses, and found both densities are in the same order of magnitude(about 10^{22}~$10^{23}m^{3}$), but the precipitates density is evidently higher [22]. However, since the size of precipitates is usually smaller than dislocation loops [22], the possibility that several precipitates form on the same dislocation loop could not be excluded.

The shape of precipitates has also been compared with dislocation loops. Jiao et al. found one ring-shaped precipitates in atom map, and believed that it is formed on dislocation loops [23]. The torus-shaped Ni-Si precipitates found by Etienne et al. by APT also have similar shape with dislocation loops [24].

In this work, not only some ring-shaped precipitates are found in atom maps, but their orientations are further examined with the help of EBSD. Although it is still not a direct proof, it puts more weight on the assumption that at least some fraction of Ni-Si precipitates form on dislocation loops. The phenomenon that the only observed well-developed ring-shaped precipitates may form on perfect loop instead of Frank loops is also inspiring. There are two possible explanations:

- One possibility is that the development of Ni-Si precipitates goes along with the growth and unfaulting of dislocation loops, and the Frank loops decorated by precipitates can also unfault.
- Another possibility is that perfect loops may be a stronger sink for Ni and Si segregation than Frank loops. The perfect loops may quickly form by unfaulting or form directly by irradiation when irradiation dose is still low. In this way, the Ni-Si precipitates near perfect loops can be better developed than those near Frank loops.

Honestly speaking, the orientation analysis by plane intersection angle has its uncertainties. A better way to identify the crystal plane orientation in atom maps may be using the method of Radiguet et al. [25] or Hatakeyama et al. [26]. The two methods will be attempted in my future work.

4.4.3 Discussion on the composition of Ni-Si precipitates

The γ' phase (Ni_3Si) in irradiated stainless steel was first discovered under TEM by its diffraction pattern [27, 28]. Due to the similarity between γ' phase precipitates and γ phase matrix, the contrast of γ' phase is very weak under TEM. The only method to see γ' phase under TEM is to make use of its diffraction pattern. Usually, even if the <100> diffraction spot of γ' phase is too weak to be seen in the diffraction pattern, by putting the objective aperture at the position where the <100> diffraction spot should be, the γ' phase could be observed in the corresponding dark field images [29-33]. By TEM observation, the γ' phase precipitates are found to be an irradiation-induced second phase, which will dissolve by post irradiation thermal annealing [32]. They form in the temperature region of roughly 400~540ºC [4].

However, this observation method assumes that these Ni and Si enriched precipitates are exactly the γ' phase. This assumption itself is questionable. Although the γ' phase has been observed under TEM, it does not mean that these precipitates consist of only the γ' phase. Theoretically, the so-called "γ' phase precipitates" observed in irradiated stainless steel by TEM could actually be a mixture of different Ni-Si phases.

But when the <100> diffraction spot of the γ' phase is used for Ni-Si precipitate observation, the other possible Ni-Si phases are automatically excluded in the TEM dark field images.

The recent development of APT technology makes the detailed analysis of Ni-Si precipitates possible. In this work, the Ni/Si atom ratio in Ni-Si precipitates is discovered to be smaller than 3, which indicates these Ni-Si precipitates should not be the exactly the standard γ' phase. Similar composition analysis of precipitates has been previously done by some other researchers. Krummeich et al. found the precipitates formed in Ni ion irradiation have a stoichiometry close to Ni_3Si [34]. Etienne et al. further discovered that depending on the shape of formed precipitates, the Ni/Si ratio could be close to 3 or smaller than 3 [22, 24, 35]. Jiao et al. irradiated two types of alloys (HP316+Si and CP316 stainless steels), and found that in CP316 stainless steel (0.65 wt.% Si) the Ni/Si ratio of precipitates is close to 3, but in HP316+Si stainless steel (1.05 wt.%Si) the Ni/Si ratio turns to be ~2.2 [23]. Toyama et al. also found in neutron irradiation that the Ni/Si ratio of precipitates is ~3[21].

Based on the literature results of APT experiments above, generally there are two opinions on the composition of Ni-Si precipitates formed in irradiated stainless steels:

1) Ni/Si atom ratio is close to 3;
2) Ni/Si atom ratio is evidently smaller than 3.

Notice that no reports of Ni/Si atom ratio much larger than 3 are found.

It is natural to think that it is the differences in their experimental condition that lead to the differences in observed Ni/Si atom ratio. However, since the irradiation and APT analysis parameters could be very different between different research groups, a direct comparison between their experiment conditions could be almost meaningless. But if the comparison is restricted within the data from the same research group, then only very limited information could be extracted. In fact, as APT studies on precipitation in stainless steel have just started in recent years, systematic work done by one research group with key parameter tuning is still lacking. The work of Jiao et al. indicates that the purity level of stainless steel plays a key role in the Ni/Si atom ratio, but the two types of alloys they used in their work differs not only in Si content, but in Ni, S and C contents as well [23]. The composition differences between the two alloys are too large to perform a mechanism analysis. Etienne et al. categorized Ni-Si precipitates into different types by their shape, and found that the Ni/Si atom ratio depends on precipitate shape [24]. But the differences in precipitate shape do not mean the differences in formation mechanisms. Precipitates of different shapes may be just on different growing stages, and one shape of precipitates may grow into another shape if provided with larger irradiation dose. The important question “where do these differences in precipitate shape come from” remains unknown.

As a conclusion, by literature results, the key factors that determine the Ni/Si atom ratio to be close to 3 or smaller than 3 seem to be complicated. The key factors may be alloy composition (especially Si content), precipitate forming conditions, growing stages, or something else.

Table 4-6 Literature data of Ni-Si precipitate composition analyzed by APT

Reference	Cr (at.%)	Ni (at.%)	Si (at.%)	Ni/Si atom ratio	Remarks
[23]	8.51	34.3	15.7	2.2	HP304+Si alloy
	14.5	21.7	7.1	3.1	CP304 alloy
[24, 35]	10.2	28.2	12.3	2.3	Lenticular rounded shape precipitates
	10.7	25.6	7.6	3.4	Torus-shaped precipitates
[36, 37]	14.5	15.6	4.8	3.3	Si enriched regions
	1.2	53.9	38.1	1.4	Ni-Si clusters
[21]	~10	40~50	15~20	~3 or smaller	

In this work, this topic is further discussed by strictly controlling the model alloy composition, irradiation condition and APT analysis parameters, so that the only variable here is the Si content (0~0.95wt.%). As previously shown in Fig. 4-6, the precipitate composition is different in base Si and high Si sample, but the Ni/Si atom ratio seems to follow the same trend against the Si concentration of the precipitate. It seems that the Si content of model alloy does not change the Ni-Si precipitate formation mechanism, but just limits the growing rate of Ni-Si precipitates. And most probably, it is the growing stage of Ni-Si precipitates that determines the Ni/Si ratio. In Fig. 4-6, developing Ni-Si precipitates with Si concentration below ~10% have the Ni/Si atom ratio of ~3; but in Ni-Si precipitates with Si concentration above ~10%, the Ni/Si ratio decreases.

If literature data are also compared in this way, then similar trend could be extracted, as listed in Table 4-6. In Table 4-6, developing Ni-Si precipitates with low Si concentration has Ni/Si atom ratio close to 3, and the Ni/Si atom ratio of other precipitates are much smaller. Toyama et al. concluded that the Ni/Si ratio in their experiment is around 3, but based on their figure it should be actually a little smaller than 3 in average [21]. Besides, Etienne et al. discovered that as irradiation temperature increases from 300°C to 400°C, the Si enrichment factor in precipitates increases much faster than that of Ni [22]. Since higher temperature accelerates the development of Ni-Si precipitates in this temperature regime, it is in consistency with the conclusion in this study.

Notice that Toyama et al. have attempted to plot Ni/Si atom ratio against the diameter of Ni-Si precipitates in their work, but did not find any meaningful trend [22]. There are three possible causes for their results:

1) Under the condition of their neutron irradiation, the Ni/Si atom ratio of precipitates may actually keep constant.
2) The diameter of precipitates is strongly depending on the definition of Ni-Si precipitates. The key parameters in precipitate definition could be: the element (Ni or Si or both) selected for definition, the value of atom distance, and the value of minimum atom number in precipitates. The different selection of these values could alter the precipitate diameter measured in atom map. Thus the precipitate diameter is not an ideal parameter for plotting.
3) Precipitate diameter may not properly represent the growing stage of precipitates, especially for those precipitates that are not spherical in shape (e. g. ring shape).

Thus in this work, the Si concentration of each precipitate core (a Φ3nm sphere) is used to represent the growing stage of precipitates, because as Ni-Si precipitate grows, not only its size increase, but its Ni and Si concentration will also increases. In this way, the uncertainty of precipitate definition and shape factors could be avoided, and the reliability of the composition analysis could be improved.

Therefore, generally speaking, there are two possibilities to explain for the observed deviation of Ni/Si atom ratio in precipitates:

1) There may be other Ni-Si phases in the precipitates besides the Ni_3Si γ' phase, such as $Ni_{31}Si_{12}$, Ni_5Si_2 or Ni_2Si [38]. If Ni-Si precipitates can be a mixture of γ' phase and other phases, this would explain the reason why usually only a very limited fraction of precipitates are visible under TEM using ***g***=<100> of γ' phase, compared to the APT observation results of all kinds of Ni-Si precipitates [2]. Besides, the formation rate of the other phases should be slower than that of the γ' phase, so that the deviation become distinct only when the Ni-Si precipitates are well developed in irradiated stainless steel. G phase is often observed in irradiated stainless steel under large dose [39, 40], but it is not a good candidate here as its Ni/Si ratio is even larger than 3 [41].
2) Another possibility is that the Ni-Si precipitates observed in APT may be only the γ' phase, but there are large amount of defects formed in the γ' phase precipitates to cause ratio deviation, which is usually the case in irradiated materials. Ni vacancies or Si interstitials or some other types of defects may be responsible for the Ni/Si atom ratio deviation observed here. They accumulate during the growing process of γ' phase, so the deviation in atom ratio is larger when the γ' precipitate is well-developed.

In Chapter 5, the possibility of defect formation in γ' precipitate is discussed. The stability of different kinds of single defects formed in the γ' phase is tested by first principle calculation.

4.5 Summary

In this chapter, two irradiation conditions are selected for further analysis by APT. The 450°C and 5dpa condition is selected because Ni-Si precipitates are most likely to form; the 290°C and ~0.8dpa condition is selected because there may be sign of precipitate precursors. The results are:

1) Addition of Si promotes Ni segregation at 290°C, although black dots, the major sinks in this condition, are actually not much changed by Si addition. Ni tends to enrich near positions of Si enrichment in high Si sample, which may be the precursor of Ni-Si precipitates.
2) Ni-Si precipitates are found in base Si and high Si samples irradiated at 450°C. Ni/Si atom ratio is quite close to 3 in developing Ni-Si precipitates with low Si and Ni concentration. But in well-developed Ni-Si precipitates, Ni/Si atom ratio turns to be lower than 3 while maintaining Ni+Si≈96at.%. The accumulation of defects or phases other than the γ’ phase during precipitate development may be responsible for the deviation in stoichiometry. Mo and Mn are fully depleted at an early stage of precipitate formation.
3) Some ring-shaped precipitates are observed at 450°C. Base on shape, size and orientation, they may well form on dislocation loops.

References in Chapter 4

[1] B. Radiguet, A. Etienne, P. Pareige, et al. Irradiation behavior of nanostructured 316 austenitic stainless steel. J Mater Sci, 2008, 43 (23-24): 7338-7343.

[2] K. Fukuya. Current understanding of radiation-induced degradation in light water reactor structural materials. J Nucl Sci Technol, 2013, 50 (3): 213-254.

[3] T. Hamaoka, A. Nomoto, K. Nishida, et al. Accurate determination of the number density of G-phase precipitates in thermally aged duplex stainless steel. Philos Mag, 2012, 92 (22): 2716-2732.

[4] N. Sekimura, F. A. Garner, J. W. Newkirk. Silicons Role in Determining Swelling in Neutron-Irradiated Fe-Ni-Cr-Si Alloys. J Nucl Mater, 1992, 191: 1244-1247.

[5] Z. Jiao, J. T. Busby, G. S. Was. Deformation microstructure of proton-irradiated stainless steels. J Nucl Mater, 2007, 361 (2-3): 218-227.

[6] F. A. Garner, H. R. Brager. The Influence of Mo, Si, P, C, Ti, Cr, Zr and Various Trace-Elements on the Neutron-Induced Swelling of Aisi-316 Stainless-Steel. J Nucl Mater, 1988, 155: 833-837.

[7] F. A. Garner, W. G. Wolfer. Factors Which Determine the Swelling Behavior of Austenitic Stainless-Steels. J Nucl Mater, 1984, 122 (1-3): 201-206.

[8] E. P. Simonen, S. M. Bruemmer. Radiation effects on environmental cracking of stainless steels. Jom-Journal of the Minerals Metals & Materials Society, 1998, 50 (12): 52-55.

[9] A. D. Marwick. Segregation in Irradiated Alloys - Inverse Kirkendall Effect and Effect of Constitution on Void Swelling. J Phys F Met Phys, 1978, 8 (9): 1849-1861.

[10] T. R. Allen, G. S. Was. Modeling radiation-induced segregation in austenitic Fe-Cr-Ni alloys. Acta Mater, 1998, 46 (10): 3679-3691.

[11] T. R. Allen, J. T. Busby, G. S. Was, et al. On the mechanism of radiation-induced segregation in austenitic Fe-Cr-Ni alloys. J Nucl Mater, 1998, 255 (1): 44-58.

[12] P. J. Maziasz. Formation and Stability of Radiation-Induced Phases in Neutron-Irradiated Austenitic and Ferritic Steels. J Nucl Mater, 1989, 169: 95-115.

[13] G. S. Was, J. P. Wharry, B. Frisbie, et al. Assessment of radiation-induced segregation mechanisms in austenitic and ferritic-martensitic alloys. J Nucl Mater, 2011, 411 (1-3): 41-50.

[14] P. R. Okamoto, Wiedersi.H. Segregation of Alloying Elements to Free Surfaces during Irradiation. J Nucl Mater, 1974, 53 (1): 336-345.

[15] S. M. Murphy, J. M. Perks. Analysis of Phosphorus Segregation in Ion-Irradiated Nickel. J Nucl Mater, 1990, 171 (2-3): 360-372.

[16] W. Assassa, P. Guiraldenq. Bulk and grain boundary diffusion of 59Fe, 51Cr, and 63Ni in austenitic stainless steel under influence of silicon content. Metal Science, 1978, 12 (3): 123-128.

[17] P. J. Maziasz, C. J. Mchargue. Microstructural Evolution in Annealed Austenitic Steels during Neutron-Irradiation. Int Mater Rev, 1987, 32 (4): 190-219.

[18] S. J. Zinkle, P. J. Maziasz, R. E. Stoller. Dose Dependence of the Microstructural Evolution in Neutron-Irradiated Austenitic Stainless-Steel. J Nucl Mater, 1993, 206 (2-3): 266-286.

[19] S. M. Bruemmer, E. P. Simonen, P. M. Scott, et al. Radiation-induced material changes and susceptibility to intergranular failure of light-water-reactor core

internals. J Nucl Mater, 1999, 274 (3): 299-314.
[20] W. Van Renterghem, A. Al Mazouzi, S. Van Dyck. Influence of post irradiation annealing on the mechanical properties and defect structure of AISI 304 steel. J Nucl Mater, 2011, 413 (2): 95-102.
[21] T. Toyama, Y. Nozawa, W. Van Renterghem, et al. Irradiation-induced precipitates in a neutron irradiated 304 stainless steel studied by three-dimensional atom probe. J Nucl Mater, 2011, 418 (1-3): 62-68.
[22] A. Etienne, B. Radiguet, P. Pareige. Understanding silicon-rich phase precipitation under irradiation in austenitic stainless steels. J Nucl Mater, 2010, 406 (2): 251-256.
[23] Z. Jiao, G. S. Was. Novel features of radiation-induced segregation and radiation-induced precipitation in austenitic stainless steels. Acta Mater, 2011, 59 (3): 1220-1238.
[24] A. Etienne, B. Radiguet, N. J. Cunningham, et al. Atomic scale investigation of radiation-induced segregation in austenitic stainless steels. J Nucl Mater, 2010, 406 (2): 244-250.
[25] B. Radiguet, A. Barbu, P. Pareige. Understanding of copper precipitation under electron or ion irradiations in FeCu0.1 wt% ferritic alloy by combination of experiments and modelling. J Nucl Mater, 2007, 360 (2): 104-117.
[26] M. Hatakeyama, I. Yamagata, Y. Matsukawa, et al. Direct observation of solute-dislocation interaction on extended edge dislocation in irradiated austenitic stainless steel. Phil Mag Lett, 2014, 94 (1): 18-24.
[27] C. Cawthorne, C. Brown. Occurrence of an Ordered Fcc Phase in Neutron-Irradiated M316 Stainless-Steel. J Nucl Mater, 1977, 66 (1-2): 201-202.
[28] H. R. Brager, F. A. Garner. Swelling as a Consequence of Gamma Prime Gamma ' and M23(C,Si)6 Formation in Neutron-Irradiated 316 Stainless-Steel. J Nucl Mater, 1978, 73 (1): 9-19.
[29] S. I. Porollo, Y. V. Konobeev, F. A. Garner. Swelling and microstructure of austenitic stainless steel ChS-68 CW after high dose neutron irradiation. J Nucl Mater, 2009, 393 (1): 61-66.
[30] S. Cisse, L. Laffont, M. C. Lafont, et al. Influence of localized plasticity on oxidation behaviour of austenitic stainless steels under primary water reactor. J Nucl Mater, 2013, 433 (1-3): 319-328.
[31] K. Fukuya, K. Fujii, H. Nishioka, et al. Evolution of microstructure and microchemistry in cold-worked 316 stainless steels under PWR irradiation. J Nucl Sci Technol, 2006, 43 (2): 159-173.
[32] H. R. Brager, F. A. Garner. Stability of the Radiation-Induced Gamma'-Phase in 316 Stainless-Steel. J Nucl Mater, 1983, 116 (2-3): 267-271.
[33] K. Fukuya, M. Nakano, K. Fujii, et al. Separation of microstructural and microchemical effects in irradiation assisted stress corrosion cracking using post-irradiation annealing. J Nucl Sci Technol, 2004, 41 (12): 1218-1227.
[34] R. Krummeich, P. Pareige, J. P. Massoud, et al. Solute cluster formation in austenitic and ferritic alloys under ion irradiation: a three-dimensional atom probe characterization. Surf Interface Anal, 2004, 36 (5-6): 575-580.
[35] A. Etienne, B. Radiguet, N. J. Cunningham, et al. Comparison of radiation-induced segregation in ultrafine-grained and conventional 316 austenitic stainless steels. Ultramicroscopy, 2011, 111 (6): 659-663.
[36] A. Etienne, B. Radiguet, P. Pareige, et al. Tomographic atom probe characterization

of the microstructure of a cold worked 316 austenitic stainless steel after neutron irradiation. J Nucl Mater, 2008, 382 (1): 64-69.

[37] P. Pareige, A. Etienne, B. Radiguet. Experimental atomic scale investigation of irradiation effects in CW 316SS and UFG-CW 316SS. J Nucl Mater, 2009, 389 (2): 259-264.

[38] D. Connetable, O. Thomas. First-principles study of nickel-silicides ordered phases. J Alloy Compd, 2011, 509 (6): 2639-2644.

[39] F. A. Garner, H. R. Brager. The Role of Phosphorus in the Swelling and Creep of Irradiated Austenitic Alloys. J Nucl Mater, 1985, 133 (Aug): 511-514.

[40] E. H. Lee, L. K. Mansur. Relationships between Phase-Stability and Void Swelling in Fe-Cr-Ni Alloys during Irradiation. Metall Trans A, 1992, 23 (7): 1977-1986.

[41] K. L. Holman, E. Morosan, P. A. Casey, et al. Crystal structure and physical properties of Mg6Cu16Si7-type M6Ni16Si7, for M = Mg, Sc, Ti, Nb, and Ta. Mater Res Bull, 2008, 43 (1): 9-15.

5. Precipitate preferential structure by first principle calculation

5.1 Modeling methodology

In Section 4.2, the deviation of Ni/Si atom ratio in precipitates is experimentally discovered by APT. In this chapter, the possibility of defect formation in γ’ phase altering its Ni/Si atom ratio is discussed by first principle calculation.

5.1.1 DFT modeling

Density functional theory (DFT) is a widely-used modeling tool to calculate the electronic structure of many-body system. It can be applied to find out the preferential atom configurations of a given structure and its corresponding total system energy. The DFT calculation is based on the two Hohenberg–Kohn theorems [1]:

- Theorem 1: The external potential is a unique function of the electron density of ground state.
- Theorem 2: The electron density that minimizes the total system energy is the ground state electron density.

One step further, the Kohn–Sham formulation assumes an effective potential in which non-interacting electron moves, instead of the intractable actual interacting system with the real potential. This much simplifies the interactions in the system.

The Vienna ab-initio simulation package (VASP) code uses plane-wave pseudopotential of Kohn-Sham DFT to approximate electron density, and is suitable in the case of infinite periodic systems, such as pure iron, crystalized Ni_3Si (γ’ phase), and so on.

The DFT calculation in body-centered-cubic (BCC) pure iron (reactor pressure vessel steels) is already quite mature, but in stainless steel the attempts have just started [2]. The difficulty lies in its multicomponent nature and magnetism [3]. The magnetism plays a key role in the stability of face-centered-cubic (FCC) phase austenite steel. Outstanding work has been done by Klaver et al. [3], and was followed by Bonny et al. [4-6], but the current modeling results of FCC austenite steel are still not satisfactory enough.

Therefore, in this work, only the γ’ phase is focused on. VASP 5.3 code is used to simulate Ni_3Si structure with single defect.

5.1.2 Parameter selection

The most important parameters in VASP calculation are the selection of exchange-correlation function, pseudopotential, superlattice size, cut-off energy and k-point mesh. As a reference, the parameters used by previous related calculation works in literature are summarized in Table 5-1.

- Exchange-correlation function.

There are two popular methods to approximate exchange-correlation energy: local density approximation (LDA) and generalized gradient approximation (GGA). LDA assumes the electron density to be homogenous, while GGA assumes a gradient of electron density. Various GGA methods have been proposed by previous researchers on how to set the electron gradient, such as PBE, PW91, Pedrew92. Of course, GGA is an improvement of LDA approximation, and requires more computing capacity.

In this study, LDA approximation is used.

Table 5-1 Key VASP parameters selected in previous studies

Material	Exchange correlation function	Pseudo-potential	Cut-off Energy (eV)	Cell size (atom/cell)	k-point mesh	Ref.
Ni_3Si	PBE-GGA	PAW	400 ~500	~80	4×4×8, 17×17×17	[7]
Ni_3Si	PW91-GGA	PAW	400	-	> 8000	[8]
fcc-$FeNi_3$	Pedrew92-GGA	USPP, PAW	-	-	-	[2]
fcc-Fe	Pedrew92-GGA	PAW	300~600	256	2×2×2, 16×16×16 ~20×20×20	[3]
Ni_3Si	GGA, LDA	USPP	400	-	10×10×10	[9]

- Pseudopotential.

To reduce the amount of calculation, the core electrons are assumed to be unchanged and only valance electrons are considered. The influence of core electrons is represented by pseudopotential approximation. Traditionally, ultra-soft pseudo-potential (USPP) is used, but recently (projector augmented wave) PAW has also been applied in many works.

To lessen the requirement of computing capacity, USPP is used in this work.

- Cut-off energy and k-point mesh.

Cut-off energy and k-point sampling mesh are two key parameters that define the accuracy during calculation process. K-point sampling is conducted by a Monkhorst-pack scheme.

To find out a balance between accuracy and computing capacity requirement in the γ' phase system, some test runs on parameter optimization are performed. Superlattice of 32 atoms is constructed, and then cut-off energy and k-point sampling points are tuned to see their influences on system total energy (TOTEN), as shown in Fig. 5-1. When cut-off energy is bigger than 400eV and k-point mesh is larger than 5×5×5, the TOTEN does not change, which means the accuracy is high enough. Thus, cut-off energy of 400eV ad k-point mesh of 5×5×5 is used in this study.

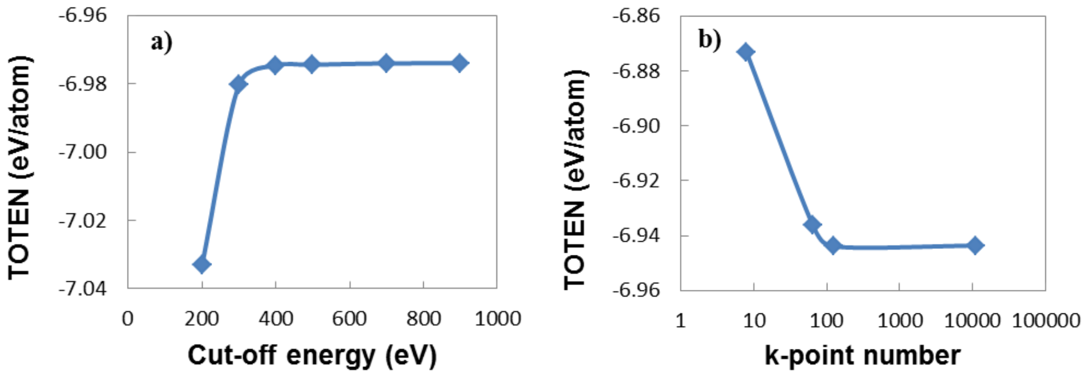

Fig. 5-1 VASP test runs on parameter optimization of a) cut-off energy, b) k-point mesh

- Other major parameters.

ISPIN=2. Electron spin is considered in all elements. The MAGMOM tag is not manually set and is using the default value. It means the initial magnetic moments for each element are all set to 1 [10].

IBRION=1. RMM-DIIS quasi-Newton algorithm is used during relaxing process. This method is slow but accurate.

ISIF=3. Stress tensor is calculated in all process. It is slow but accurate.

EDIFF = 10^{-4} eV/atom, EDIFFG = 10^{-4} eV/atom. The accuracy for solving Kohn–Sham equation and relaxing process are both fixed at 10^{-4} eV/atom.

5.1.3 Definition of defect formation energy

In this study, different types of single defect are introduced into the perfect Ni_3Si lattice, to study the stability of Ni_3Si structure and its tendency to incorporate single defects. As the first step, the way to calculate formation energy of single defect needs to be defined. In this study, single defect formation energy is defined in the similar way as that in the previous work of Udagawa et al. [11, 12].

For one interstitial defect:

$$E_{f,\mathrm{d}} = E_{tot}(Ni_{3x}Si_x + M) - E_{tot}(Ni_{3x}Si_x) - \frac{E_{tot}(M_y)}{y} \tag{5-1}$$

For one vacancy defect:

$$E_{f,d} = E_{tot}(Ni_{3x}Si_x - M) + \frac{E_{tot}(M_y)}{y} - E_{tot}(Ni_{3x}Si_x) \tag{5-2}$$

For one substitutional defect:

$$E_{f,d} = E_{tot}(Ni_{3x}Si_x - M + N) + \frac{E_{tot}(M_y)}{y} - E_{tot}(Ni_{3x}Si_x) - \frac{E_{tot}(N_z)}{z} \tag{5-3}$$

Where $E_{f,\,d}$ is the single defect formation energy;

E_{tot} is the system total energy calculated by VASP;

M and N are atoms as interstitial, vacancy or substitution. Their reference states are M_y (with y M atoms) and N_z (with z N atoms), respectively; The related reference states used here are fcc-Ni, diamond-Si, bcc-Fe and bcc-Cr. In fact, the selection of reference states here is not very satisfying. Ideally, the formation of single defect in γ’ phase is a process of atom exchange between the γ’ phase and the γ austenite matrix. So the reference state should be the γ austenite matrix. However, the stability of γ austenite phase mainly comes from its magnetism, which is very difficult to simulate currently. A usual practice is to use its corresponding stable single substance phase as the reference [3]. Of course, for future simulation with higher reliability, the use of γ austenite matrix as the reference is necessary.

$Ni_{3x}Si_x$ is the standard γ’ phase superlattice which contains 3x Ni atoms and x Si atoms.

By this definition, the defect formation energy $E_{f,\,d}$ for standard γ’ phase (Ni_3Si) is 0. $E_{f,\,d}>0$ means this kind of defect tends to form in the standard γ’ phase thermodynamically, while $E_{f,\,d}<0$ means this defect is unstable.

Moreover, the phase formation energy $E_{f,\,p}$ of γ’ phase may be useful when comparing with other results. It represents the process how single substances (Ni and Si) form chemical compound (Ni_3Si). It is defined like this [3]:

$$E_{f,p}(Ni_{3x}Si_x) = \frac{\{(E_{tot}(Ni_{3x}Si_x) - E_{tot}(Ni_{3x}) - E_{tot}(Si_x)\}}{3x + x} \qquad (5\text{-}4)$$

Here Ni_{3x} and Si_x also mean the reference states of Ni and Si, which are fcc-Ni and diamond-Si, respectively. Unlike the previously-defined single defect formation energy, the phase formation energy here is standardly defined and is comparable with literature data.

5.2 Results of calculated defect formation energy

5.2.1 Perfect γ’ phase lattice

First, the perfect γ’ phase lattice without defects is modeled in VASP. The Ni_3Si γ’ phase is a cubic lattice (named as $L1_2$ or cP4 structure), with Ni atoms at face center positions and Si atoms at vertex positions, as shown in Fig. 5-2. Each primitive cell contains three Ni atoms and one Si atom.

In this VASP calculation, a superlattice containing 32 atoms (2×2×2 primitive cells with 24 Ni atoms and 8 Si atoms) is constructed, as shown in Fig. 5-3.

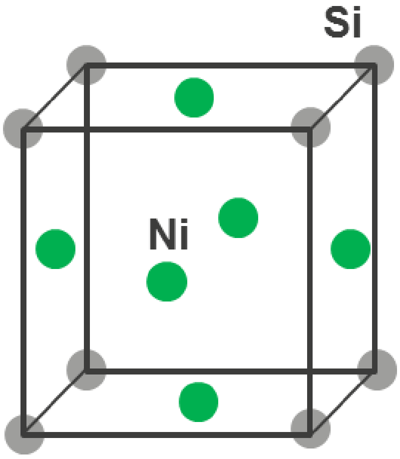

Fig. 5-2 Perfect γ’ phase lattice (Ni_3Si)

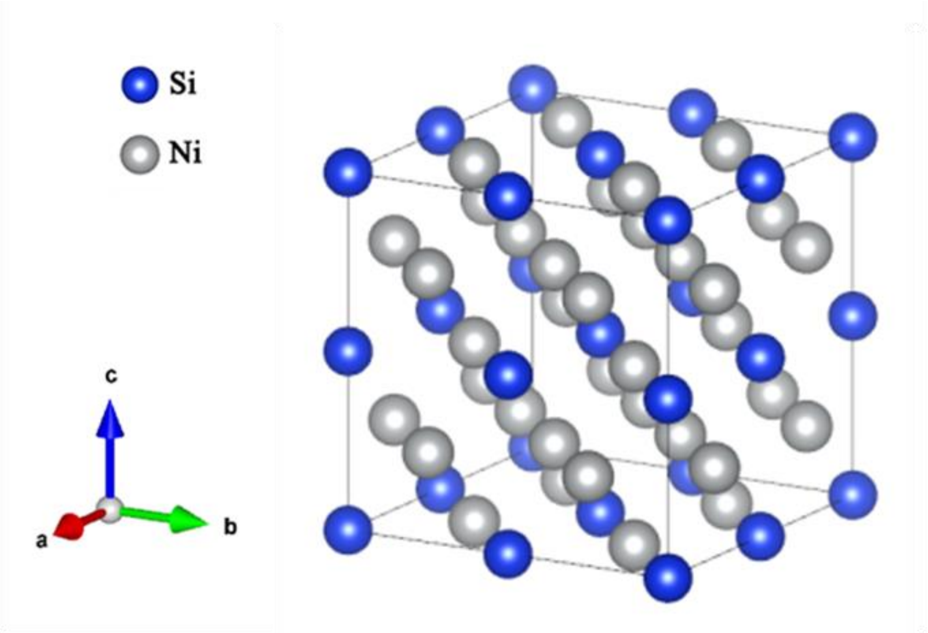

Fig. 5-3 32-atom superlattice constructed in VASP calculation (Ni_3Si)

After relaxing, the phase formation energy for perfect γ’ is $E_{f,p}$=-0.5421 eV/atom, and lattice constant a = 0.3437nm. These two values are compared with previous experiment and modeling results using VASP or Computer Coupling of Phase Diagrams and Thermochemistry (CALPHAD), as shown in Table 5-2. The lattice constant a_0 calculated here is very similar to previous results. For phase formation energy, the scattering in previous data is quite large. This may well due to the selection of modeling method in different previous works. When using GGA instead of LDA as exchange correlation function, the resultant phase formation energy is larger. But anyway the result here matches the data previously calculated by LDA ($E_{f,p}$=-0.558) [9]. This puts weight on the reliability of calculation in this study.

Table 5-2 Experiment and modeling results on perfect γ’ phase

	This study	Modeling		Experiment
a_0 (nm)	0.3437	0.343 [13]	Thermo-Calc	0.3500 [14] 0.3506 [15]
		0.3437 [9]	CASTEP (LDA, USPP)	
		0.3460 [16]	Quasi-harmonic Debye model	
		0.3512 [7]	VASP (GGA, PAW)	
		0.3516 [9]	CASTEP (GGA, USPP)	
$E_{f,p}$ (eV/atom)	-0.5421	-0.416 [17]	DFT (LDA, FLMTO)	-0.447 [18] -0.467 [19]
		-0.444 [9]	CASTEP (GGA, USPP)	
		-0.463 [7]	VASP (GGA, PAW)	
		-0.510 [20]	CALPHAD (FLMTO)	
		-0.511 [21]	-	
		-0.558 [9]	CASTEP (LDA, USPP)	

5.2.2 Vacancy defect

The single vacancy defect means one Ni atom or one Si atom is removed from the perfect γ' phase lattice. Since the Ni positions in γ' phase are all equivalent, only one configuration needs to be considered for Ni vacancy. So is the case for Si vacancy. The schematic of single vacancy defect configuration is illustrated in Fig. 5-4.

To produce single Ni vacancy defect in the constructed 32-atom superlattice, one Ni atom is removed at ($0.25a_0$, $0.5a_0$, $0.25a_0$) position. This is used as the initial configuration for relaxing process. For single Si vacancy defect, one Si atom at ($0.5a_0$, $0.5a_0$, $0.5a_0$) position is removed.

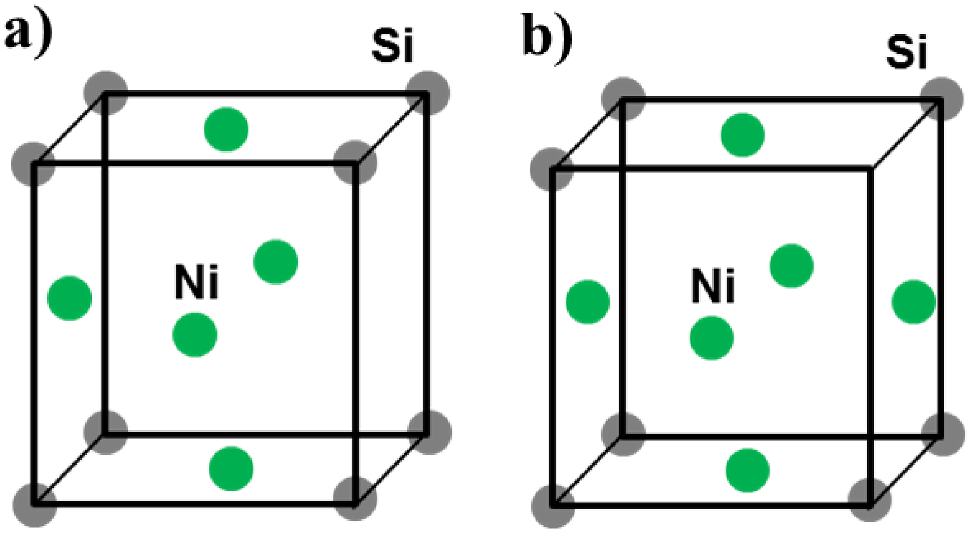

Fig. 5-4 Schematic of single a) Ni, b) Si vacancy defect configuration

The defect formation energy calculated after relaxing is listed in Table 5-3. The vacancy configurations are both maintained after relaxing in the two cases. Besides, the surrounding atoms near the vacancy are distorted after relaxing to compensate for the space left by the removed atom. The defect formation energy of Ni or Si vacancy is evidently larger than 0. This means both two configurations are not stable compared to the perfect γ' phase. The configuration of Si vacancy is especially not preferable as its defect formation energy is very large.

Table 5-3　Defect formation energy for single vacancy

Configuration before relaxing	$E_{f,d}$ (eV/atom)
Perfect lattice	0
Si vacancy	4.1661
Ni vacancy	1.7192

5.2.3　Substitutional defect

One substitutional defect means one atom in γ' phase lattice is replaced by another atom. Similar to single vacancy defect discussed above, there is only one substitutional position needs to be considered for either Si substitution or Ni substitution due to lattice symmetry, as shown in Fig. 5-5.

To produce single substitutional defect at Ni position in the constructed 32-atom superlattice, one Ni atom at ($0.25a_0$, $0.5a_0$, $0.25a_0$) position is replaced by another atom, Such as Si, Fe or Cr. Then the configuration is relaxed in VASP. For single substitutional defect at Si position, one Si atom at ($0.5a_0$, $0.5a_0$, $0.5a_0$) position is substituted.

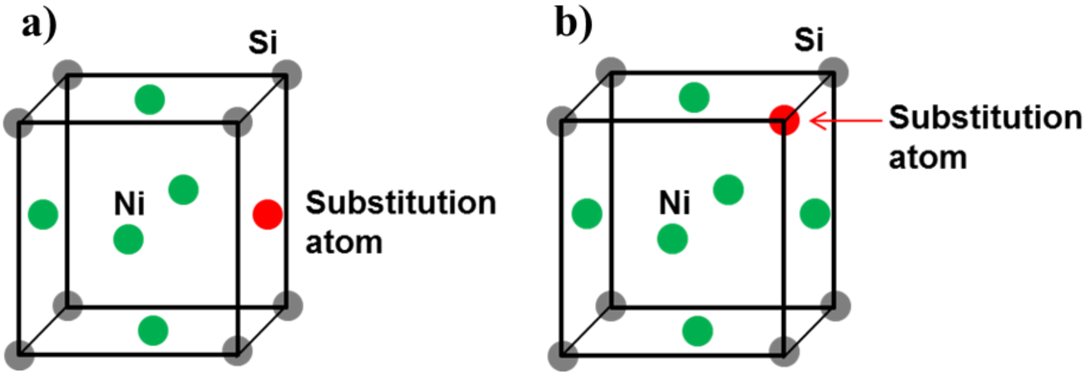

Fig. 5-5　Schematic of single substitutional defect at a) Ni, b) Si position

The calculated defect formation results of relaxed systems are listed in Table 5-4. This time, the relaxing process also doesn't introduce significant changes in atom configuration. The substitutional defect configurations are maintained, and only some minor distortion occurs near substitutional position. The defect formation energy of all types of substitutions calculated here are larger than 0, meaning that none of the configurations is thermodynamically favorable compared to the perfect γ' phase.

One thing to note is that the defect formation energy when Ni position is substituted is substantially lower than that when Si position is substituted. This is in consistency with the conclusion found in vacancy formation that Ni vacancy is more favorable than Si vacancy, as previously shown in Table 5-3. Especially, when Ni is substituted by Si atom, the defect formation energy $E_{f,\,d}$ is very close to 0. This means that although thermodynamically perfect γ' phase is still the most favorable configuration of all kinds, the configuration when Ni position is substituted by Si may also occur when the system is not reaching equilibrium.

Table 5-4 Defect formation energy for single substitution

Configuration before relaxing	$E_{f,\,d}$ (eV/atom)
Perfect lattice	0
Si substituted by Ni	2.7301
Ni substituted by Si	0.0580
Si substituted by Fe	3.1721
Ni substituted by Fe	0.7816
Si substituted by Cr	2.4611
Ni substituted by Cr	1.4513

5.2.4 Interstitial defect

Interstitial defect in the form of dumbbell is considered here. The position of dumbbell defect is still ($0.25a_0$, $0.5a_0$, $0.25a_0$) for Ni and ($0.5a_0$, $0.5a_0$, $0.5a_0$) for Si in the 32-atom superlattice. However, the dumbbells can have different orientation and spacing, therefore various possible configurations need to be selected here based on lattice symmetry.

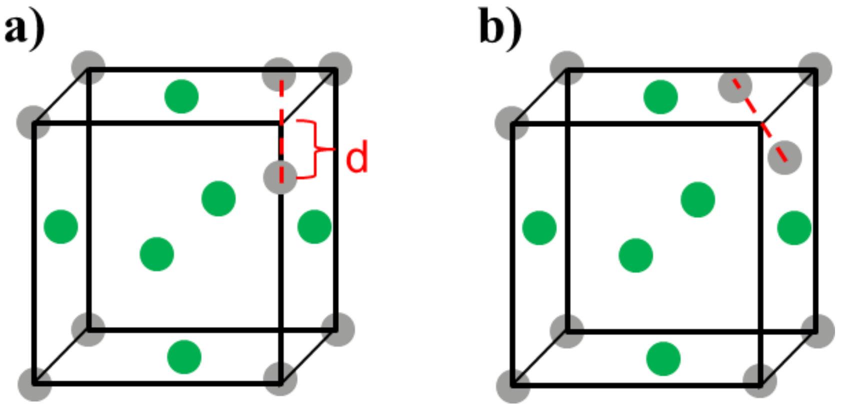

Fig. 5-6 Schematic of single interstitial defect at Si position with direction of a) <001>, b) <111>. The spacing of dumbbell is 2*d*.

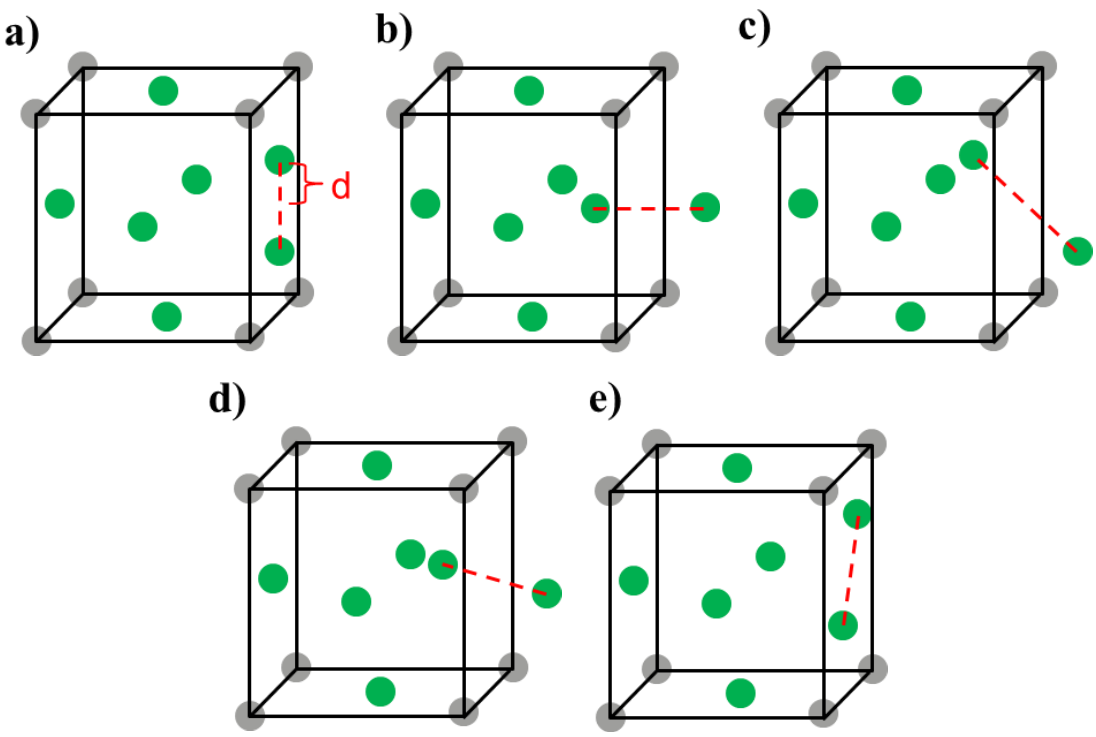

Fig. 5-7 Schematic of single interstitial defect at Ni position with direction of a) [100] or [001], b) [010], c) <111>, d) [110] or [011], e) [101]. The spacing of dumbbell is 2*d*.

For Si position, the dumbbell orientation is simple to analyze due to the high symmetry of the neighboring atoms. For dumbbell orientation at the Si position of ($0.5a_0$, $0.5a_0$, $0.5a_0$), the coordinate axis of ***x***, ***y*** and ***z*** are all equivalent. Thus, the possible orientations at Si position are illustrated in Fig. 5-6. The spacing between the two atoms in a dumbbell is marked as 2*d*. The orientation of <011> direction is excluded here, because when in <011> direction, the distance between Si in dumbbell and Ni at face center is much too small that such configuration cannot be stable.

Table 5-5 Defect formation energy for single interstitial

Configuration before relaxing	Before relax		After relax		$E_{f,d}$
	Direction	d/a_0	direction	d/a_0	(eV/atom)
Perfect lattice					0
Si dumbbell	<001>	1/4		~28.5%	3.1719
Si dumbbell	<001>	1/3		~28.5%	3.1732
Si dumbbell	<111>	√3/4		~16%√3	5.1403
Ni dumbbell	[100], [001]	1/4		~28.9%	3.6163
Ni dumbbell	[100], [001]	1/3		~28.9%	3.6159
Ni dumbbell	[010]	1/4		~27.4%	6.6566
Ni dumbbell	<111>	√3/4	[101]	~19%√2	4.9751
Ni dumbbell	[110], [011]	1/4	[100], [001]	~28.9%	3.6162
Ni dumbbell	[101]	1/4		~19%√2	4.9714

**d*: half of the spacing between the two atoms in a dumbbell.

**a_0: the lattice constant.

For Ni position, the symmetry is lower so that more configurations need to be taken into consideration. For dumbbell orientation at the Ni position of ($0.25a_0$, $0.5a_0$, $0.25a_0$), the coordinate axis of ***x*** and ***z*** are equivalent, while ***y*** axis is independent. Therefore, the five possible orientations of dumbbells are illustrated in Fig. 5-7.

Each possible orientation of dumbbells is calculated in VASP, with an assumed reasonable initial spacing for relaxing. After preferential dumbbell direction is discovered, initial dumbbell spacing is tuned to find out the proper distance between the two atoms of the dumbbell. The calculation results are listed in Table 5-5.

For Si dumbbell, the orientation of <001> is more preferable than <111>, as the defect formation energy is lower. Then calculation is performed at <001> orientation for two atom spacing, $d = a_0/4$ and $d = a_0/3$. After structure relaxing, both two initial conditions become the same configuration with d = ~28.5% a_0. Since $a_0/4 < 28.5\%a_0 < a_0/3$, this relaxed configuration with Si dumbbell in <001> direction and $d = 28.5\%a_0$ should be a preferential configuration, when speaking of the possible single Si dumbbell in γ' phase.

For Ni dumbbell at ($0.25a_0$, $0.5a_0$, $0.25a_0$), the orientation of [100] or [001] has the lowest defect formation energy. The atom spacing is also tuned by setting $d = a_0/4$ and $d = a_0/3$. Similarly, d = ~28.9% (a value between $a_0/4$ and $a_0/3$) is obtained after relaxing for both two initial conditions, indicating this is a preferential configuration.

One thing to note is that some Ni dumbbells changed their orientations after relaxing, as marked Table 5-5. The Ni dumbbell in [110] or [011] direction changed into [100] or [001] direction after relaxing, and both its spacing and defect formation energy are the same with that calculated in the [100] or [001] configuration. So is the case of <111> direction dumbbell, which changed into [101] direction after relaxing and has the same spacing and defect formation energy with that calculated in [101] configuration. Such results show that both <111> direction and [110] or [011] direction dumbbells are not stable. The results also put weights on the relative stability of [101] direction and [100] or [001] direction dumbbells.

5.3 Attempts on larger superlattice size

To reduce the lattice distortion caused by introduced single defect, a larger superlattice of 108 atoms would be preferred in VASP calculation [22]. Due to the limitation of calculation power, the accuracy of convergence and relaxation cannot be as high as that in the 32-atom superlattice. The parameters changed in 108-atom superlattice are:

IBRION=2. The conjugate-gradient algorithm is used during relaxing process. This method is less accurate than RMM-DIIS quasi-Newton algorithm.

ISIF=2. Stress tensor is no longer calculated in all process. This the default value of VASP code.

LREAL=AUTO. Projection operators are evaluated in real-space instead of reciprocal space. This accelerates calculation in large size supercell, but reduces some accuracy.

Table 5-6　Defect formation energy calculated in 32-atom superlattice and 108-atom superlattice

No.	Configuration before relaxing	$E_{f,d}$ (32 atoms) (eV/atom)	$E_{f,d}$ (108 atoms) (eV/atom)
1	Perfect lattice	0	0
2	Ni substituted by Si	0.0580	-0.6089
3	Ni substituted by Fe	0.7816	0.7433
4	Ni substituted by Cr	1.4513	0.9100
5	Ni vacancy	1.7192	2.0103
6	Si substituted by Cr	2.4611	2.3745
7	Si substituted by Ni	2.7301	2.8630
8	Si substituted by Fe	3.1721	3.2865
9	Si vacancy	4.1661	4.4079

The calculation results of 108-atom superlattice are listed in Table 5-6, and are compared with those calculated in the 32-atom supercell. The interstitial configurations are not calculated here, because they cause large lattice distortion, and the relaxing time is too long in the 108-atom supercell. Their formation energy in 108-atom supercell will be confirmed in the future.

As shown in Table 5-6, for most configurations, the defect formation energy does not change much when calculated in larger supercell. But for configuration No.2 and No.4, the defect formation energy substantially decreases when the supercell size is enlarged to contain 108 atoms.

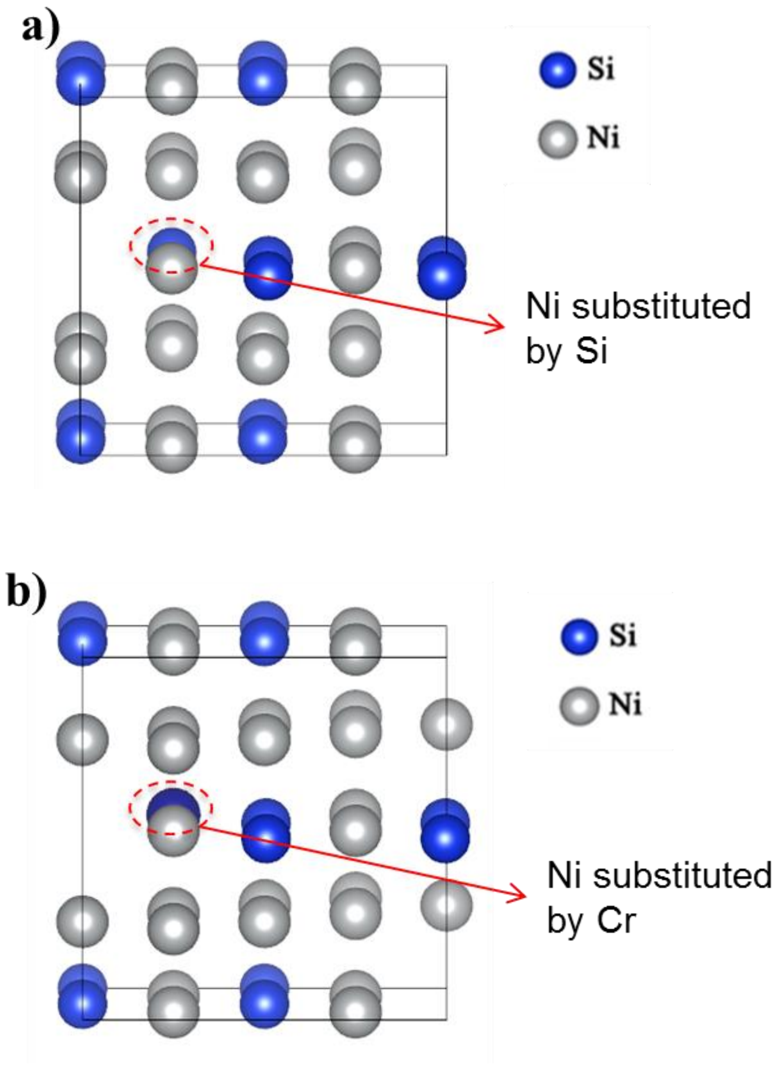

Fig. 5-8 Lattice distortion in 32-atom supercell after relaxing. a) one Ni atom is substituted by Si, b) one Ni atom is substituted by Cr.

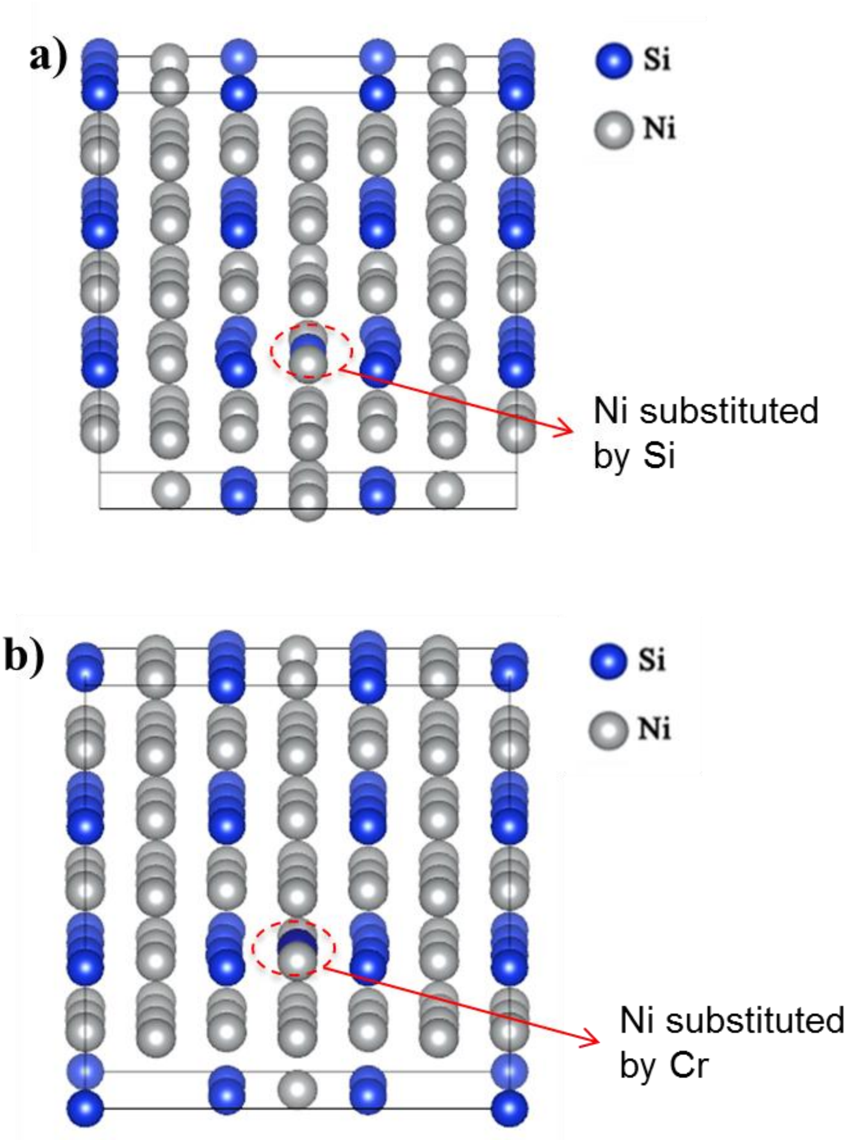

Fig. 5-9 Lattice distortion in 108-atom supercell after relaxing. a) one Ni atom is substituted by Si, b) one Ni atom is substituted by Cr.

By checking the lattice distortion after relaxing in all the configurations, it is found that only in configuration No.2 and No.4 that the distortion is evidently visible, as shown in Fig 5-8 and Fig. 5-9. In 32-atom supercell (Fig 5-8), the distortion in these two configurations is large, so that most of the atoms in the supercell is distorted more or less. But in 108-atom supercell, the distortion is quite well accommodated in the larger supercell, as shown in Fig. 5-8. It could be concluded that the larger supercell size reduces the extent of lattice distortion in configuration No.2 and No.4, and thus substantially reduces the calculated defect formation energy. In other configurations, the lattice distortion is not so evident; therefore the enlarged supercell size has less effect on the calculated defect formation energy.

Generally speaking, the order of formation energy is also almost the same between results calculated in 32-atom and 108-atom supercells. The only exception is confutation No.2, one Ni atom substituted by Si. When calculated in the 108-atom superlattice, this configuration has defect formation energy a little smaller than zero, which means it is even more preferable than the perfect γ’ phase.

5.4 Discussion

The results of defect formation energy calculated by VASP are summarized here. All the configurations of single defects have defect formation energy larger than 0, which means the perfect γ' phase lattice is thermodynamically the most stale and most preferable configuration.

Among these calculated configurations with single defect, the one in which Ni atom is substituted by Si has the lowest defect formation energy, which is very close to 0. This indicates that when allowed by kinetics, this defect configuration tends to occur. The defect formation energy of Ni atom substituted by Si is the second lowest. It is interesting to note that defect formation energy to remove or substitute a Ni atom is always evidently smaller than that of a Si atom, but this might also be affected by the selection of reference states in this work.

Single interstitial is also considered here, in the form of dumbbell. Si dumbbell tends to lie in the direction of <001>, with d = ~28.5%a_0; Ni dumbbell at (0.25a_0, 0.5a_0, 0.25a_0) tends to lie in the direction of [100] or [001], with d = ~28.9%a_0. However, the defect formation energies of these dumbbells are quite large compared with vacancies or substitutions, so they are actually not preferable.

Special attention needs to be paid on the accuracy of these calculation results. Due to the limitation in computing capacity, when relaxing in high accuracy, only a 32-atom superlattice could be constructed in this work. The accuracy is more or less sacrificed when larger supercell of 108 atoms is attempted. By comparing the calculated results and lattice distortion between the two calculation conditions, it is found that the lattice distortion is better accommodated in the 108-atom supercell, and the results of 108-atom supercell should have better reliability. Of course, large supercell with high relaxing accuracy is always desirable to improve the reliability of VASP modeling results. The results obtained here should better be quantitatively validated in even larger superlattice with high relaxing accuracy.

Previously in Section 4.2, the deviation of Ni/Si atom ratio has been experimentally observed by APT, especially in well-developed precipitates. These well-developed Ni-Si precipitates are previously regarded as the γ’ phase in literature [23, 24], but such deviation in stoichiometry put doubts on its exact crystal structure.

The VASP calculation results here are in consistency with the experiment results in Section 4.2, and provide a possible explanation for that. The configuration that Ni substituted by Si is calculated to be also a preferential configuration and its formation energy is very close to 0. This explains the reason why Ni/Si atom ratio is smaller than 3, and why in well-developed precipitates Ni+Si≈96at.%. Ni atom substituted by Si atom is a preferable configuration in γ’ phase precipitates, so the number of Ni atom reduces, and the summation of Ni and Si atom keeps constant in γ’ phase precipitates during irradiation. In some well-developed Ni-Si precipitates, the Ni concentration is lower than the line of Ni+Si≈96at.%, and the corresponding Fe concentration is high. This could be explained by the VASP calculation result that the configuration of Ni atom substituted by Fe atom is the third most preferential configuration of all.

Furthermore, the modeling results obtained from 32-atom and 108-atom supercell are both consistent with the experiment results in Section 4.2. The configuration when Ni is substituted by Si is more preferable than the perfect γ’ phase when calculated in 108-atom supercell. This indicates that the γ’ phase is not the most stable phase and there may be other Ni-Si phases with similar but smaller Ni/Si atom ratio that stably exist. It matches the previous modeling results of NiSi, Ni_3Si_2, Ni_2Si, $Ni_{31}Si_{12}$ which are calculated to have smaller phase formation energy than the γ’ phase [7]. Also, if the Ni-Si precipitates are a mixture of various Ni-Si phases, it explains why currently only a very small fraction of Ni-Si precipitates could be seen under TEM compared to that visible under APT. However, the formation energy below zero does not necessarily means that the Ni-Si precipitates formed in irradiated stainless steel should contain phases other than the γ’ phase, because there are two limitations in the current modeling work:

1) The selection of reference states may be not proper here. The total energy (TOTEN) calculated for the perfect γ’ phase and for the substitution configuration (Ni substituted by Si) are both -6.9438 eV/atom when calculated in 108-atom supercell. So the difference in defect formation energy comes from the way it is calculated, which involves the selection of reference states. In this work, the reference states of the Ni or Si atoms induced or removed from the γ’ phase supercell are their corresponding simple substance (fcc-Ni and diamond-Si). A more reliable method is to exchange atoms between precipitates and matrix. For example, a Ni atom is

extracted from the matrix, and then introduced into the γ’ phase to form interstitial.

2) The modeling work here only considers the stability of the precipitate itself. The interface free energy is not considered. Of course the interface between the austenite matrix and the Ni-Si precipitates should play an important role on the formation of Ni-Si precipitates. The γ’ phase is usually coherent with the matrix, which lower its interface free energy. Even if the other Ni-Si phases could be more preferable thermodynamically compared to the γ’ phase, but when calculated in austenite matrix, their interface free energy may be higher.

Due to the difficulty in simulating the complex austenite matrix, the matrix is currently not modelled in this work. Further modeling work on Ni-Si precipitates in matrix is needed to confirm the result here.

5.5 Summary

To explain the composition deviation in γ’ precipitates experimentally observed in Chapter 4, first principle calculation by VASP code is applied in this chapter. A supercell of perfect γ’ phase lattice is first constructed, and then different types of single defects are introduced. The supercell size of 32 atoms and 108 atoms are both attempted.

1) The phase formation energy of perfect γ’ phase is found to be $E_{f,p}$=-0.5421 eV/atom, with lattice constant of a = 0.3437nm. It matches previous modeling results in literature.
2) When one Ni atom is substituted by one Si atom, the defect formation energy is very close to zero, which means this configuration could also be preferable thermodynamically. When one Ni atom is substituted by Fe, the defect formation energy is the third lowest. This explains the reason why Ni/Si atom ratio is smaller than 3, and why in well-developed precipitates Ni+Si≈96at.%, which are experimentally observed in Chapter 4.
3) The results calculated in 32-atom supercell and in 108-atom supercell matches quite well. The enlarged supercell size reduced lattice distortion in some configurations, and thus decreases the calculated defect formation energy.

References in Chapter 5

[1] R. M. Martin, Electronic Structure: Basic Theory and Practical Methods, Cambridge University Press, 2004.

[2] L. Malerba, G. J. Ackland, C. S. Becquart, et al. Ab initio calculations and interatomic potentials for iron and iron alloys: Achievements within the Perfect Project. J Nucl Mater, 2010, 406 (1): 7-18.

[3] T. P. C. Klaver, D. J. Hepburn, G. J. Ackland. Defect and solute properties in dilute Fe-Cr-Ni austenitic alloys from first principles. Phys Rev B, 2012, 85 (17).

[4] G. Bonny, D. Terentyev, R. C. Pasianot, et al. Interatomic potential to study plasticity in stainless steels: the FeNiCr model alloy. Model Simul Mater Sc, 2011, 19 (8).

[5] A. Bakaev, D. Terentyev, X. He, et al. Energetics of radiation defects in Fe-based austenitic alloys: Atomic scale study. Nucl Instrum Meth B, 2013, 303: 33-36.

[6] G. Bonny, N. Castin, D. Terentyev. Interatomic potential for studying ageing under irradiation in stainless steels: the FeNiCr model alloy. Model Simul Mater Sc, 2013, 21 (8).

[7] D. Connetable, O. Thomas. First-principles study of nickel-silicides ordered phases. J Alloy Compd, 2011, 509 (6): 2639-2644.

[8] X. M. Yuan, L. J. Zhang, Y. Du, et al. A new approach to establish both stable and metastable phase equilibria for fcc ordered/disordered phase transition: application to the Al-Ni and Ni-Si systems. Mater Chem Phys, 2012, 135 (1): 94-105.

[9] Y. Cao, J. C. Zhu, Y. Liu, et al. First-principles studies of the structural, elastic, electronic and thermal properties of Ni3Si. Comp Mater Sci, 2013, 69: 40-45.

[10] Georg Kresse, Martijn Marsman, J. Furthmuller, Vienna Ab-initio Simulation Package the Guide, Vienna, 2013.

[11] Y. Udagawa, M. Yamaguchi, T. Tsuru, et al. Effect of Sn and Nb on generalized stacking fault energy surfaces in zirconium and gamma hydride habit planes. Philos Mag, 2011, 91 (12): 1665-1678.

[12] Y. Udagawa, M. Yamaguchi, H. Abe, et al. Ab initio study on plane defects in zirconium-hydrogen solid solution and zirconium hydride. Acta Mater, 2010, 58 (11): 3927-3938.

[13] M. Lindholm, B. Sundman. A thermodynamic evaluation of the nickel-silicon system. Metall Mater Trans A, 1996, 27 (10): 2897-2903.

[14] E. A. Brandes, G. B. Brook, C. J. Smithells, Smithells metals reference book, Butterworth-Heinemann, London, 1998.

[15] Y. Oya, T. Suzuki. The Nickel-Rich Portion of the Ni-Si Phase-Diagram. Z Metallkd, 1983, 74 (1): 21-24.

[16] M. A. Blanco, E. Francisco, V. Luana. GIBBS: isothermal-isobaric thermodynamics of solids from energy curves using a quasi-harmonic Debye model. Comput Phys Commun, 2004, 158 (1): 57-72.

[17] D. Iotova, N. Kioussis, S. P. Lim. Electronic structure and elastic properties of the Ni(3)X (X=Mn, Al, Ga, Si, Gel) intermetallics. Phys Rev B, 1996, 54 (20): 14413-14422.

[18] W. H. Lee, J. H. Lee, J. D. Bae, et al. Syntheses of Ni2Si, Ni5Si2, and NiSi by mechanical alloying. Scripta Mater, 2001, 44 (1): 97-103.

[19] S. V. Meschel, O. J. Kleppa. Standard enthalpies of formation of some 3d transition

metal silicides by high temperature direct synthesis calorimetry. J Alloy Compd, 1998, 267 (1-2): 128-135.

[20] T. Tokunaga, K. Nishio, H. Ohtani, et al. Thermodynamic assessment of the Ni-Si system by incorporating ab initio energetic calculations into the CALPHAD approach. Calphad, 2003, 27 (2): 161-168.

[21] L. Kaufman. Coupled Phase-Diagrams and Thermochemical Data for Transition-Metal Binary-Systems .4. Calphad, 1979, 3 (1): 45-76.

[22] M. J. Hackett, J. T. Busby, G. S. Was. The mechanism of Zr and Hf in reducing radiation-induced segregation in 316 stainless steel. Metall Mater Trans A, 2008, 39A (2): 218-224.

[23] T. Toyama, Y. Nozawa, W. Van Renterghem, et al. Irradiation-induced precipitates in a neutron irradiated 304 stainless steel studied by three-dimensional atom probe. J Nucl Mater, 2011, 418 (1-3): 62-68.

[24] R. Krummeich, P. Pareige, J. P. Massoud, et al. Solute cluster formation in austenitic and ferritic alloys under ion irradiation: a three-dimensional atom probe characterization. Surf Interface Anal, 2004, 36 (5-6): 575-580.

6. The Orowan hardening model in heavy ion irradiation

6.1 Nano-indentation methodology

The irradiation hardening is tested by nano-indentation. The nano-indentation is performed on the Shimadzu DUH-211 indentor, and the ISO-14577 standard is followed during the process [1]. A Berkovich pyramid-shape diamond indenter tip is used in this work.

A constant indentation depth of 200nm is kept for all samples. By literature, this indentation depth will represent the hardness from the sample top surface to roughly around 800~1000nm depth region [2-4], which is a proper value to reveal in irradiation hardening in this work. Fig. 6-1 shows a typical loading-unloading curve tested by nano-indentation. The sample is an unirradiated high Si sample. First, indenter tip touches the sample surface, and load is slowly added until the indentation depth reaches 200nm. Then, the force is kept for constant for 5 second. Finally, the load is slowly removed. The curve is quite smooth as shown in Fig. 6-1. The loading-unloading curves are checked for each indent, and some curves that do not follow this standard pattern are removed as bad data points. The bad data points could be caused by the scratches or dust on some parts of the sample surface, or by possible vibration in the testing room.

The nano-hardness is calculated by the maximum force, and the elastic modulus can be calculated by the slope of the unloading curve. Elastic modulus is not much affected by grain orientation or irradiation, and will decrease when the sample moves during indentation. Thus elastic modulus is a good indicator of the proper mounting of the sample for indentation. For stainless steel, a tested elastic modulus to be around 160GPa or above could be considered as satisfying.

At least 200 indents are indented for each sample, before irradiation and after irradiation. The distance between each two indents is kept at 30μm, which is much larger than literature value [5], to avoid possible interactions between their plastic zones. The 200 indents cover a region of 600×300 μm on the sample surface, which is large enough to cover more than 50 grains. Therefore, the tested nano-hardness is an average value of many grains with various orientations, to minimize the possible effects of grain orientation on tested hardness value [6]. This can be seen in Fig. 6-2. Fig. 6-2 is a superpose image of the inverse pole figure and the image quality figure scanned by EBSD. The scanned sample is a typical high Si sample. The inverse pole figure shows the grain size, while the image quality figure shows the array of nano-indents. The error bar of nano-hardness comes from the standard deviation of the 200 indent points.

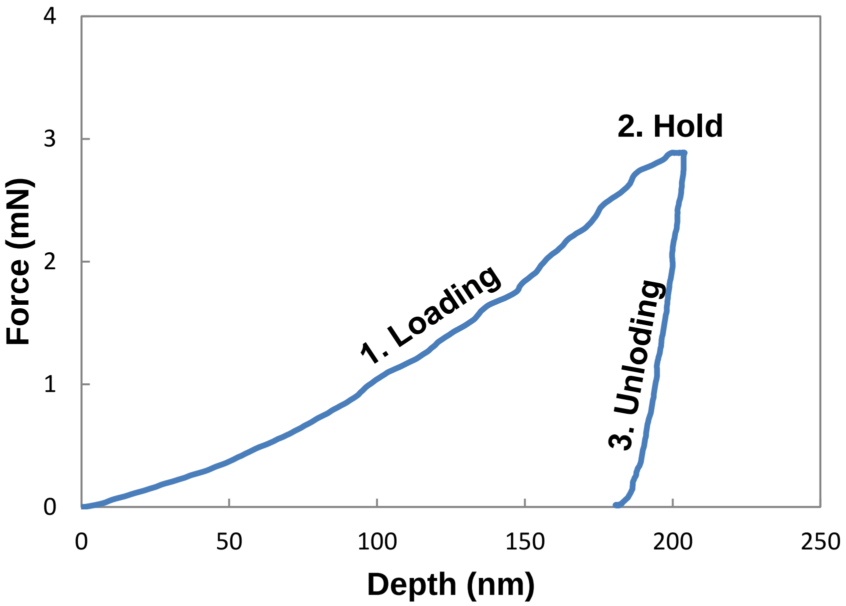

Fig. 6-1 A typical loading-unloading curve tested by nano-indentation. The sample is an unirradiated high Si sample.

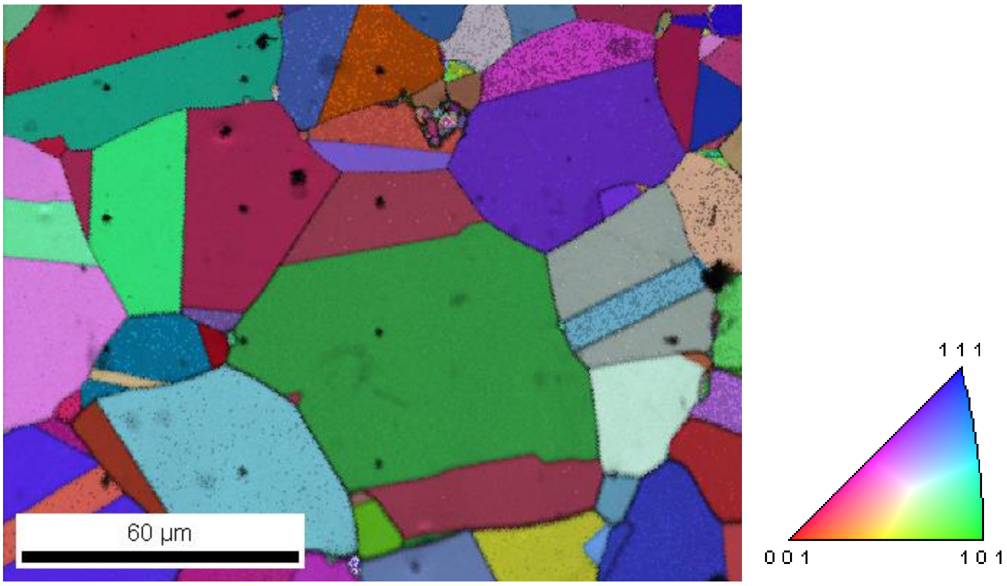

Fig. 6-2 A superpose image of the inverse pole figure and the image quality figure scanned by EBSD. The scanned sample is a typical high Si sample. The array of black dots is the nano-indents.

6.2 Irradiation hardening results

The nano-indentation results of unirradiated samples are shown in Fig. 6-3. In this study, each unirradiated sample prepared for irradiation is tested with 200 indents. This is because the nano-hardness of the same composition could be a little bit different among the samples prepared. Such differences could be caused by the sample surface condition, the ratio of indents on grain boundaries to indents in grain centers, and so on. For the same reason, the nano-indentation tests after irradiation are just performed in the region near the indent arrays tested before irradiation, to minimize the effects of such differences.

As shown in Fig. 6-3, the addition of Si generally increases the nano-hardness of the specimens, but the change is actually quite small. Si is a hardening alloying element in the high purity 316L stainless steel model alloy. And when the composition is fixed, the hardness difference between each unirradiated sample is very small, which proves the reliability of the nano-hardness test in this study.

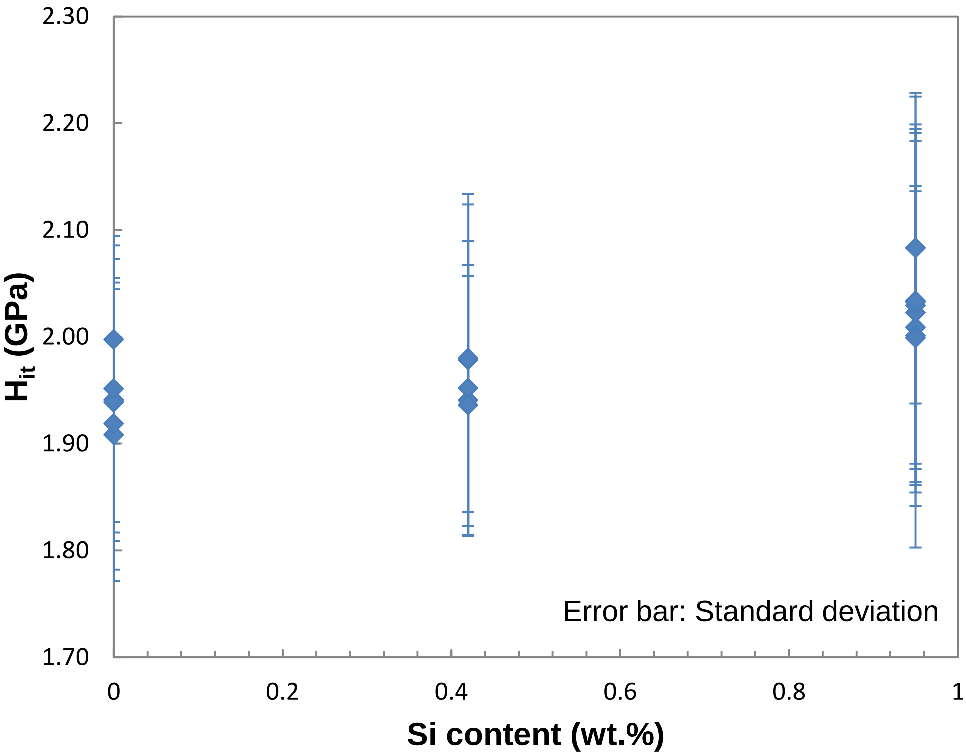

Fig. 6-3 Nano-indentation results of unirradiated samples. Each blue mark represents the average value of 200 indents tested on one prepared sample

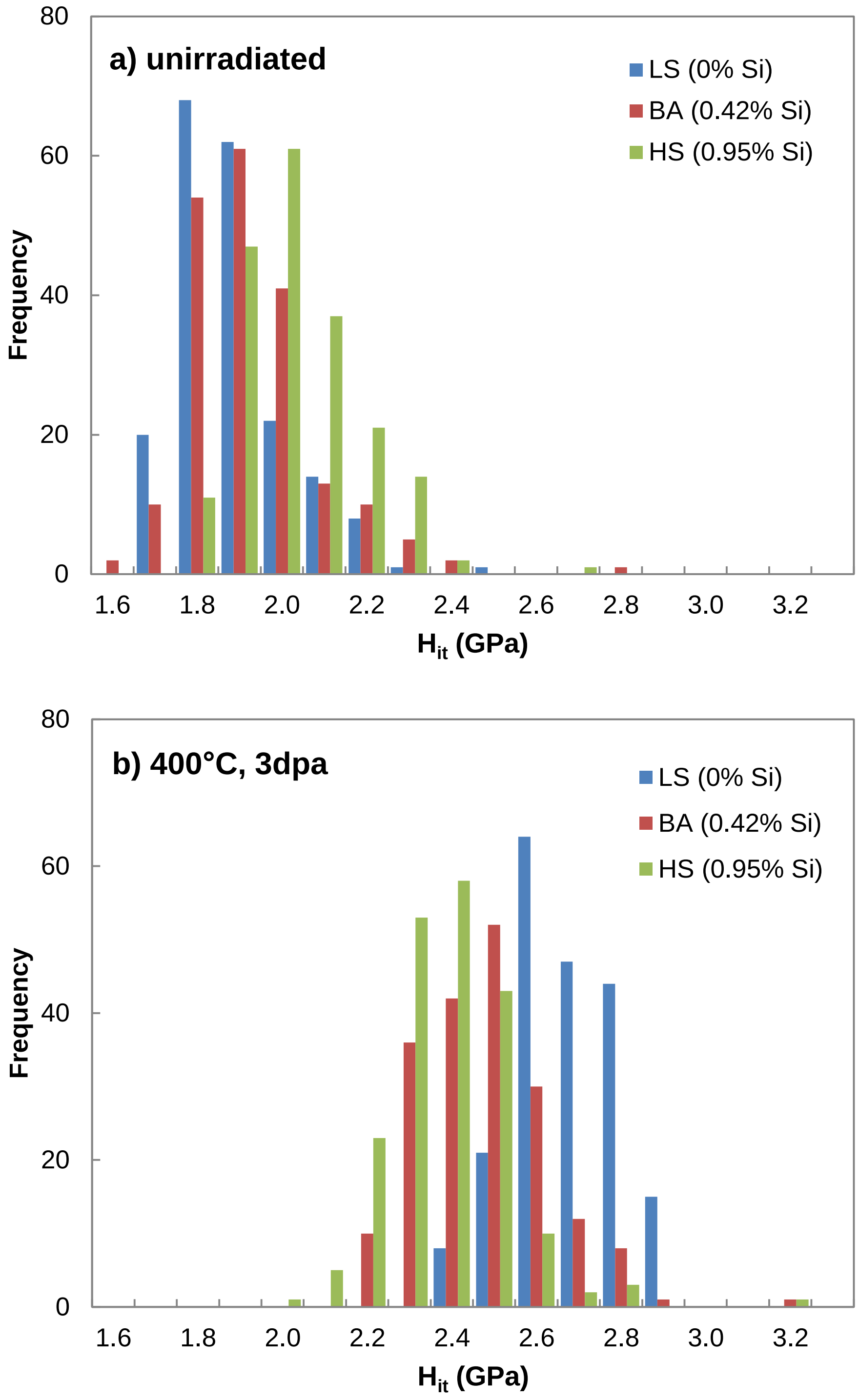

Fig. 6-4 Histogram of indentation result distribution a) before irradiation and b) after 400°C and 3dpa irradiation. 200 indents are performed for each sample before or after irradiation.

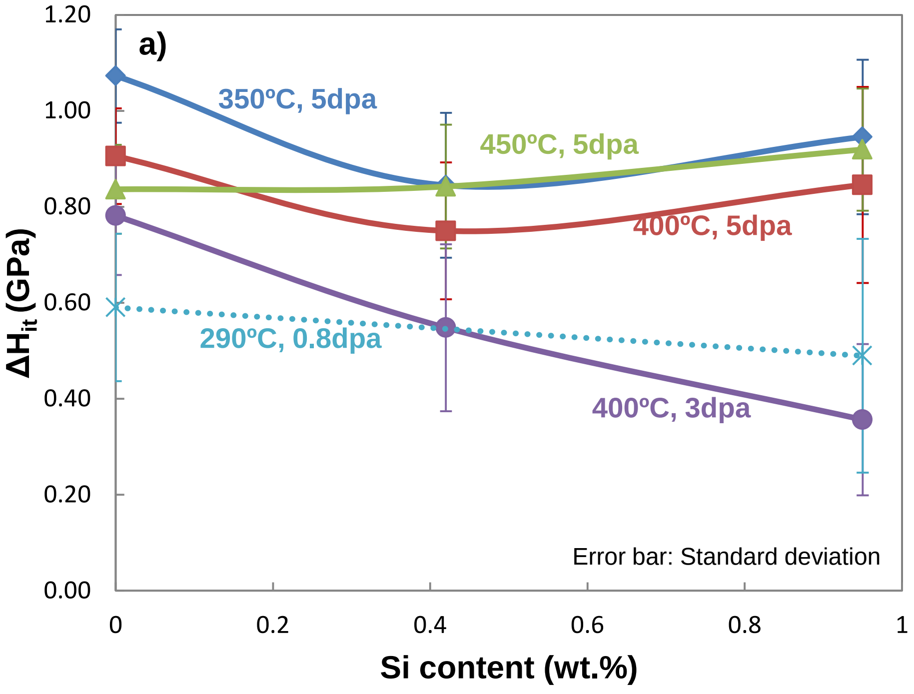

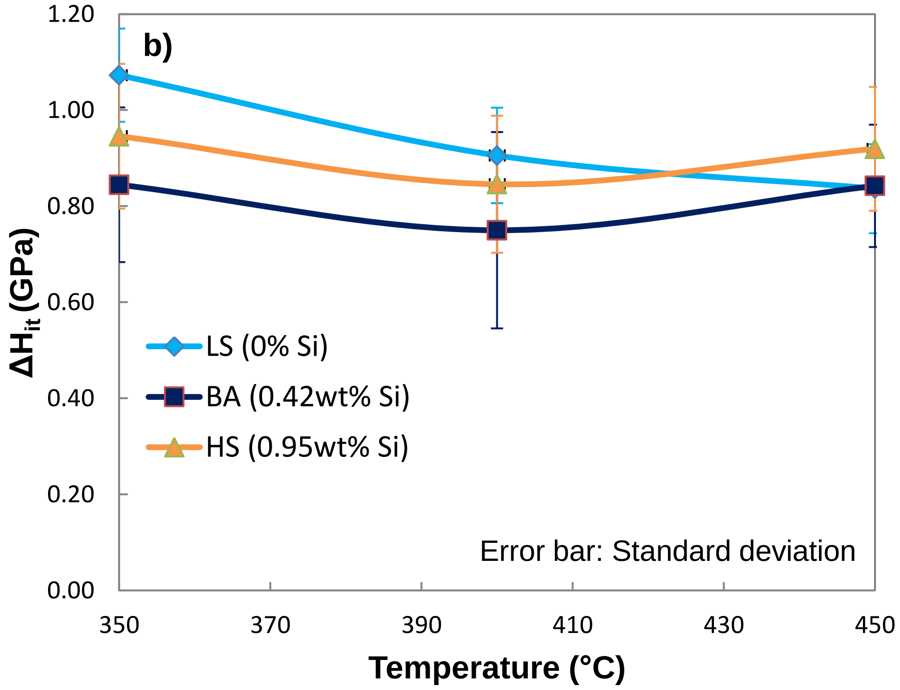

Fig. 6-4 Irradiation hardening results tested by nano-indentation. a) All hardening results are plotted against Si content; b) The hardening results of 5dpa irradiation are plotted against irradiation temperature.

To further confirm the hardness test reliability, the histogram of indentation result distribution before and after irradiation is drawn. Fig. 6-4 shows such a typical histogram before and after irradiation for the three samples. Only few irregular data points are found, and the shape of data distribution for each sample is reasonable.

All the nano-indentation results of irradiation hardening are plotted against Si content in Fig. 6-4 (a). For samples irradiated at 290ºC to ~0.8dpa, the addition of Si does not show evident effects on irradiation hardening. Or to be more precise, the hardening of high Si sample seems a little bit smaller than that of low Si sample. But since the error bar is large in nano-indentation results, such difference is still within the error range. This is exactly in consistency with the microstructure observation results discussed in Section 3.2. It further confirms that black dots are the main contributor to irradiation hardening here.

When samples are irradiated at higher temperature of 400ºC to 3dpa, the effects of Si addition becomes evident. The irradiation hardening monotonically decreases as Si content increases. As analyzed in Section 3.3, this is due to the suppressed Frank loop number density and average size at all the depths by Si addition. When irradiated to 5dpa at the same temperature, the irradiation hardening further increases for all the three compositions. However, the hardening of high Si sample turns out to be larger than that of base Si sample, which indicates the formation of Ni-Si formation in high Si sample at 5dpa. It shows that besides irradiation temperature, dose is also a key parameter in precipitation. There seems to be a threshold dpa value above which Ni-Si precipitates begin to form in large density.

The irradiation hardening of high Si sample is larger than that of base Si sample when samples are irradiated at 350, 400 and 450ºC to 5dpa. However, their causes are not exactly the same. At 450ºC, the unfaulting of Frank loops is evident in low Si sample, but Si addition retards the unfaulting process, as previously discussed in Section 3.4. Therefore, the larger irradiation hardening of high Si sample irradiated at 450ºC comes not only from the formation of Ni-Si precipitates, but from the suppressed Frank loop unfaulting as well. For low Si samples which are irradiated at 350 and 400ºC to 5dpa, the irradiation temperature is low and the loop unfaulting is not evident, as described in Section 3.4. The high Si and base Si samples irradiated at these two conditions have not been examined by TEM yet. But based on the knowledge of Si effects learned from 400ºC, 3dpa irradiation and 450ºC, 5dpa irradiation, it is likely that evident unfaulting process will also not be observed in samples with Si addition. Therefore, at 350 and 400ºC, the larger irradiation hardening of high Si sample probably comes from Ni-Si precipitation mainly. But this assumption needs further microstructure examination to confirm.

The hardening results of 5dpa irradiation in Fig. 6-4(a) are re-plotted against irradiation temperature in Fig. 6-4(b). In this way, the effects of irradiation temperature are shown clearer.

In irradiated low Si sample, no Ni-Si precipitates could be formed. So the irradiation hardening comes from the Frank loops. When specking of dislocation loops only, it is natural that higher irradiation temperature results in smaller extent of hardening, because higher temperature causes lower density of Frank loops and enhanced Frank loop unfaulting. Perfect loops are glissile, and are supposed not to contribute to irradiation hardening.

For samples containing Si, the trend is similar when irradiation temperature is increased from 350°C to 400°C. The hardening decreases, but the amount of decrease is a little bit smaller compared to that of low Si sample. But when irradiation temperature is further increased to 450°C, the irradiation hardening increases for both base Si and high Si samples. This should be attributed to the formation of Ni-Si precipitates, which are already confirmed in Section 4.2.

It is interesting to note that the curves of base Si and high Si samples look very similar in shape. It seems that the temperature effects on samples without Si (low Si) follow one trend, and the temperature effects on samples with Si (base Si and high Si) follow another trend. The amount of Si added into model alloys changes the absolute value of irradiation hardening, but does not change the relative temperature effects on the irradiated samples. Note that the irradiation hardening here is both influenced by Frank loops and Ni-Si precipitates. So perhaps as irradiation temperature increases, the change in irradiation hardening contributed by Ni-Si precipitation is the same in base Si and high Si sample. Or perhaps the similar curve shape is just a coincidence. The change in Ni-Si precipitation is actually different in base Si and high Si sample, but such difference is just compensated by the different changes in Frank loops.

As we know, the hardness change caused by irradiation is an indicator of the overall microstructure evolution during irradiation. The hardening results here match the observed microstructure results in the previous chapters, so this further confirms the experiment reliability in the current study.

The results of nano-hardness test are largely depending on the parameters used, especially the indentation depth. It is also very sensitive to the irradiation condition and the surface condition of the samples prepared. Therefore, a direct comparison in absolute value between the literature data and the data in this work is difficult to perform.

K. Fukuya found that the amount of increase in yield strength caused by neutron irradiation at 300°C is substantially suppressed by the addition of 0.92% Si [7]. But in this study, such Si effects are evident when irradiation temperature is higher. This may well be due to the difference in dose rate between heavy ion irradiation and neutron irradiation. The difference in dose rate can cause irradiation temperature shift phenomenon, which is described in detail in the textbook written by G. Was (Section 8.3.5) [8]. Generally speaking, the microstructure of irradiation at lower dose rate and lower temperature could be similar to that irradiated at higher dose rate and higher temperature, when considering the number of defects lost to sinks per unit volume is kept constant. The phenomenon has also been quantitatively verified [9].

The literature data of irradiation hardening tested by Vickers hardness is summarized. The irradiation conditions that are similar to the conditions used in this work are listed in Table 6-1 for comparison. The Vickers hardness (H_v) is converted to nano-harness (H_{it}) by a factor of 0.76 [4]. The scattering in literature data is quite large, but generally speaking, most of the literature data are larger in value than the hardness data tested in this work. One reason is that the difference between nano-indentation and Vickers hardness test could be large, and 0.76 is only a rough convertor. The second reason is that in literature, the irradiation is either neutron or proton, both of which produce homogenous radiation damage in the tested region. The irradiation particle in this study is heavy ion, which produces high dpa damage at deep regions. However, compared with the surface region, the deep region contributes less to the irradiation hardening measured by nano-indentation. The effects of such defect distribution are discussed in the following section.

Table 6-1 Literature data of irradiation hardening by Vickers hardness.

Ref	Stainless steel	Irradiation particle	Temperature (°C)	Dose (dpa)	ΔHv (kg/mm^2)	ΔH_{it} (GPa)
[10, 11]	CP304	Proton	360	5	176	2.27
	Model alloys	Proton	360	5	164~193	2.11~2.48
[12]	CP304	Proton	360	5	190	2.45
	CP316	Proton	360	5	174	2.24
[13]	HP316	Proton	400	5	179	2.31
	HP 316+0.3%Pt	Proton	400	5	112	1.44
	HP 316+0.3%Hf	Proton	400	5	63	0.81
[14]	304	Neutron	275	~1	110~129	1.42~1.66
	316	Neutron	275	~1	58~146	0.75~1.88
[15]	316	Neutron	365	6	176	2.27
[16]	316L	Proton	400	7	237	3.06
	316L	Proton	500	7	126	1.62
[17]	316L	Proton	400	4	129	1.66
	316L	Proton	400	7	163	2.10
	316L	Proton	500	7	121	1.56

6.3 The Orowan model with defect depth distribution

In neutron irradiation, irradiation hardening could be connected to microstructure by simply applying the average values of loop number density and size to the classic Orowan model [18, 19]. But in heavy ion irradiation, the inhomogeneous defect distribution brings difficulty on the interpretation of hardening results [20, 21]. With our relrod observation results of Frank loop depth distribution, attempts are made here to apply the Orowan model to heavy ion irradiation by finding a proper method to average the loop density and size in the plastic zone of nano-indentation. In this section, the samples irradiated at 400°C to 3dpa is taken as an example of such attempts, because in this irradiation condition, the major type of radiation defects is only Frank loops.

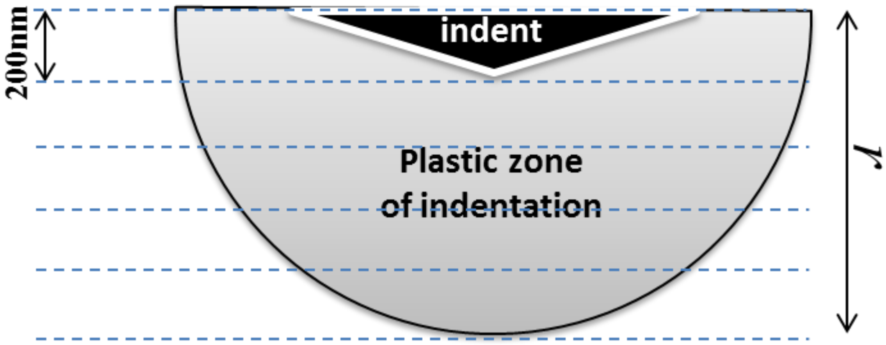

Fig. 6-5 A schematic of the plastic zone of nano-indentation

For simplicity, the plastic zone is assumed to be semi-sphere in shape [22] with radius of *r*, as shown in Fig. 6-5. And *r* also means the maximum depth of the plastic zone. For our indentation at a constant depth of 200nm, *r* is supposed to be in the range of 800~1000nm. Here, two conditions, *r*=800nm and *r*=1000nm, are both attempted. The plastic zone is divided into four or five regions at intervals of 200nm depth, which is the same way of what we did in Frank loop observation. Then the Orowan equation (Equation 1-1 and 1-2) could be rewritten like this:

$$\Delta\sigma_l = \alpha_l M \mu b \Big(\sum_h \frac{V_h}{V} N_{l,h} d_{l,h}\Big)^{1/2}$$

Where $\Delta\sigma_l$ is the change in yield strength caused by Frank loop formation (the only hardening contributor considered here);

M is the Taylor factor (3.06) [18];

μ is the shear modulus (76GPa) [18];

b is the Burgers vector (0.255nm) [18];

V is the total volume of the semi-spherical plastic zone;

V_h is the volume of one divided region of the plastic zone at the depth of h;

$N_{l,h}$ and $d_{l,h}$ are the number density and the average size of Frank loops in this divided region at the depth of h.

Here $\Delta\sigma_l$ is calculated from Vickers hardness change [23], and Vickers hardness change is converted from the nano-hardness change tested in experiment by a factor of 0.76 [4]. $N_{l,h} \times d_{l,h}$ has the physical meaning of the Frank loop total length in one unit volume, therefore $N_{l,h} \times d_{l,h}$ is first calculated in each divided region, and then is averaged with a weighting factor of V_h/V. The region of 0~200nm depth is neglected in calculation due to its very low loop density and the interference of the extra FIB damage.

The calculated hardening coefficient α_l is listed in Table 6-2. Previous research on neutron irradiation shows α_l to be in the range of 0.30~0.45 for Frank loops [19, 24, 25]. Here when r=1000nm, α is around 0.30 for all the three samples, which meets the lower limit of previous literature data. When r=800nm, the hardening coefficient for high Si sample reaches 0.48, much higher than that of the other two samples. This should be caused by the fact that the Frank loop density in 200~600nm depth region for high Si sample is extremely low, as previously discussed in Section 3.3. The maximum depth r should be larger than 800nm to include more loops at deeper regions to explain for the amount of irradiation hardening tested.

Table 6-2 Calculation of the irradiation hardening coefficient in the Orowan model. The irradiation is performed at 400°C to 3dpa.

	Si wt.%	ΔH_{it} GPa	$\Delta\sigma_l$ GPa	α_l (r=800nm)	α_l (r=1000nm)
LS	~0	0.78	0.18	0.34	0.30
BA	0.42	0.55	0.13	0.30	0.27
HS	0.95	0.36	0.084	0.48	0.32

6.4 Summary

In this chapter, nano-indentation tests are performed on samples before and after irradiation:

1) At 290°C and ~0.8dpa, Si addition does not change irradiation hardening; At 400°C and 3dpa, Si addition significantly reduces hardening. These hardening results well match the microstructure observation results, which further confirms the experiment reliability.
2) When irradiated at 350~450°C to 5dpa, the hardening of high Si (0.95wt.%) sample is larger than that of base Si (0.42wt.%), which indicates the formation of Ni-Si precipitates. At 450°C, the larger hardening value of high Si sample not only comes from the denser Ni-Si precipitate formation, but also comes from the Si’s role in retarding Frank loop unfaulting.
3) The Orowan model can also be applied in heavy ion irradiation by averaging the inhomogeneous loop density and size in a semi-spherical plastic zone. A hardening coefficient of around 0.30 is obtained for all the three samples irradiated at 400°C to 3dpa by assuming the maximum depth of the plastic zone to be five times of the indentation depth. This hardening coefficient value meets the lower limit of previous literature data.

References in Chapter 6

[1] ISO 14577, Metallic materials - Instrumented indentation test for hardness and materials parameters. 2002.

[2] D. Kiener, A. M. Minor, O. Anderoglu, et al. Application of small-scale testing for investigation of ion-beam-irradiated materials. J Mater Res, 2012, 27 (21): 2724-2736.

[3] M. Ando, E. Wakai, T. Sawai, et al. Synergistic effect of displacement damage and helium atoms on radiation hardening in F82H at TIARA facility. J Nucl Mater, 2004, 329: 1137-1141.

[4] K. Yabuuchi, Y. Kuribayashi, S. Nogami, et al. Evaluation of irradiation hardening of proton irradiated stainless steels by nanoindentation. J Nucl Mater, 2014, 446 (1-3): 142-147.

[5] A. Lupinacci, K. Chen, Y. Li, et al. Characterization of ion beam irradiated 304 stainless steel utilizing nanoindentation and Laue microdiffraction. J Nucl Mater, 2015, 458: 70-76.

[6] T. Miura, K. Fujii, K. Fukuya, et al. Influence of crystal orientation on hardness and nanoindentation deformation in ion-irradiated stainless steels. J Nucl Mater, 2011, 417 (1-3): 984-987.

[7] K. Fukuya, S. Shima, H. Kayano, et al. Stress-Corrosion Cracking and Intergranular Corrosion of Neutron-Irradiated Austenitic Stainless-Steels. J Nucl Mater, 1992, 191: 1007-1011.

[8] G. S. Was, Fundamentals of Radiation Materials Science: Metals and Alloys, Springer, 2007.

[9] G. S. Was, J. T. Busby, T. Allen, et al. Emulation of neutron irradiation effects with protons: validation of principle. J Nucl Mater, 2002, 300 (2-3): 198-216.

[10] Z. Jiao, G. S. Was. The role of irradiated microstructure in the localized deformation of austenitic stainless steels. J Nucl Mater, 2010, 407 (1): 34-43.

[11] Z. Jiao, G. S. Was. Impact of localized deformation on IASCC in austenitic stainless steels. J Nucl Mater, 2011, 408 (3): 246-256.

[12] J. Gan, G. S. Was. Microstructure evolution in austenitic Fe-Cr-Ni alloys irradiated with protons: comparison with neutron-irradiated microstructures. J Nucl Mater, 2001, 297 (2): 161-175.

[13] L. Fournier, B. H. Sencer, G. S. Was, et al. The influence of oversized solute additions on radiation-induced changes and post-irradiation intergranular stress corrosion cracking behavior in high-purity 316 stainless steels. J Nucl Mater, 2003, 321 (2-3): 192-209.

[14] D. J. Edwards, E. P. Simonen, S. M. Bruemmer. Evolution of fine-scale defects in stainless steels neutron-irradiated at 275 degrees C. J Nucl Mater, 2003, 317 (1): 13-31.

[15] M. N. Gusev, O. P. Maksimkin, O. V. Tivanova, et al. Correlation of yield stress and microhardness in 08Cr16Ni11Mo3 stainless steel irradiated to high dose in the BN-350 fast reactor. J Nucl Mater, 2006, 359 (3): 258-262.

[16] S. Teysseyre, Z. Jiao, E. West, et al. Effect of irradiation on stress corrosion cracking in supercritical water. J Nucl Mater, 2007, 371 (1-3): 107-117.

[17] R. S. Zhou, E. A. West, Z. J. Jiao, et al. Irradiation-assisted stress corrosion cracking of austenitic alloys in supercritical water. J Nucl Mater, 2009, 395 (1-3):

11-22.
[18] K. Fukuya, K. Fujii, H. Nishioka, et al. Evolution of microstructure and microchemistry in cold-worked 316 stainless steels under PWR irradiation. J Nucl Sci Technol, 2006, 43 (2): 159-173.
[19] G. E. Lucas. The Evolution of Mechanical Property Change in Irradiated Austenitic Stainless-Steels. J Nucl Mater, 1993, 206 (2-3): 287-305.
[20] N. Sekimura, T. Kamada, Y. Wakasugi, et al. Evaluation of radiation hardening in Fe alloys under heavy ion irradiation by micro-indentation technique. J Nucl Mater, 2002, 307: 308-311.
[21] R. Kasada, S. Konishi, K. Yabuuchi, et al. Depth-dependent nanoindentation hardness of reduced-activation ferritic steels after MeV Fe-ion irradiation. Fusion Eng Des, 2014, 89 (7-8): 1637-1641.
[22] P. Hosemann, D. Kiener, Y. Q. Wang, et al. Issues to consider using nano indentation on shallow ion beam irradiated materials. J Nucl Mater, 2012, 425 (1-3): 136-139.
[23] J. T. Busby, M. C. Hash, G. S. Was. The relationship between hardness and yield stress in irradiated austenitic and ferritic steels. J Nucl Mater, 2005, 336 (2-3): 267-278.
[24] M. L. Grossbeck, P. J. Maziasz, A. F. Rowcliffe. Modeling of Strengthening Mechanisms in Irradiated Fusion-Reactor 1st Wall Alloys. J Nucl Mater, 1992, 191: 808-812.
[25] K. V. Tsay, O. P. Maksimkin, L. G. Turubarova, et al. Microstructural defect evolution in neutron - Irradiated 12Cr18Ni9Ti stainless steel during subsequent isochronous annealing. J Nucl Mater, 2013, 439 (1-3): 148-158.

7. Concluding remarks

7.1 Principal conclusions

The ageing management of stainless steel components in light water reactors is an important issue. Currently, the Japan and U.S. ageing management standards mainly rely on the databases of mechanical cracking to evaluate the condition of stainless steel components. However, continuous efforts should also be made to trace back to the microstructure evolution process, which is the origin of such mechanical degradation.

The main objective of this research is to improve the knowledge base of radiation defect formation in stainless steel, to try to bridge the mismatch between actual component working conditions and database values, and to reduce the uncertainties in safety standards introduced by possible unknown factors. The formation of black dots and Frank loops is isolated by controlling irradiation condition, and their formation mechanisms are discussed by tuning the Si content. By raising irradiation temperature to 450°C and dose to 5dpa, γ’ precipitates are introduced. The formation mechanisms of γ’ precipitates are analyzed by combining near-atomic scale three dimensional atom maps with first principle calculation. The possible relationship between the formation of precipitates and dislocation loops are discussed. Additionally, attempts are made to quantitatively correlate these microscopic defects with macroscopic hardening in heavy ion irradiation by utilizing the heterogeneous defect depth distribution observed.

The principal results of this study are:

1) The formation of black dot is not much influenced by Si in irradiation at 290ºC. However, Frank loops are distinctively suppressed by Si addition at 400ºC in both density and size, especially in the near-surface region. This could be explained by Si’s role in enhancing the effective diffusivity of vacancies and thus promoting recombination. It could also be explained if the Si addition can promote the trapping of interstitials by surface sink. For low Si samples, the unfaulting of Frank loops is not evident until the irradiation temperature is raised to 450ºC.

2) When irradiated at 290ºC to ~0.8dpa, the addition of Si enhances Ni segregation. And Ni tends to enrich near positions of Si enrichment in high Si sample, which may be the precursor of Ni-Si precipitates.

3) Ni-Si precipitates are formed in both base Si (0.42wt.%) and high Si (0.95wt.%)

samples irradiated at 450ºC to 5dpa. In well-developed Ni-Si precipitates, Ni/Si atom ratio is found to be smaller than 3 while maintaining Ni+Si≈96at.% by atom probe tomography. It could be explained by VASP calculation that when one Ni atom is replaced by Si, the configuration is still preferable as its defect formation energy is very close to zero. Mo and Mn are fully depleted at an early stage of precipitate formation.

4) Some Ni-Si precipitates are found to be of ring shape. And base on the shape, size and orientation, they should have formed on dislocation loops. Si addition retards loop unfaulting, possibly via suppressing Frank loop size or stabilizing Frank loops by precipitation.

5) The irradiation hardening tested by nano-indentation matches the microstructure observed in this work. The Orowan model can also be applied in heavy ion irradiation by averaging the inhomogeneous loop density and size in a semi-spherical plastic zone. A hardening coefficient of around 0.30 is obtained for all the three samples irradiated at 400°C to 3dpa by assuming the maximum depth of the plastic zone to be five times of the indentation depth. This hardening coefficient value meets the lower limit of previous literature data.

The present study is a fundamental research on stainless steel degradation behavior under irradiation. The results improve the understanding of stainless steel degradation, and contribute to the ageing management and nuclear safety in the following aspects:

1) The existence of dense Ni-Si precipitates in irradiated stainless steel is confirmed, so they should not be ignored when considering stainless steel degradation and cracking. The Ni-Si precipitates are found to be not exactly the γ’ phase, and are observed to have interactions with dislocation loops, so the importance of further studies on Ni-Si precipitates is emphasized.
2) The effects of alloying element Si in irradiated stainless steel are further clarified. It provides references for future design of stainless steels that could be applied in nuclear power plants.
3) The differences between heavy ion irradiation and neutron irradiation in defect depth distribution are discussed, and the Orowan model for neutron irradiation

hardening is modified to fit the case of heavy ion irradiation. Such efforts improve the reliability of using the heavy ion irradiation tool to emulate neutron damage. A better understanding of the heavy ion irradiation tool could save time and money for future studies and databases.

7.2 Perspectives

The microstructure evolution in irradiated stainless steel is a complex process, therefore continuous research efforts are needed to clarify it. The present study attempted several typical irradiation conditions and three typical model alloy compositions, but of course much more works are needed to construct a complete understanding. Some interesting results in the present study may inspire some new research topics for future study. The author lists some here:

1) The role of Ni-Si precipitates during stainless steel deformation needs to be reconsidered. Previously, the role of precipitates is described by the Orowan model, because with the Orowan model, the irradiation hardening can be fitted by the number density and size of the γ' precipitates observed under TEM. But in the current study, the stoichiometry of observed Ni-Si precipitates is proved to be quite different from that of standard γ' phase. Also the number density of Ni-Si precipitates has been proved by other researchers to be much higher that observed under TEM. Therefore, the way these Ni-Si precipitates contribute to irradiation hardening could be different from previous expectation.

2) The nature of experimentally observed Ni-Si precipitates needs to be further discussed by modeling. The VASP calculation results obtained in this work are interesting, but not satisfactory enough since the austenite matrix is not considered in this work. To improve the reliability, the matrix also needs be simulated by first principle calculation. In this way, the nature of Ni-Si precipitates, including the existence of other Ni-Si phases and the possibility of defect formation could be thoroughly discussed. It can also provide basis for further molecular dynamics modeling.

3) One-dimensional diffusion model could be attempted to explain the depth distribution of Frank loops experimentally observed by TEM in this study, and to explain the Ni and Si segregation near sinks quantitatively observed by APT when model alloys are irradiated at 290°C.

4) More works on the interactions between Ni-Si precipitates and dislocation loops are

needed. The main focus should be the number fraction of Ni-Si precipitates formed on loops, and how loops decorated by Ni-Si precipitates behave during deformation. Due to observation limitations, the experiment needs to be smartly designed. Molecular dynamics modeling should also be utilized to help reveal its inner mechanisms.

Acknowledgements

I would first express my thanks to my supervisor, Prof. Naoto Sekimura. I would like to thank his helpful advices one my research and his inspiring encouragement during my three years here. I clearly remember when I entered this laboratory three years ago I was a student with material science background and limited knowledge on nuclear engineering. It is my supervisor who has guided me into the field of nuclear safety and encouraged me to go further and further and in this field.

I would also like to thank assist professor Kenta Murakami. I benefit a lot from his training on facilities and his advices on my research work. He is really a warm-hearted person who is always ready to solve other people’s problems. I also want to thank Prof. Tatsuya Itoi for his helpful suggestions on my research topic.

I’m also grateful to Dr. Naoki Soneda, Dr. Kenji Dohi and Mr. Kenji Nishida in Central Research Institute of Electric Power Industry. Their experiences helped me a lot to find out an interesting, important and practical topic for my PhD thesis. They gave helpful advices on my results and opinions. I would like to thank Dr. Kenji Dohi for his help in improving my TEM observation skills, and would like to thank Mr. Kenji Nishida for his help to improve my understanding of atom probe technique. And this thesis dissertation much benefited from Dr. Soneda’s detailed and helpful advices.

And I would like to thank Mr. Omata and Mr. Morita in Tokai-mura campus for their help in operating the heavy ion irradiation facility. I learnt a lot from their engineering experiences.

I would like to thank Prof. Zhengcao Li in Tsinghua University, who is the supervisor of my master thesis. It is fortunate for me that we could keep in contact in my PhD candidate period. I’m grateful to his advices and encouragement.

Finally I would like to thank my parents and my wife. Without their support I could not complete this.

Publications & Awards

Journal Publications (雑誌論文)

1) D. Y. Chen, K. Murakami, K. Dohi, K. Nishida, N. Soneda, Z. C. Li, L. Liu, N. Sekimura, *Depth distribution of Frank loop defects formed in ion-irradiated stainless steel and its dependence on Si addition*, Nuclear Instruments and Methods B, accepted.

2) D. Y. Chen, K. Murakami, K. Dohi, K. Nishida, N. Soneda, Z. C. Li, L. Liu, N. Sekimura, *Radiation defects formed in ion-irradiated 316L stainless steel model alloys with different Si additions,* Materials Transections, Vol.56, No. 9, 2015, in press.

3) D. Y. Chen, K. Murakami, K. Dohi, K. Nishida, N. Soneda, Z. C. Li, L. Liu, N. Sekimura, *Ni-Si precipitate formation in ion irradiated austenite stainless steel and its interaction with dislocation loops*, Journal of Nuclear Materials, to be submitted.

4) D. Y. Chen, K. Murakami, K. Dohi, K. Nishida, N. Soneda, Z. C. Li, L. Liu, N. Sekimura, *Irradiation-induced segregation and Ni-Si precipitate nucleation in stainless steel matrix,* Journal of Nuclear Materials, to be submitted.

5) L. Liu, K. Nishida, K. Dohi, A. Nomoto, N. Soneda, K. Murakami , Z. C. Li, D. Y. Chen, N. Sekimura, *Effects of solute elements on hardening and microstructural evolution in neutron-irradiated and thermally-aged reactor pressure vessel model alloys,* Journal of Nuclear Science and Technology, accepted.

6) Z. Hu, Z. C. Li, D. Y. Chen, W. Miao and Z. J. Zhang, *CO_2 corrosion of IG-110 nuclear graphite studied by gas chromatography*, Journal of Nuclear Science and Technology, Vol. 51, No. 4, pp.487-492, 2014.

Conference Presentations (学会発表)

1) D. Y. Chen, K. Murakami, K. Dohi, K. Nishida, N. Soneda, Z. C. Li, L. Liu, N. Sekimura, *Depth distribution of Frank loop defects formed in ion-irradiated stainless steel and its dependence on Si addition*, Swift Heavy Ions in Matter, 2015, Darmstadt, Germany, Poster presentation.

2) D. Y. Chen, K. Murakami, K. Dohi, K. Nishida, N. Soneda, N. Sekimura, *Gamma prime precipitate formation in 316 stainless steel model alloy irradiated at 450 degrees C*, Annual Meeting of Atomic Energy Society of Japan, 2015, Hitachi, Japan, Oral presentation.

3) D. Y. Chen, K. Murakami, K. Dohi, K. Nishida, N. Soneda, Z. C. Li, L. Liu, N. Sekimura, *Radiation defects formed in ion-irradiated 316L stainless steel model alloys with different Si additions,* Annual Meeting of The Japan Institute of Metals and Materials, 2015, Tokyo, Japan, Oral presentation.

4) D. Y. Chen, K. Murakami, K. Dohi, K. Nishida, N. Soneda, N. Sekimura, *Si effects on hardening of Ni ion irradiated HP316L stainless steel model alloys and its relationship with microstructure*, Annual Meeting of Atomic Energy Society of Japan, 2014, Tokyo, Japan, Oral presentation.

Awards (受賞)

1) 「第 8 回 学生研究発表会 原子力・放射線分野」奨励賞, 日本原子力学会, 2015.